First-principles studies on Pt-doped fcc MoC catalysts for low-temperature water-gas shift reaction

by

DAOFAN CAO

A thesis submitted to the University of Birmingham for the degree of

DOCTOR OF PHILOSOPHY

Birmingham Centre for Energy Storage

School of Chemical Engineering

College of Engineering and Physical Sciences

The University of Birmingham

November 2023

Abstract

The role of hydrogen in future net-zero energy emissions is beyond doubt, both in the transport sector and stationary power generation. As the storage and transportation of hydrogen still present a huge challenge, methanol as a hydrogen carrier and portable hydrogen production have been proposed. However, the hydrogen produced by methanol through the catalytic reaction is inevitably mixed with carbon monoxide as a by-product. To ensure the purity of the hydrogen, the by-product carbon monoxide is usually controlled by the water-gas shift reaction. Thus, the development of water-gas shift catalysts at low temperatures is very important. Recently, the Pt atom doped molybdenum carbide with a face-centred cubic structure (M_1/fcc MoC) has shown great catalytic potential for the low-temperature water-gas shift reaction. However, the Pt-doped fcc MoC catalyst exhibits different crystalline facets that show different physiochemical properties. More importantly, the surfaces can evolve to different surface phase structures under the H_2/H_2O atmosphere due to the thermodynamic stability. Therefore, the reaction mechanism of water-gas shift at different crystal faces and the phase structures of Pt_1/fcc MoC remains controversial.

This work has therefore focused on systematic mechanistic studies on low-temperature water-gas shift reaction of Pt doped fcc MoC catalysts, considering the evolution of surface phase structure and different facets, based on first-principles methods including density functional theory and ab initio thermodynamics while different reaction pathways were evaluated through turnover frequencies (TOFs) calculated by the energetic span

model (ESM) which is more appropriate for the catalytic cycles. The species, including OH*, O*, and H*, were all readily formed on the (001) surface according to the reaction rate constants, but the comprehensive investigation showed that the H_2O*, OH*, and O* species tended to cover the (001) surface instead of H*, justifying the importance of the evolved surface in the water-gas shift reaction. Disregarding the evolution of the surface phase structure, the WGS reaction on the Pt_1/(111)-Mo surface occurred mainly through the redox mechanism, whereas on the Pt_1/(001) surface, it occurred mainly through the associative mechanism. However, considering the evolution of the surface phase structure, the predicted results for the WGS reaction were quite different. The Mo–O monolayer phase enabled redox and H_2O-assisted associative mechanisms to predominate on the Pt_1/(111)-Mo surface, whereas the associative mechanism still predominated on the Pt_1/(001) surface.

From a macro perspective, the original (111)-Mo surface cannot compete with the original or the evolved (001) surfaces in the WGS reaction. However, with the original (111)-Mo surface evolved to the thermodynamically more stable Mo–O monolayer phase, catalytic efficiencies of the redox route and the H_2O-assisted associative route could increase sharply to a level comparable with those of (001) surfaces. Thus, the (111)-Mo and (001) surfaces exhibit similar catalytic efficiencies for the WGS reaction, although through different surface phase structures and pathways.

Acknowledgements

First of all, I would like to express my gratitude to my supervisor, Prof. Yulong Ding, who has given me a lot of advice and guidance on research directions and ideas, all from his profound knowledge and great experience. Thank those who helped me in life at the Birmingham Centre for Energy Storage (BCES), including Dr. Shangfeng Du, Zheng Du, Xusheng Zhang, Zeyu Niu and Yuanye Meng.

I would also express my appreciation to my co-supervisor, Prof. Ke Liu, at the Southern University of Science and Technology (SUSTech). Thank those who helped me at SUSTech, including Prof. Changning Wu, Fenghao Jiang and Decheng Xiang. The funding from Shenzhen Gas & SUSTech Joint Energy Lab and Shenzhen Science and Technology Program (KQTD201804111 43418361) should also be acknowledged.

Thanks to Prof. Xingying Lan, Dr. Xin Su, Dr. Min Wang, and Shouzhuang Li from China University of Petroleum (Beijing) for their effective communication and collaboration.

Last but not least, special thanks to my family. My wife, Tian Yanchu, has selflessly supported me and given so much to my family. In the third year of my PhD study, we had a son, Cao Runquan, and his arrival has made our family happier. The spiritual support I received from my parents and grandparents enabled me to forge ahead during tough times. I am indebted to my family because I spend most of my time at work. Their unwavering support has enabled me to complete my research.

Table of Contents

List of Figures

Figures in Main content

Figures in Supplementary Information

List of Tables

Tables in Main content

Tables in Supplementary Information

Abbreviations

AIT	*ab initio* Thermodynamics
DFT	Density Functional Theory
ESM	Energetic Span Model
ML	Monolayer
SMSI	Strong Metal Support Interaction
TDI	TOF-Determining Intermediate
TDTS	TOF-Determining Transition State
TOF	Turnover Frequency
TST	Transition State Theory
VASP	Vienna *ab initio* Simulation Package
WGS	Water Gas Shift
ZPE	Zero-Point Energy

Nomenclature

$d^{\neq}_{\mathrm{O\cdots H}}$	the O–H bond length
$E^{\mathrm{H_2O}}_{\mathrm{AVG},n}$	average binding energy of water with ZPE correction
δE	Energetic span
$\Delta E^{\neq}$	the energy barrier
ΔE_r	the reaction energy
ΔG_r	Gibbs free energy of the reaction
h	Plank constant
k	reaction rate constant
k_B	Boltzmann constant
q_{vib}	vibrational partition functions
T	reaction temperature
X_{TOF}	the normalised degree of TOF control
γ	stability of surface phase structure

Chapter 1 Introduction

1.1 Background

Energy demand has dramatically increased as a result of the continued economic and urbanisation growth [1] and mainly met by fossil fuels, leading to huge environmental problems, especially global warming, that the world is facing today [2, 3]. In energy transition period, versatile sources and widespread applications make hydrogen a desired, sustainable, and promising energy, also known as the *hydrogen economy* [4-8]. It can be produced not only from fossil fuels, but also from nuclear energy, biomass, wind and solar energy [9-12]. Nowadays, hydrogen has already been used in the chemical processes at around 80 Mt per year as shown in Figure 1.1, while it can also supply electricity or power *via* fuel cells, combustion engines *etc.* with zero or near-zero emissions [13-19].

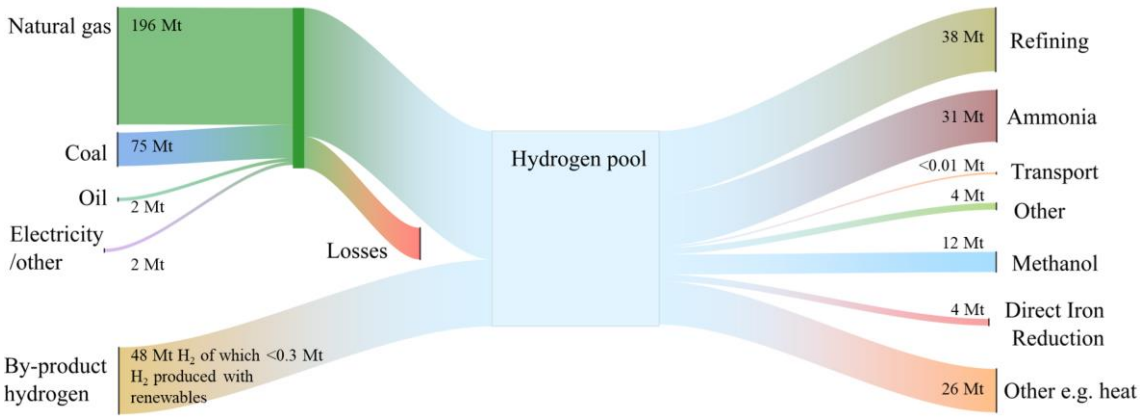

Figure 1.1 Sankey diagram of the hydrogen in 2018 (adopted from [20]).

Hydrogen fuel cell technologies can generate electricity with better efficiency and lower noise than combustion-based technologies [21] in the transport sector [22, 23] or in

stationary power generation applications [24] through an electrochemical mechanism without the restriction from the Carnot cycle. Especially the proton exchange membrane fuel cell (PEMFC) has a solid and flexible electrolyte that is hard to leak or crack and low operating temperature of only ~80°C. As tested by Argonne Lab [22], the performance of commercial PEMFC supplied by Toyota has an average efficiency of 40–50% and a peak efficiency of around 66% [22]. Another frequently mentioned advantage of hydrogen is high gravimetric energy density (GED), typically around 120.2 MJ/kg (lower heating value), which is 2.7 times that of gasoline, while the GED of batteries is only around 250 Wh/kg (*i.e.* 0.9 MJ/kg) [25]. However, the volumetric energy density (VED) is a more important indicator as the limited fuel storage capacity, while hydrogen has a VED of only 10.81 MJ/m^3 at ambient temperature and pressure, compared to 32317 MJ/m^3 for gasoline [26]. Therefore, the storage and transport method for hydrogen must be carefully chosen as greater market acceptance could only be attained by the achieving the same level of convenience as petrol and diesel [27]. Currently, many efficient and reliable hydrogen storage and transport technologies has been developed or are under research [28]. Besides the physical-based methods, which require special physical conditions for storage [29-31], chemical hydrogen carriers [15] store hydrogen in chemical compounds that contain hydrogen at near ambient conditions, including methanol, ammonia, *etc* [32, 33]. Of these, methanol is seen as a potential solution to both the carbon capture/recycling and hydrogen energy supply problems [34-37]. Firstly, methanol can be synthesised from various sources, such as methane, coke oven gas, coal, biomass, and captured CO_2, *etc*

[36, 38-40]. Secondly, it is a colourless, odourless, water-soluble liquid with a boiling point of 64.6 °C, a freezing point of −97.8 °C and a density of 0.80 g/cm^3, by which it means that although it could be lethal if ingested, but these physical properties ensure that it does not evaporate at ambient conditions. There are already 12 Mt of hydrogen in use worldwide for methanol production, signifying the mature supply chain and distribution network [41]. This eliminates the extra costs for additional transport and equipment, significantly reducing the cost of supplying hydrogen [35, 42].

Table 1.1 Comparison of hydrogen storage methods and release conditions.

Storage method	Condition	Hydrogen density (kg H_2/m^3)	H_2 release conditions
H_2 Gas	Ambient	0.3	Direct release
CGH_2	35 MPa	28	Pressure release
	70 MPa	40	Pressure release
LH_2	20.28 K	71	Evaporation
Methanol	Ambient	99	Catalytic T ≥ 200 °C

As can be seen from Table 1.1, methanol has high hydrogen density compared to physical storage methods at same volume. The key step is how to release the hydrogen from the methanol through catalytic reactions, and this generally could be achieved either by direct decomposition or by steam reforming [15]. Direct methanol decomposition produces the syngas consisting of CO and H_2 endothermically as $CH_3OH \rightarrow CO + 2H_2$. Methanol steam reforming (MSR) uses a mixture of methanol and water as feedstock, usually with

a theoretical 1:1 molar ratio of methanol to water, producing carbon dioxide and hydrogen as $CH_3OH + H_2O \rightarrow CO_2 + 3H_2$. However, there is an inevitable by-production of CO in the MSR reaction. Thus, the mechanism of steam reforming is also sometimes explained as a multi-step reaction in which a decomposition reaction takes place followed by a water-gas shift reaction. So additional processes need to be implemented to reduce the CO concentration to obtain high purity hydrogen [43]. Thus, the water-gas shift (WGS) reaction is particularly important in the methanol-to-hydrogen process to control the CO content in the products [44], represented by equation (1-1).

Water-gas shift: $CO + H_2O \rightleftharpoons CO_2 + H_2$ $\Delta H = -41.2$ kJ/mol (1-1)

The WGS is a reversible and exothermic reaction, while lowering the reaction temperature is thermodynamically favourable, but the kinetic limitation would slow down the reaction [45]. The development of catalysts that retain the activity but operate at lower temperature (≤ 200°C) is necessary, which could mitigate this conflict [46]. In recent studies, metal-doped fcc molybdenum carbide (MoC) catalysts have shown excellent low-temperature performance [47, 48]. However, fcc MoC has different crystal facets showing different reaction properties and that surface evolution in a steam reforming atmosphere that containing water and hydrogen, leads to differences in reaction performance, necessitating an insight into the evolution of surface species and their influence on the water-gas shift reaction routes.

1.2 Aims and objectives

This research aims to give an insight into the reaction route of the Pt_1/fcc MoC catalysts on low temperature water-gas shift reaction under H_2O/H_2 atmosphere by a series of first-principles methods, providing guidance for understanding the catalytic performance resulting from differences in surface structures.

The specific objectives of this thesis are:

(1) To understand the evolution of surface phase structure of (001) surface of fcc MoC considering the formation and configuration of various species under H_2O/H_2 atmosphere.

(2) To study the catalytic efficiency of the water-gas shift reaction on the original (111)-Mo and original (001) surfaces considering various reaction routes, using the density functional theory and the energy span model.

(3) To further investigate the catalytic efficiency of WGS on the evolved surfaces and discuss the influence of the surface phase on it.

1.3 The layout of the Thesis

This thesis comprises seven chapters:

Chapter 2 summarises the research progress and outlines the main challenges and controversies relevant to this thesis.

Chapter 3 then introduces the theories and methodologies used in this thesis including

density functional theory, *ab initio* molecular dynamics, *ab initio* thermodynamics, and energetic span model as well as the computational details used in this thesis.

Chapter 4 presents the results and discussion of the surface phase structure evolution on the (001) surface of fcc MoC.

Chapter 5 gives the results and discussion of the water-gas shift reaction on the original surface of the Pt_1/fcc MoC under H_2/H_2O atmosphere considering the crystal facets and different reaction routes.

Chapter 6 provides the results and discussion of the water-gas shift routes on the evolved surface of the Pt_1/fcc MoC under H_2/H_2O atmosphere considering the crystal facets, different reaction routes, and the surface phase structure evolution.

Chapter 7 summarises the main conclusions and provides recommendations for the future work.

Chapter 2 Literature Review

2.1 Mechanism of water-gas shift reaction

The water-gas shift reaction was first discovered in 1780 by the Italian scientist Felice Fontana while quenching red-hot coal with water in a glass bell jar, and the composition of water gas was subsequently determined by Lavoisier [49, 50]. The produced water-gas is a mixture of hydrogen and carbon monoxide, which is currently known as syngas in the chemical industries. The overall chemical equation of WGS reaction is depicted as equation (1-1). In industrial scale WGS, the WGS reaction is achieved by means of two-stage units with different temperatures, where the high-temperature shift (HTS) operates from 320 to 450°C and the low-temperature shift (LTS) from 150 to 250°C. But what we are currently talking about is the control of CO content in a portable methanol-to-hydrogen device. The steam reforming of methanol occurs at temperatures in the range of 200 to 300°C. For overall system efficiency considerations, the operating temperature of the low-temperature water-gas shift reaction can be better coupled with the outlet temperature of the steam reforming [48, 51, 52].

However, until now, there is still no clear answer to the mechanism of the water-gas shift reaction [45, 53]. Especially for the LTS, the reaction mechanism is more complicated while the different types of catalysts give rise to different microscopic mechanisms [53]. Two primary mechanisms have been proposed and are widely accepted in low-temperature water-gas shift reactions, namely the redox (or regenerative) mechanism and the associative mechanism [45]. These two mechanisms are described next.

The reactants of water gas shift reaction are CO and H_2O, so the earliest steps are adsorption of the reactants as follows:

$$CO + * \longrightarrow CO^* \tag{2-1a}$$

$$H_2O + * \longrightarrow H_2O^* \tag{2-1b}$$

$$H_2O^* + * \longrightarrow H^* + OH^* \tag{2-1c}$$

Here and later in the text, the asterisk ($*$) indicates a vacant surface site on the catalytic surface while the species with the asterisk (X^*) means an adsorbed species.

In the redox (or regenerative) mechanism, the catalyst undergoes oxidation and reduction cycles during the reaction [54]. The adsorbed H_2O (2-1b) or adsorbed OH* (2-1c) can dissociate into O* species. Then, the adsorbed CO* can be oxidised by the surface adsorbed O* to form surface adsorbed CO_2*. This mechanism involves following steps:

$$OH^* + * \longrightarrow O^* + H^* \tag{2-2a}$$

$$OH^* + OH^* \longrightarrow H_2O^* + O^* \tag{2-2b}$$

$$CO^* + O^* \longrightarrow CO_2^* + * \tag{2-2c}$$

Finally, the adsorbed CO_2* and H* species would form the products CO_2 and H_2.

$$CO_2^* \longrightarrow CO_2 + * \tag{2-3a}$$

$$H^* + H^* \longrightarrow H_2 + 2^* \tag{2-3b}$$

The original description of the redox mechanism came from Armstrong and Hilditch in 1920, based on the oxidation and reduction of iron [55]. It was not until 1949 that Kulkova

and Temkin provided a clearer expression taking into account kinetic data [56]. At low water contents in the feed, the dissociation of water (2-1b) is the rate limiting step. In contrast, at high the water contents, the CO oxidation (2-2c) is the rate limiting step.

In the associative mechanism, the CO interacts with surface OH* generated by dissociative adsorption of water, leading to the formation of the intermediate, such as carboxyl (COOH*) or formate (HCOO**). Taking the carboxyl as an example, this mechanism involves following steps after (2-1a) to (2-1c) and before (2-3a) and (2-3b):

$$CO^* + OH^* \longrightarrow COOH^* + * \quad \text{(2-4a)}$$

$$COOH^* + * \longrightarrow CO_2^* + H^* \quad \text{(2-4b)}$$

If there is the formate intermediate in the associative mechanism, the similar chemical equation can be obtained by replacing COOH* in equation (2-4a) and (2-4b) with HCOO**. In 1920, Armstrong and Hilditch firstly proposed the associative mechanism based on the copper catalyst [55]. They summarised that formic acid tends to decompose into CO_2 and H_2, and thus formate was considered to be the intermediate. Many studies prior to 2007 presented formate as the intermediate and some researchers also pointed out the unimportance of the carboxyl intermediate in the low temperature water-gas shift reaction [57, 58]. In 2008, Grabow *et al.* [59] and Gokhale *et al.* [60] investigated the mechanism of the low temperature water gas shift reaction on platinum and copper respectively through density functional theory (DFT) calculations. They proposed that the carboxyl species is the important intermediate during the WGS reaction, while also

concluded that the formate acts as a spectator species [61]. Fu et al. [62] also prudently excluded the formate as the intermediate by experiment. Nelson *et al.* [63] addressed this controversy combining comprehensive experimental and computational studies and determined that the carboxyl is the primary intermediate during the (r)WGS. Later, they confirmed that on the oxide-supported atomically dispersed transition metal catalysts, the formate intermediate can be eliminated [64, 65]. Metal carbide supported noble metal catalysts have recently been reported as highly active for the WGS reaction at low temperatures [47, 48, 66-70]. It was reported that COOH species is the intermediate in the low-temperature WGS reaction over the MoC [48, 71]. Therefore, in the catalytic system based on molybdenum carbide for WGS, only the reaction pathway related to the COOH intermediate could be considered.

2.2 Molybdenum carbide based catalysts

In recent years, molybdenum carbides have been receiving significant attention in the field of hydrogen production [67, 72-77] due to its unique chemical and surface properties, which can be used for methanol steam reforming [78, 79], methanol decomposition [80] and water-gas shift reaction (WGS) [81]. Lin *et al.* [48] reported that the Pt_1/α-MoC catalysts exhibited high catalytic activity, a result that is more than 5 times higher than the commercial $Cu/ZnO/Al_2O_3$ and Cu-Al spinel catalysts [82-84] and even 18 times higher than the $Pt/NiAl_2O_4$ catalyst [85]. These fully demonstrated the great potential of MoC-based catalysts in these types of reactions.

In molybdenum carbide, carbon atoms occupy interstitial sites in the molybdenum metal, resulting in longer metal-metal bonds and the presence of three types of bonding: metallic, covalent and ionic [86]. As a result, it is able to exhibit catalytic properties similar to those of platinum group metals (Pt, Pd, Ru, *etc.*) [87, 88]. Various types of molybdenum carbides (δ-MoC, α-MoC, β-Mo_2C, γ-MoC and η-MoC are synthesised and explored [89-92]. However, there are differences in the naming conventions used by research groups or research areas, which may be confusing when reviewing relevant references. To avoid any confusion, molybdenum carbides can be classified based on crystal structures, namely into lattices with face-centred cubic (fcc), hexagonal closed packed (hcp), and simple hexagonal (hex) structures [93]. The δ-MoC or α-MoC has a face-centred cubic structure (*i.e.* NaCl type) with hexoctahedral crystal structures [94, 95]. Generally speaking, the term of α-MoC is commonly found in experimental studies and the term of δ-MoC is commonly found in computational studies [96]. The β-Mo_2C has a hexagonal closed packed structure and the γ-MoC has a simple hexagonal structure (*i.e.* WC type). In this thesis, the term fcc MoC is used, but when citing reported references, the notation retains the original form of the references to make it easier to trace the source.

Among different types of MoCs, the fcc MoC surfaces loaded with certain dispersed metals show exceptional catalytic properties in low temperature hydrogen production reactions. The extremely strong metal support interaction (SMSI) effect, together with excellent O–H activation ability [75] and H_2O dissociation capabilities [97], allows the fcc MoC to outperform other MoCs, especially in the low temperature water gas shift or

steam reforming for hydrogen production reactions. The experimental results by Dong and Bao *et al.* [97] clearly demonstrated the SMSI effect between highly dispersed Au over-layers and the fcc MoC, where the strong charge transfer through the Au-carbide interfaces endows the Au/MoC_x with excellent low-temperature WGS reactivity. As a milestone, Lin and Ma *et al.* [48] reported that the Pt_1/α-MoC presented extraordinary reactivity of methanol aqueous phase reforming in the low temperature. The authors found that generation and molar proportional increase of β-Mo_2C phase in the fcc MoC would seriously suppress the reactivity of Pt_1/α-MoC. Using the cheap and abundant Ni instead of the noble Pt, another work by Lin and Ma *et al.* [68] indicated that the Ni_1/fcc MoC performed better than Pt/Al_2O_3 and Cu/ZnO/Al_2O_3 catalysts. However, the reaction temperature required by Ni_1/fcc MoC was higher than that of Pt_1/fcc MoC (513 *vs.* 463 K), meanwhile the atomic turnover frequency of Ni_1/fcc MoC is much lower (1805 *vs.* 4134 h^{-1}). As other breakthroughs in low-temperature hydrogen production, Au/fcc MoC [66] and (Pt_1-Pt_n)/fcc MoC [47] prepared by Ma *et al.* exhibited excellent WGS reactivity at ultra-low temperatures (< 423K) surpassing those of Pt/β-Mo_2C, Au/β-Mo_2C and noble metals catalysts supported on oxides. The experiments by Rodriguez and Illas *et al.* [98] also confirmed the superiority of the Au/fcc MoC catalyst over the Au/β-Mo_2C catalyst in the WGS reaction. Besides, Wang and Sun *et al.* [70] demonstrated that Ir_1/α-MoC (fcc MoC) has high activity in the water-gas shift reaction at 423 K, and the reaction rate was one to two order magnitudes higher than those on Ir_1/FeO_x and Ir_1/Al_2O_3. These studies have illustrated the excellent catalytic performance of fcc MoC for the low-temperature

water-gas shift reaction, especially with the loading of highly dispersed Pt particles. The excellent activity of fcc MoC towards water would also complicate the active species on the catalytic surface during the reaction, leading to different mechanistic interpretations.

2.3 Surface phase structure of fcc MoC

As metal-doped fcc MoC catalysts have shown unprecedented reactivity in the low-temperature WGS reaction, thus it is of great significance to explore and clarify the origin of its high performance. Besides, the WGS reaction is also considered as part of reaction route in the steam or aqueous phase reforming of methanol, where the dehydrogenation of methanol first forms CO and H_2, then the CO reacts with H_2O resulting in CO_2 and further H_2 release (WGS) [99-101]. In these reactions, fcc MoC plays an important role in the activation of water to surface OH* or further surface O* [48], giving the oxidation capability to the surface phase of fcc MoC which is then reduced by CO or other reactants in the reduced state. For water-gas shift reactions, water activation would affect the entire reaction. The activity of the catalyst surface is maintained by the constant oxidation-reduction cycle of oxygen-containing species on the fcc MoC surface. However, once this surface cycle is broken, the surface accumulates excess O* species. Consequently, the SMSI effect and the ability to dissociate water are affected, indicating catalyst deactivation [47, 66, 97]. The interaction between the O* species and the fcc MoC surface should be neither too strong nor too weak, which is what is known as the Sabatier principle [102-105]. Analysing the species on the catalyst surface is particularly important for developing catalysts and elucidating the reaction mechanism, as different surface

structures produce different catalytic behaviour due to different physicochemical properties. For example, Mo- and C-terminated surfaces of Mo_2C (001) displayed significantly distinct catalytic performances with respect to the accumulation of surface O* species [106].

The results of characterisation techniques including the high-resolution transmission electron microscopy (HRTEM) showed that the prepared fcc MoC mainly exposed two crystalline planes, (111) and (001) facets [91]. There is still some controversy about the catalytic role played by these two facets. Ma and co-workers, through a series of experimental and computational works, claimed the importance of the Mo-terminated fcc MoC (111) surface for the water gas shift reaction [66] and the methanol aqueous phase reforming reaction [48, 68]. In comparison, Sun and Lin *et al.* [70] claimed that the fcc MoC (001) surface is predominantly exposed in the water-gas shift reaction, which was also supported by the computational results of DFT carried out by Politi and Illas *et al.,* showing high stability of the fcc MoC (001) surface [107]. Later, Posada-Pérez and Illas *et al.* [98] demonstrated the highly active low-temperature reactivity of the Au/fcc MoC (001) surface by combining the experiments with DFT calculations.

As can be seen from the above summary, the controversy over the two facets (111) and (001) arises mainly from the physicochemical properties of the different crystalline planes. Different facets have different reactivity, which leads to variation in the composition of the surface phases during chemical reactions. Furthermore, the structure of the surface phase species becomes more complex due to the thermodynamic and kinetic differences

of the various species (H_2O*, OH*, O* and H*) on different facets of fcc MoC under the reaction atmosphere. Recently, Chu and Liu *et al.* used a series of first-principles methods including DFT calculations, *ab initio* thermodynamics, and *ab initio* molecular dynamics, to study the evolution of the surface phase structure of the Mo-terminated fcc MoC (111) surface under a steam reforming atmosphere (H_2O/H_2 mixture) [108]. They found that the surface OH* phase was easier to form than the surface O* phase at the early stage of the reaction, resulting in the highly active reactivity of the Mo-terminated fcc MoC (111) surface. However, the catalytic surface was predicted to deactivate quickly after several cycles of the reaction because the surface O* has a higher thermodynamic stability, leading to the accumulation of the inert O* phase [108]. The evolution of surface phase structure over time is closely influence the behaviours of MoC type catalysts. Cai *et al.* [79] found that in the steam reforming on Zn-Pt/MoC catalysts, the methanol conversion and the H_2 production rate gradually decreased with the increase in the running time of the experiments, especially at high steam concentration. They concluded that this was due to the high steam concentration which accelerated the oxidation of the (001) surface in the catalyst.

Therefore, revealing and understanding the structure and evolution of the surface phase on different facets ((111) vs (001)) of fcc MoC under steam reforming atmosphere (H_2O/H_2) is essential before studying the mechanism and reaction pathway of the water gas shift reaction. There is already a framework for research on the Mo-(111) surface of fcc MoC, and there is still work to be done on the (001) surface of MoC.

2.4 Low temperature water gas shift reaction *via* fcc MoC

As mentioned above, the WGS reaction using various supported metal catalysts usually proceeds *via* two routes, namely, the redox route and the associative route [71]. In the redox mechanism, the carbon monoxide is directly oxidised by surface O* atom generated by the successive dehydrogenation of H_2O on the substrate [109, 110]. In the associative mechanism, the CO first combines with one OH group of H_2O to form a surface carboxyl HO–CO* intermediate, and then further dehydrogenation leads to CO_2 [59, 60, 111]. This means that on the catalyst surface, the adsorption and reaction of reactants at the active sites will take place in a different order. The different routes arise mainly from the adsorption energy, thermodynamics and kinetic states of the species on the surface.

Due to the existence of (111) and (001) facets of fcc MoC, there is controversy not only about which surface plays the dominant role in the WGS reaction but also about which kind of mechanism is preferred by different surfaces. By DFT calculations, Posada-Pérez, Rodriguez and Illas *et al.* [98] explored the WGS reaction routes on a (001) surface model of fcc MoC with or without a supported Au_4 cluster. Based on the energy barriers of certain elementary reaction steps, they argued that the Au_4/fcc MoC (001) surface preferred the redox route to the associative route, while it was just the opposite on the un-doped fcc MoC (001) surface. The recent research conducted by Prats and Illas *et al.* [112] exhibited the WGS reaction mechanisms on the Au_4/fcc MoC (001) surface using the kinetic Monte Carlo method, which could take the effects of reaction kinetics into account. Contrary to the conclusions based only on the energy barriers of elementary reaction steps,

their results showed that the associative route was the predominant mechanism on the Au_4/fcc MoC (001) surface responsible for 99.8% CO_2 molecule formation. More recently, Li, Lin and Wang *et al.* performed DFT calculations on the WGS reaction catalysed by a series of single-atom catalysts where Rh_1, Pd_1, Pt_1 and Au_1 are supported on fcc MoC (001) surface [113]. With the associative mechanism considered only in their study, they found that the Rh_1, Pd_1, and Pt_1 sites served as single-atom promoters to enhance the reactivity of the (001) surface of fcc MoC rather than participating directly in the reaction, while the Au_1 not only acted as a promoter but could also directly participate in the reaction as a site for CO adsorption. In contrast, other research groups claimed that the (111)-Mo terminated surfaces of fcc MoC were the predominant surfaces in catalysing the relevant reactions. Ma and co-workers proposed a double-hydroxyl associative mechanism for the WGS reaction on a Au_{15}/fcc MoC (111) surface model by DFT calculations, where the formation of HO–CO* intermediate from CO reacting with the first OH* and its subsequent dehydrogenation to CO_2 assisted by the other OH* proceeded in one elementary reaction step [66]. Similarly, the double-hydroxyl associative mechanism was also considered in the WGS reaction constituting the route for methanol reforming with a Pt_1/fcc MoC (111) surface model [48].

Besides the studies on the effects of different crystal facets of fcc MoC on the WGS reaction, the surface phase structural reconstructions, particularly with chemical changes arising from interactions between the 'fresh' surface and the reactants or products, are more closely related to the intrinsic reactivity of heterogeneous catalysts [114-117].

Recently, Chu *et al.* systematically investigated the surface phase structural evolutions of the MoC (111)-Mo surface under the H_2O/H_2 environment using combined ab initio-based methods [108]. It was found that due to the fast O–H cleavage kinetics of H_2O, the (111)-Mo surface is readily covered by a layer of OH groups, and with the passage of time, it is prone to be covered by a layer of O* atoms instead of OH* due to the thermodynamic stability of the Mo–O layer. As a contrast, the case of the MoC (001) surface is discussed in this thesis. More recently, employing the oxidised surface model constructed by covering a layer of O* atoms on the 'fresh' surface, Tian, Tong and Xu *et al.* [118] proposed a water-assisted associative mechanism of WGS on the Au/fcc $MoC_x(111)O_y(OH)_z$, where the CO adsorbed on Au directly abstracted OH from the physically adsorbed H_2O molecule to form the HO–CO* intermediate, meanwhile the leftover H of H_2O bonded with the O* atom of the oxidised substrate. They argued that by avoiding the difficulty of OH* or O* detachment from the substrate during HO–CO* formation, the CO conversion rate on the Mo–O layer phase could be significantly accelerated. For the recently reported Pt/γ-Mo_2N of excellent reactivity and stability in WGS reaction, Jia and co-workers [119] proved that the actual active phase of γ-Mo_2N was the highly distorted MoO_x surface layers constrained by the γ-Mo_2N lattice, the O vacancies of which could dissociate H_2O to OH* and be regenerated by the reaction of CO with OH*.

2.5 Summary of the literature review

Based on the literature review and previous studies, we conclude that the catalytic

performance of metal doped fcc MoC is affected by the exposed crystal surfaces and closely related to the surface phase structure under the working environment. More specifically, the factors include different crystal facets ((111) *vs.* (001)), different surface phase structures (original or 'fresh' surface *vs.* $MoC(H_2O)_x(OH)_y(O)_z$ surface), and different reaction routes (redox route, associative route or water-assisted associative route) in the water-gas shift reaction.

As far as we know, previous DFT studies on the above factors are relatively scattered and far from comprehensive and lacked effective evaluation methods for the kinetics of different reaction routes. One desired concept for the kinetic evaluation is the turnover frequency (TOF) [120] of catalytic cycles on a specific active site, which can be obtained from the DFT-computed potential energy profile using the energetic span model [121]. This model makes use of the fact that the highest transition state or a single elementary reaction step only could not always determine the efficiency of a catalytic cycle [122, 123]. Instead, the energy span model identifies two states possessing the largest degree of control on the TOF, known as TOF-determining transition state and TOF-determining intermediate. The theories and methods are presented in detail in the next chapter.

In conclusion, as the excellent performance of Pt-doped fcc MoC as a catalyst in the low-temperature water-gas shift reaction for hydrogen production has been recently reported, the existence of different facets in fcc MoC, *i.e.* the (001) and (111) surfaces, requires further investigation into the reaction mechanism, especially considering the influence of surface phase evolution, under the real reaction environment. The evolution of the phase

structure on the MoC (111)-Mo surface has been reported, so a similar idea can be used to study the MoC (001) surface. Based on this, the water-gas shift reaction of Pt_1/fcc MoC can be systematically studied by combined *ab initio* methods. For comprehensive and systematic studies of Pt doped fcc MoC catalysts on low-temperature water-gas shift reaction under steam reforming atmosphere, it is necessary to examine the possible reaction routes of the water-gas shift reaction on the Pt_1/fcc MoC (111) and (001) surfaces, where the various surface phase structures existing under the typical H_2O/H_2 environment were considered, after investigating the phase structure of the MoC (001) surface. Then, the energetic span model was employed to evaluate and compare the TOF of different catalytic cycles on the various surface phase structures of fcc MoC (111) and (001) facets. Finally, a comprehensive discussion on the structure-performance relationship of the Pt_1/fcc MoC model system was presented.

Chapter 3 Theories and methodologies

Aiming to investigate the water dissociation on fcc MoC as well as the water-gas shift reaction occurring on Pt_1/fcc MoC at lower temperatures under a hydrogen-rich atmosphere, this thesis will provide detailed calculations of the system through first-principles methods and confirm them with experimental results from the literature.

First-principles methods, also known as *ab initio* methods ("*ab initio*" is Latin for "from the beginning"), are a class of computational and quantum chemistry techniques based on quantum mechanics that do not rely on any empirical data or parameters, but instead, they derive properties and behaviours directly from the fundamental laws of physics [124], providing a powerful and nuanced approach to understanding chemical phenomena at the molecular and atomic levels [125]. By employing quantum chemistry, researchers can delve into the intricate details of the reaction mechanism on heterogeneous catalyst surfaces, identifying reaction pathways, transition states and energy barriers, unveiling a comprehensive view of how reactants interact with the catalyst, how bonds are formed and broken, and how reaction kinetics are governed, while also facilitating catalyst optimisation by predicting how structural or electronic changes affect catalytic activity and selectivity [126]. In the context of the WGS reaction, these methods not only enhance the fundamental understanding of the reaction, but also guide the development of more efficient and sustainable catalytic processes [60]. Its ability to bridge theoretical calculations with tangible applications underscores the indispensable role of first-principles methods in modern chemical research and technology.

This chapter focuses on an introduction to the theories and methodologies used in this thesis including density-functional theory (DFT), *ab initio* molecular dynamics (AIMD), *ab initio* thermodynamics (AIT) and the energy-spanning model (ESM). DFT is used to construct the potential energy surfaces of the reaction paths, AIMD is used to perform the evolution of specific surface structures in the kinetic aspect, AIT calculates the stability and builds the surface thermodynamic phase diagrams based on DFT results, and ESM is used to perform the turnover frequency (TOF) by using the DFT results as well. The specific setup, validation and testing of these methods will be described in the next chapter.

3.1 Fundament for quantum chemistry

3.1.1 Time independent Schrödinger equation

In the realm of classical physics, the deterministic behaviour of systems is well-described by Newtonian mechanics. However, as we delve into the microscopic world of atoms and subatomic particles, classical descriptions falter, unable to capture the inherent probabilistic nature of quantum systems. Herein lies the significance of the Schrödinger equation, introduced by Erwin Schrödinger and published in 1926 [127]. Schrödinger equation serves as the cornerstone of quantum mechanics, providing a mathematical framework to describe the evolution of quantum states over time. Unlike classical equations of motion, which yield definitive trajectories, the Schrödinger equation yields wave functions, encapsulating all possible outcomes and their associated probabilities [128]. We can get the wave function for a single nonrelativistic particle by solving the Schrödinger equation as follows:

$$i\hbar \frac{\partial}{\partial t} \Psi(\boldsymbol{r},t) = \hat{H}\Psi(\boldsymbol{r},t) \tag{3-1}$$

Here, i is the imaginary unit ($i = \sqrt{-1}$), $\hbar$ is the reduced Planck constant ($\hbar = h/2\pi$, while h is original Planck constant), $\Psi(\boldsymbol{r},t)$ is the wave function where $\boldsymbol{r}$ is the position vector in three-dimensional space and t is time. $\hat{H}$ is the Hamiltonian operator corresponding to the total energy of a system in quantum mechanics. One word more, such a symbol with a hat represents an operator, which is particularly important in quantum mechanics, and an operator acts on a function or a value to produce another function or value. But it should be noted that the notion $\hat{H}\Psi$ means the Hamiltonian operation is to be performed on Ψ, instead of $\hat{H}$ times Ψ.

Hamiltonian operator can be expressed as the sum of the kinetic and potential energies as

$$\hat{H} = \underbrace{-\frac{\hbar^2}{2m}\nabla^2}_{\substack{\text{kinetic energy} \\ \text{operator}}} + \underbrace{V(\boldsymbol{r},t)}_{\substack{\text{potential energy} \\ \text{operator}}} = \hat{T} + \hat{V} \tag{3-2}$$

in which m is the mass of the particle, ∇^2 is the Laplacian operator that can be written as $\nabla^2 = \partial^2/\partial x^2 + \partial^2/\partial y^2 + \partial^2/\partial z^2$ in three dimensions using Cartesian coordinates. Thus, the Schrödinger equation can be rewritten from (3-1) to following time-dependent Schrödinger equation (TDSE) form as

$$i\hbar \frac{\partial}{\partial t} \Psi(\boldsymbol{r},t) = \left[-\frac{\hbar^2}{2m}\nabla^2 + V(\boldsymbol{r},t) \right] \Psi(\boldsymbol{r},t) \tag{3-3}$$

describing a system evolving with time. Once having determined wave function, the

probability density function can be defined as $\Pr(\boldsymbol{r},t)=|\Psi(\boldsymbol{r},t)|^2$. If the potential energy is assumed that does not evolve with time, the V is uniquely a function of location $\boldsymbol{r}$ as $V(\boldsymbol{r})$. For stationary state, the wave function $\Psi(\boldsymbol{r},t)$ can be separated as the product of $\Psi(\boldsymbol{r})$ and $\varphi(t)=e^{-iEt/\hbar}$, thus the probability density is

$$|\Psi(\boldsymbol{r},t)|^2=\Psi^*(\boldsymbol{r})\Psi(\boldsymbol{r})e^{iE/t\hbar}e^{-iE/t\hbar}=|\Psi(\boldsymbol{r})|^2 \tag{3-4}$$

which is time independent. In classical physics, this phenomenon is referred to as a standing wave. Here, according to above stationary state assumption, we can obtain the time independent Schrödinger equation (TISE) as

$$\hat{H}\Psi(\boldsymbol{r})=\left[-\frac{\hbar^2}{2m}\nabla^2+V(\boldsymbol{r})\right]\Psi(\boldsymbol{r})=E\Psi(\boldsymbol{r}) \tag{3-5}$$

where E is the total energy of the system. In this form, the wave function is an eigenfunction of the Hamiltonian operator with corresponding eigenvalues E. There are some basic features of the wave function at stationary states: (1) time independent physical properties, (2) time independent probability densities and expectation values, (3) statistically certain value of total energy, and (4) the general solution of this separable Schrödinger equation is a linear combination of the stationary states.

3.1.2 Many-body Schrödinger equation

For many-body system, it becomes much more complicated. Considering a system containing M nuclei and N electrons while $\boldsymbol{R}_M$ and $\boldsymbol{r}_N$ are the coordinates of nuclei and electrons respectively. Then the Hamiltonian operator (3-2) can be expanded

as a many-body form:

$$\begin{aligned}\hat{H} &= \hat{T} + \hat{V} \\ &= \underbrace{\underbrace{-\frac{\hbar^2}{2}\sum_{i=1}^{M}\frac{1}{M_i}\nabla_i^2}_{\text{Nuclei kinetic energy}} \underbrace{-\frac{\hbar^2}{2m_e}\sum_{i=1}^{N}\nabla_i^2}_{\text{Electron kinetic energy}}}_{\hat{T} \Rightarrow \text{kinetic energy terms}} + \\ &\underbrace{\underbrace{\frac{1}{2}\sum_{\substack{i=1 \\ i\neq j}}^{M}\sum_{j=1}^{M}\frac{Z_i Z_j e^2}{|\boldsymbol{R_i}-\boldsymbol{R_j}|}}_{\text{Nuclear}-\text{Nuclear repulsion}} \underbrace{-\sum_{i=1}^{M}\sum_{j=1}^{N}\frac{Z_i e^2}{|\boldsymbol{R_i}-\boldsymbol{r_j}|}}_{\text{Nuclear}-\text{electron attraction}} + \underbrace{\frac{1}{2}\sum_{\substack{i=1 \\ i\neq j}}^{N}\sum_{j=1}^{N}\frac{e^2}{|\boldsymbol{r_i}-\boldsymbol{r_j}|}}_{\text{Electron}-\text{electron repulsion}}}_{\hat{V} \Rightarrow \text{potential energy terms}}\end{aligned} \tag{3-6}$$

where M_i is the mass of nuclei, m_e is the electron mass.

One can imagine the interaction of nuclei and electrons in the system, the motions of the elections and nuclei are coupled. The mass of a nucleus is much greater than the mass of an electron (more than 1000 times), and consequently nuclei move much more slowly than do the electrons. Thus, for electrons, the nuclei are fixed, and further, the coordinates of the nuclei in the system can be approximated as fixed. The lowest energy state of electrons, *i.e.* ground state, can be found for a given set of electrons moving in the field of a set of nuclei. This is called the Born-Oppenheimer approximation, which was proposed by Max Born and J. Robert Oppenheimer [129]. The contribution of nuclei to the kinetic energy can be neglected and we can treat the ion-ion interaction classically. The Schrödinger equation can be separated into one electronic equation and one nuclear equation [130]. Once the position of nuclei is specified ($\boldsymbol{R}$), the ground energy state of these can be determined as $E(\boldsymbol{R})$. This function gives the adiabatic potential energy surface of atoms. The lowest energy can specify the lowest energy configuration of the

atom, and the highest energy point along the minimum energy path is a saddle point, which is sometimes identified as the transition state. The terms related to the nuclear position can be regarded as parameters, the term for nuclei kinetic energy can be deleted, and the Schrödinger equation is

$$\begin{aligned}\hat{H}\Psi &= \left[\hat{T}+\hat{V}+\hat{U}\right]\Psi = E\Psi \\ &= \left[-\frac{\hbar^2}{2m_e}\sum_{i=1}^{N}\nabla_i^2 + \sum_{i}^{N}V(\boldsymbol{r_i}) + \sum_{i=1}^{N}\sum_{j<i}U(\boldsymbol{r_i},\boldsymbol{r_j})\right]\Psi\end{aligned} \tag{3-7}$$

Despite above simplifications, obtaining an exact solution of the Schrödinger equation for electrons is still an impossible task. To find accurate approximations, several techniques have been developed. Wavefunction-based methods and density-based methods are the two main categories of methods. Wavefunction-based methods, such as the Hatree-Fock method, are useful and accurate enough for small molecules, but for the larger system, such as heterogeneous catalysts, they have a high computational cost. Solving the many-body Schrödinger equation required significant computational resources, limiting the size and complexity of systems that could be studied. Different methods were often tailored to specific types of systems or properties, lacking a universal approach that could be broadly applied. With respect to the computational cost and accuracy, density functional theory gives a well compromising solution.

3.2 Density functional theory

3.2.1 Hohenberg-Kohn theorems

Shortly after the introduction of the Schrödinger equation, the Thomas-Fermi (TF) model,

named after Llewellyn Thomas [131] and Enrico Fermi [132], was developed for the electronic structure of many-body systems. Unlike wave function theory, the Thomas-Fermi model is formulated in terms of the electronic density alone by simplifying the many-body problem to a homogeneous electron gas, making it a precursor to modern density functional theory, suggesting that within an atom, electrons are distributed uniformly in small volume elements, though the overall electron density can vary.

The probability density $n(\boldsymbol{r})$ that any of the N electrons is at the position $\boldsymbol{r}$ is called the particle density and is therefore given by

$$n(\boldsymbol{r}) = N \int \Psi^*(r, r_2, \ldots, r_N)\Psi(r, r_2, \ldots, r_N)\ \mathrm{d}^3 r_2 \mathrm{d}^3 r_3 \ldots \mathrm{d}^3 r_N \tag{3-8}$$

Obviously, the integration of the above is the number of particles:

$$\int n(\boldsymbol{r})\mathrm{d}^3\boldsymbol{r} = N \tag{3-9}$$

In the Thomas-Fermi model, the total energy can be expressed by:

$$E_{TF}[n(r)] = C_F \int n^{5/3}(\boldsymbol{r})\mathrm{d}\boldsymbol{r} - Z\int \frac{n(\boldsymbol{r})}{\boldsymbol{r}}\mathrm{d}\boldsymbol{r} + \frac{1}{2}\iint \frac{n(\boldsymbol{r})n(\boldsymbol{r}')}{|\boldsymbol{r}-\boldsymbol{r}'|}\mathrm{d}\boldsymbol{r}\,\mathrm{d}\boldsymbol{r}' \tag{3-10}$$

where C_F is a factor equal to 2.871, Z is the charge of nucleus, and the terms represent the kinetic energy of electrons, electrons-nuclei interaction, and electron-electron interaction, respectively. Although such a model lacks in electron exchange and correlation energies, and subsequent complementary models still suffer from large errors, the importance of this model lies in that the electron density is used as a variable, which

established the foundation for the emergence of DFT.

In 1964, Hohenberg and Kohn put forward and proven two simple and ingenious Hohenberg-Kohn (HK) theorems which are seen as the theoretical foundation and a milestone of density functional theory [133].

The first Hohenberg-Kohn theorem is the proof of existence that indicates the ground state properties of a system are uniquely determined by its electron density. In other words, the external potential $V(\boldsymbol{r})$ is uniquely determined by the ground state electron density $n(\boldsymbol{r})$. From basic quantum mechanics, the calculation pathway is $V(\boldsymbol{r}) \rightarrow \hat{H} \rightarrow \psi_0 \rightarrow n$, while according to the first HK theorem, it can be further concluded that $n \rightarrow V(\boldsymbol{r}) \rightarrow \hat{H} \rightarrow \psi_0, \psi_1, \ldots, \psi_N$. The second Hohenberg-Kohn theorem emphases variational theorem that the energy of the true electron density is always less than the energy of any other density. Once we use the density define a universal functional for the energy $E[n]$, the exact ground state is the global minimum value of this functional. Thus, the total energy can be expressed using electron density as

$$E[n(\boldsymbol{r})] = \int n(\boldsymbol{r}) V_{\text{ext}} \mathrm{d}\boldsymbol{r} + F_{\text{HK}}[n(\boldsymbol{r})] \tag{3-11}$$

where $V_{\text{ext}}(n(r_i))$ is an external potential indicating the Coulomb interaction between electron and the i nucleus. The $F_{\text{HK}}[n(\boldsymbol{r})]$ is the Hohenberg-Kohn functional and usually formulated as

$$F_{\text{HK}}[n(\boldsymbol{r})] = T_{\text{e}}[n(\boldsymbol{r})] + E_{\text{ee}}[n(\boldsymbol{r})] \tag{3-12}$$

where $T_e[n(\boldsymbol{r})]$ is the kinetic energy of electrons and $E_{ee}[n(\boldsymbol{r})]$ is the electron-electron interaction. In above expression, the external potential energy due to the nuclei-electron attraction is system dependent, and the HK functional is universally valid.

However, Hohenberg-Kohn theorems do not give a way to calculate the ground state energy using the electron density, since the expression for $F_{HK}[n(\boldsymbol{r})]$ is unknown, nor do they tell us how to obtain the electron density in the absence of a wave function.

3.2.2 Kohn–Sham equations

In 1965, Walter Kohn, along with Lu Jeu Sham, formulated the Kohn-Sham equations, mapping the real system of interacting electrons onto a system of non-interacting particles with the same electron density [134].

For equation (3-12), the electron-electron interaction $E_{ee}[n(\boldsymbol{r})]$ can be furthermore separated into two parts:

$$\begin{aligned} E_{ee}[n(\boldsymbol{r})] &= \frac{1}{2}\iint \frac{n(\boldsymbol{r}_1)n(\boldsymbol{r}_2)}{r_{1,2}}\mathrm{d}r_1\mathrm{d}r_2 + E_{ncl}[n(\boldsymbol{r})] \\ &= J[n(\boldsymbol{r})] + E_{ncl}[n(\boldsymbol{r})] \end{aligned} \tag{3-13}$$

where $J[n(\boldsymbol{r})]$ is the classical Coulomb part, which is already well known, and the $E_{ncl}[n(\boldsymbol{r})]$ is the non-classical contribution to the electron-electron interaction including all the effects of self-interaction correction, exchange and Coulomb correlation.

The universal HK functional for a realistic system can be written as a separated form:

$$F_{HK}[n] = T_s[n] + J[n] + E_{xc}[n] \tag{3-14}$$

where $E_{\mathrm{xc}}[n]$ is the exchange-correlation energy, defined by comparing with equation (3-12) and (3-14):

$$E_{\mathrm{xc}}[n]=(T_{\mathrm{e}}[n]-T_{\mathrm{s}}[n])+(E_{\mathrm{ee}}[n]-J[n]) \tag{3-15}$$

Then, the exchange-correlation potential $V_{\mathrm{xc}}(\boldsymbol{r})$ can be formulated as

$$V_{\mathrm{xc}}[n]=\frac{\partial E_{\mathrm{xc}}[n(\boldsymbol{r})]}{\partial n(\boldsymbol{r})} \tag{3-16}$$

Kohn and Sham assumed a non-interacting electron system where the electrons behave as particles without Coulomb repulsion, and the electron density of a non-interacting system and that of a realistic system are equal ($n_{\mathrm{s}}(\boldsymbol{r})=n_0(\boldsymbol{r})$). This leads to an expression for the kinetic energy containing the single particle wave function φ_i:

$$T_{\mathrm{s}}=\sum_{i=1}^{N}\left\langle\varphi_i\left|-\frac{1}{2}\nabla^2\right|\varphi_i\right\rangle \tag{3-17}$$

The wave function $\varphi_i(\boldsymbol{r})$ is the Kohn-sham orbital, and the electron density in this system is $n(r)=\sum_i^N|\varphi_i(\boldsymbol{r})|^2$. Considering the single electron, the Hamiltonian here can be written as the Kohn-Sham equation in the form:

$$\left[-\frac{\hbar^2}{2m_{\mathrm{e}}}\nabla^2+V(\boldsymbol{r})+V_{\mathrm{H}}(\boldsymbol{r})+V_{\mathrm{xc}}(\boldsymbol{r})\right]\varphi_i(\boldsymbol{r})=\varepsilon_i\varphi_i(\boldsymbol{r}) \tag{3-18}$$

Here, the V is also appeared in Schrödinger equation (3-7), the V_H is the Hartree potential which is defined by $V_{\mathrm{H}}(r)=e^2\int\frac{n(\boldsymbol{r}')}{|\boldsymbol{r}-\boldsymbol{r}'|}d^3\boldsymbol{r}'$. Until now, the exchange-correlation potentials are unknown and need to be estimated by an appropriate way. It was

possible to solve this equation self-consistently because of Kohn-sham second theorem, by using a variational approach and a suitable expression for the exchange term. The key to solving the Kohn-Sham equation therefore lies in finding suitable exchange-correlation functionals [135, 136].

3.2.3 Exchange-Correlation functional

The essence of the DFT calculation is to first transform the multi-electron problem into multiple non-interacting single-electron problems without interaction, and then represent all the resulting deviations with a single exchange-correlation functional, which is taken out and analysed separately. The form of the exchange correlation functional E_{xc} is very important in finding the theoretical solution. However, since the actual form of this item is not known in practice, it is necessary to give its approximate form in each case. Perdew *et al.* constructed a concept of Jacob's ladder to describe the exchange-correlation functional [137, 138], as shown in the figure below.

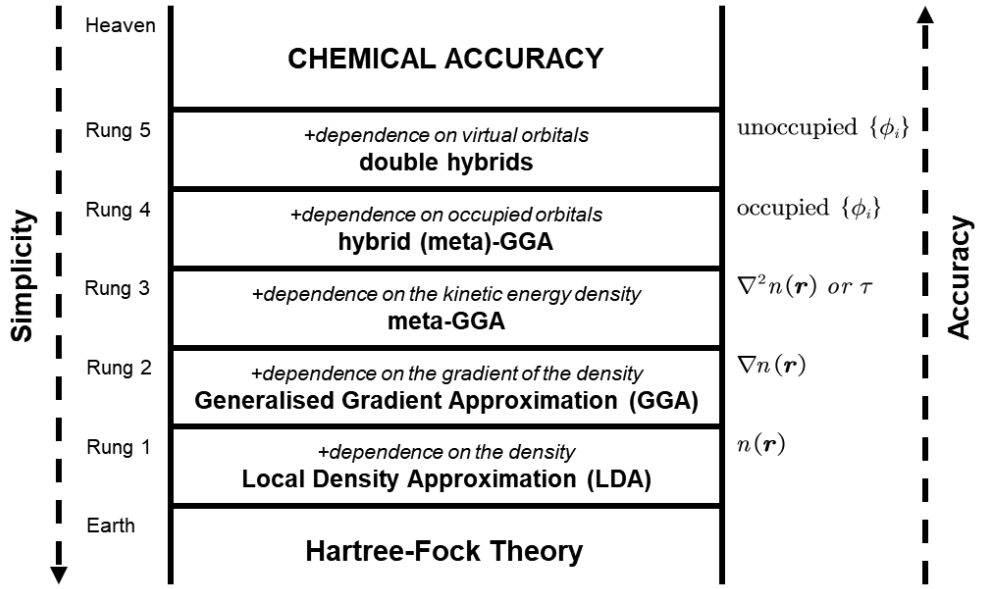

Figure 3.1 The Jacob's ladder describing the hierarchy of the exchange-correlation functionals. Remodified from references [137, 138].

The local density approximation (LDA) is the simplest approach to the functional, which introduces the uniform electron gas as the local electron density:

$$V_{\mathrm{xc}}^{\mathrm{LDA}}[n] = V_{\mathrm{xc}}^{\text{electron gas}}[n(\boldsymbol{r})] \tag{3-19}$$

The exchange-correlation energy of a uniform electron gas can be accurately obtained from quantum Monte Carlo or other methods. As the uniform electron gas approximation suggests, LDA is more accurate for materials with slowly varying valence charge densities, such as metals, but LDA tends to underestimate the exchange energy and overestimate the correlation energy, indicating that LDA is not satisfying in chemistry.

Considering the realistic interactions between electrons and nuclei, we can imagine that the electron density gradient would be the largest near nuclei and the electron density

gradient would approach zero far from nuclei. Thus, the next useful approximation to the functional is generalised gradient approximation (GGA) based on this idea, which includes information on the variation of electron density [139]. So the exchange-correlation functional can be expressed as

$$V_{\mathrm{xc}}^{\mathrm{LDA}}[n] = V_{\mathrm{xc}}[n(\boldsymbol{r}), \nabla n(\boldsymbol{r})] \tag{3-20}$$

As can be seen that more physical ingredients are included in the GGA functionals. Perdew–Wang 91 (PW91) functional [140] and the Perdew–Burke–Ernzerhof (PBE) functional [141] are two widely used nonempirical GGA functionals. Other methods on the higher rung of the Jacob's ladder may be more accurate, but they tend to cost more computational resources to calculate. The meta-GGA functionals are defined by including the second derivative of electron density $\nabla^2 n(\boldsymbol{r})$ or including the kinetic energy density $\tau(\boldsymbol{r})$ [142]. The hybrid functionals combine the HF approximation and DFT methods such as B3LYP, B3PW91, *etc* [143, 144]. This thesis mainly includes the discussion about transition mental carbide, and the comparison [107, 145] showed that the PBE functional is sufficient for this system.

3.2.4 van der Waals (vdW) correction

The conventional DFT approach could not provide information about weak van der Waals (vdW) interactions in either LDA or GGA since these methods have no term to account for dispersion. However, for a chemical system, the weak interactions have negligible contributions, especially for the layered materials or surface adsorption system. It is

useful to add a correction term to conventional DFT methods for considering the contribution from vdW, sometimes called DFT+D methods. The most popular vdW correction schemes are DFT-TS [146] (designed by Tkatchenko and Scheffler), DFT-D2 [147], and DFT-D3 [148] (later two are all designed by Stefan Grimme).

In this thesis, a modified version of DFT-D3 using Becke-Johnson damping, namely DFT-D3(BJ), is chosen to use a simple correction term representing the dispersion. The details would not be discussed here.

3.2.5 Bloch theorem and plane-wave method

For heterogeneous catalysis, a system contains not only the reactants and products, but also catalytic surfaces. Usually, we assume that the catalytic surface is homogeneous by applying the periodic boundary condition. The Kohn-sham orbitals can be expanded as a linear combination of basis functions. For periodic boundary conditions, a plane wave approach is more suitable for the system. Employing Bloch theorem together with plane waves for a periodic system [149], the wave function can be expressed as

$$\varphi_i(\boldsymbol{r}) = \sum_{\mathbf{G}} C e^{i(\mathbf{k}+\mathbf{G})\cdot\mathbf{r}} \tag{3-21}$$

where $\mathbf{G}$ is the reciprocal lattice vector, and $\mathbf{k}$ is a vector in *k*-space to the first Brillouin Zone. Each wave function in this case is characterised by a plane wave with a wave vector $\mathbf{k}$ in the first Brillouin zone of the supercell. The sampling of *k*-points is usually conducted by the method proposed by Monkhorst and Pack [150], which is used

in present thesis. The more *k*-points selected, the more accurate the calculation is expected to be, but also the more computationally intensive. Thus, to ensure convergence, it is necessary to test the size of the *k*-point mesh.

Such a simplification solves the problem of the infinite plane; however, the number of basis functions still limits the computation efficiency. To overcome this problem, the electronic potential is described using a pseudopotential [151], assuming that the valence electrons of each nucleus play key physical and chemical roles. In this thesis, the pseudopotential is implemented by the projector-augmented wave (PAW) method developed by Blöchl [152]. To make the computations feasible, one cannot include an infinite number of plane waves. Instead, a finite number is used, and this number is determined by the cutoff energy. In practical calculations, the choice of the cutoff energy is crucial. It is common practice to perform convergence tests, where calculations are repeated with increasing cutoff energies until the desired property (*e.g.*, total energy, atomic forces) converges to a stable value within a specified tolerance.

3.2.6 Transition state theory

For catalytic reactions, it is crucial to analyse chemical kinetics, reaction rates, and energy barriers. Transition State Theory (TST) is a cornerstone in the realm of chemical kinetics, offering a theoretical framework to understand the rates of chemical reactions, proposed independently by Henry Eyring [153], Meredith Gwynne Evans, and Michael Polanyi [154] in the 1930s. The theory posits that molecules must pass through a high-energy

configuration, known as the transition state, before a reaction can proceed. This ephemeral state, which exists for an infinitesimally short duration, is neither a reactant nor a product but a unique configuration representing the highest energy point along the reaction coordinate. By employing statistical mechanics, TST quantifies this rate, yielding the famous Eyring equation, which relates the rate constant of a reaction to temperature, activation energy, and other molecular parameters [155].

Within the DFT framework, the transition state is located by seeking the saddle point on the potential energy surface, corresponding to a maximum along the reaction coordinate and minima in all other orthogonal directions. Various algorithms, such as the nudged elastic band (NEB) and the climbing image NEB (CI-NEB) proposed by Henkelman *et al.*, have been developed to efficiently locate this saddle point, ensuring that the transition state adheres to the geometric and electronic criteria. NEB constructs a series of "images" or replicas of the system between the reactant and product states, and these images are then optimised to trace out the minimum energy path connecting them. This results in a detailed energy profile of the reaction, highlighting the transition state as the energy maximum [156]. To enhance the efficiency and accuracy of the NEB, the CI-NEB was introduced, while once the highest energy image (closest to the transition state) is identified during the NEB iterations, it is allowed to "climb" up the energy surface towards the exact transition state, ensuring a more precise characterisation of the saddle point. Once the transition state accurately determined, TST is then employed to compute the reaction rate.

The elementary reaction rate constant k, including temperature dependence, was calculated using harmonic transition state theory (hTST) [157].

$$k = \frac{k_B T}{h} \frac{q_{\mathrm{TS,vib}}}{q_{\mathrm{IS,vib}}} \exp\left(-\frac{E_a}{k_B T}\right) \tag{3-22}$$

where k_B stands for Boltzmann constant (1.381×10^{-23} J/K), h denotes Plank constant, T represents reaction temperature, E_a is the energy barrier for elementary reaction with zero-point energy correction calculated by DFT calculation, $q_{\mathrm{TS,vib}}$ and $q_{\mathrm{IS,vib}}$ represent the vibrational partition functions of the initial states and the transition states respectively, each the vibrational partition function (q_{vib}) can be calculated with the following equation:

$$q_{\mathrm{vib}} = \prod_i \frac{1}{1 - \exp(-h\nu_i / k_B T)} \tag{3-23}$$

where ν_i denotes the vibrational frequency of each vibrational mode of the surface adsorbing species derived from DFT harmonic frequency calculation. In this work, the frequencies lower than 50 cm^{-1} were varied to 50 cm^{-1} to remove the error due to low frequency.

3.2.7 Bader charge analysis

When a molecule adsorbs onto a catalytic surface, there is a redistribution of electron density between the molecule and the surface. This redistribution can influence the strength and nature of the adsorption, which can affect the subsequent reaction steps. Bader charge analysis [158], based on the Atoms in Molecules (AIM) theory proposed by Richard Bader, offers a rigorous approach to understanding the electronic structure of

systems, including those involved in surface adsorption processes in catalysis. Bader charge analysis divides the electron density of a system into discrete atomic basins, allowing for the assignment of charges to individual atoms. This partitioning is based on the topology of the electron density, with boundaries defined by zero-flux surfaces in the electron density gradient [158]. Thereby, the oxidation or reduction characteristics of the surface adsorption can be determined by comparing the variation of the partitioned charge before and after adsorption. The detailed derivation of the equations will not be reviewed here, as the software package developed by Henkelman has access to information on valence electrons [159]. In this thesis, the degrees of surface oxidation by adsorbates at different coverages are calculated based on Equation (3-24) [108]:

$$OX_{atom} = \left(\sum_{i=1}^{n} Z_{\mathrm{val},i}^{\mathrm{atom,clean}} - \sum_{i=1}^{n} Z_{\mathrm{val},i}^{\mathrm{atom,ads}} \right) \Big/ \sum_{i=1}^{n} Z_{\mathrm{val},i}^{\mathrm{atom,clean}} \qquad (3\text{-}24)$$

where n is the number of Mo or C atoms in the topmost layer (n = 9 in Figure 4.1), and $Z_{\mathrm{val},i}^{\mathrm{atom,ads}}$ and $Z_{\mathrm{val},i}^{\mathrm{atom,clean}}$ are the numbers of valence electrons possessed by each Mo or C atom of the topmost layer in the clean model and the model with adsorbates, respectively. The number of valence electrons was computed using Bader charge partitioning. [158, 159] A positive OX_{atom} value means electron loss while a negative OX_{atom} value stands for electron gain.

3.3 Ab initio molecular dynamics

Molecular adsorption, as molecules adhere to surfaces, plays a pivotal role in the heterogeneous catalysis. Understanding dynamics, energetics, and mechanisms of

molecular adsorption at the atomic and electronic levels is crucial for harnessing and optimising these catalysts. Based on the DFT calculations, *ab initio* molecular dynamics (AIMD), as a computational method, has revolutionised our ability to "probe" molecular adsorption phenomena [160, 161]. Particularly for the water-gas shift reaction studied in this thesis, the molecular adsorption location on the α-MoC surface is well worth discussing since the adsorption sites for surface species (OH*, O*) are controversial. Excluding unstable adsorption sites in advance can drastically reduce the computational effort and lead to useful conclusions. Unlike classical molecular dynamics, which relies on predefined empirical potentials, AIMD derives forces directly from quantum mechanical calculations, typically using DFT. Due to their small mass, electrons respond much more quickly to changes in their environment and exhibit quantum behaviour over the length scales and timescales of molecular dynamics simulations. In contrast, as Born-Oppenheimer approximation, nuclei move more slowly, and their motion can often be well-approximated using classical physics over these scales. The motion of the nuclei is governed by Newton's second law:

$$M_I \frac{d^2 \boldsymbol{R}_I}{dt^2} = -\nabla_{\boldsymbol{R}_I} E \tag{3-25}$$

where M_I is the mass of nucleus I, $\boldsymbol{R}_I$ is the position of nucleus I, E is the total energy of the system, which is in terms of the electron density and can be calculated by DFT. These forces are then used to update the atomic positions and velocities using a suitable integration algorithm, such as the Verlet algorithm [162]. At each time step, the

positions of the nuclei are updated based on these forces. However, before the forces can be computed, the electronic structure must be determined for the current nuclear configuration. This is where the iterative procedure comes into play:

Step 1 – Initialization: Begin with an initial guess for the electron density, $n^{(0)}(\boldsymbol{r})$.

Step 2 – Solve for Electronic Structure: With the initial guess, solve the Kohn-Sham equations to obtain the electronic wavefunctions $\psi_i(\boldsymbol{r})$.

Step 3 – Update Electron Density: The electron density is updated to $n^{(N+1)}(\boldsymbol{r})$ based on the obtained wavefunctions.

Step 4 – Convergence: Determine the difference between the updated electron density and the previous iteration: $\Delta n = \int |n^{(N+1)}(\boldsymbol{r}) - n^{(N)}(\boldsymbol{r})| d\boldsymbol{r}$. If Δn is below a predefined threshold, the electronic structure is considered converged for this time step.

Step 5 – Move Nuclei: With the forces derived from the converged electronic structure, the positions of the nuclei are updated using the Verlet algorithm.

Step 6 – Repeat: For the next time step, return to step 2, using the updated nuclear positions and the converged electron density from the previous time step.

This iterative procedure ensures that at each time step of the molecular dynamics simulation, the electronic structure is consistent with the positions of the nuclei, allowing AIMD to capture dynamic processes involving changes in electronic structure. The correct time step selection, such that the phase space is efficiently sampled, is an important question in molecular dynamics. In practical implementations, the chosen time

step should be capable of capturing the shortest period of motion in the system, which is usually about one-tenth of the motion period, as a general rule of thumb. Maximum vibrational frequencies in a system containing hydrogen are in the range of 10^{14} Hz, suggesting that a 1 fs ($=10^{-15}$ s) time step is appropriate.

When AIMD simulations are performed under conditions where the temperature needs to be maintained constant, the canonical ensemble becomes relevant [163]. However, due to the deterministic nature of classical dynamics and the quantum mechanical calculations for the forces, without any external intervention, the system would not naturally sample the canonical ensemble. This is where thermostats used, and specifically those compatible with AIMD, come into play. Thermostats in AIMD are algorithms designed to ensure that the system remains at a constant temperature, effectively simulating the presence of a heat bath and allowing the system to sample from the canonical ensemble. Given the quantum nature of the forces in AIMD, not all classical thermostats are suitable. Thermostats like the Nosé–Hoover [164, 165] or the Langevin are often employed in AIMD to ensure the system samples the canonical ensemble while accounting for the quantum-derived forces. In this work, a canonical ensemble with Nosé–Hoover thermostats with the time step of 1 fs was implemented to carry out the AIMD.

3.4 *Ab initio* thermodynamics

In heterogeneous catalysis, the catalyst and reactants are in different phases. Thus understanding the intricate details of catalytic reactions at the molecular levels under

realistic conditions is crucial for the chemical engineer. In this context, Reuter and Scheffler developed a framework called *ab initio* thermodynamics (AIT) to predict the stability of different adsorbed structures, reaction intermediates, and phases on surfaces under a given environment at finite temperature and pressure of gas phase [116, 117, 166-168], combining first-principles calculations such as DFT with classical thermodynamics to predict the thermodynamic properties. This method assumes that the catalytic surface is in thermodynamical equilibrium with the gas phase environment. The stability of different structures is then assessed by comparing thermodynamic potentials. For a system under constant temperature and pressure, the Gibbs free energy (G) is the relevant thermodynamic potential. The Gibbs free energy of entire system can be broken down into three parts as follows:

$$G = G_{\text{solid}} + G_{\text{gas}} + \Delta G_{\text{surf}} \tag{3-26}$$

where G_{solid} is the Gibbs free energy contributed by the solid phase, G_{gas} is that contributed by the gas phase and ΔG_{surf} is that contributed by the adsorption process. In thermodynamics, the most stable phase structure of the adsorption process would minimise the surface Gibbs free energy ΔG_{surf}. We now can obtain following expression upon the rearrangement of equation (3-26) [169]:

$$\Delta G_{\text{surf}} = G - G_{\text{solid}} - G_{\text{gas}} \tag{3-27}$$

When the clean catalytic surface slab is adsorbed with adsorbates, the stability $\gamma(T,p)$ of different surface phase structures consisting of i surface species (adsorbates) at

temperature T and pressure p is defined as follow:

$$\gamma(T,p) = G_{\text{ads}}^{\text{slab}}(T,p) - G_{\text{clean}}^{\text{slab}}(T,p) - \sum_i (n_i \times \mu_i(T,p)) \quad (3\text{-}28)$$

where the $G_{\text{ads}}^{\text{slab}}(T,p)$ is the Gibbs free energy of the catalyst model with adsorbates, $G^{\text{slab}}(T,p)$ is the Gibbs free energy of the clean catalyst model and $\mu_i(T,p)$ is the chemical potential of isolated specie i. A more negative $\gamma(T,p)$ denotes a more stable surface structure. For the condensed phases, the vibrational energy and entropy contributions to the Gibbs free energy usually cancel to a large extent in the subtraction term $G_{\text{ads}}^{\text{slab}}(T,p) - G_{\text{clean}}^{\text{slab}}(T,p)$. With considering only the thermal correction to the adsorbates, the term $G_{\text{ads}}^{\text{slab}}(T,p) - G_{\text{clean}}^{\text{slab}}(T,p)$ can be replaced by $E_{\text{ads}}^{\text{slab,ZPE}}(0\text{K}) + \Delta G_{\text{ads}}(T) - E_{\text{clean}}^{\text{slab}}(0\text{K})$, where $E_{\text{ads}}^{\text{slab,ZPE}}(0\text{K})$ is the ZPE-corrected total energy of the catalyst model with adsorbates, $E_{\text{clean}}^{\text{slab}}(0\text{K})$ is the total energy of the clean catalyst model, $\Delta G_{\text{ads}}(T)$ is the thermal correction to the adsorbates, which is calculated according to the following equation as implemented in VASPKIT software [170]:

$$\Delta G_{\text{ads}}(T) = -RT \ln q_{\text{vib}}^{\text{ads}} \quad (3\text{-}28\text{a})$$

where $q_{\text{vib}}^{\text{ads}}$ is the vibrational partition function for adsorbates and can be calculated as (3-23). Please note that in some literature the RT term may also be written as $N_A k_B T$, although they are equivalent. Thus, equation (3-28) can be simplified as below:

$$\gamma(T,p) = E_{\text{ads}}^{\text{slab,ZPE}}(0\text{K}) + \Delta G_{\text{ads}}(T) - E_{\text{clean}}^{\text{slab}}(0\text{K}) - \Sigma_i (n_i \times \mu_i(T,p)) \quad (3\text{-}28\text{b})$$

For the gas phase (assuming ideal gas), the chemical potential of species i depending on temperature and pressure, can be expressed below:

$$\mu_i(T,p) = E_i^{\mathrm{ZPE}}(0\,\mathrm{K}) + \tilde{\mu}_i(T,p^0) + RT\ln(p_i/p^0) \tag{3-28c}$$

where $E_i^{\mathrm{ZPE}}(0\,\mathrm{K})$ is the total energy of isolated species i with ZPE correction obtained from DFT calculation, $\tilde{\mu}_i(T,p^0)$ is the energy difference between the chemical potential (temperature T and pressure 1 atm) and total energy at 0 K for species i, p_i is the partial pressure of species i, p^0 is the standard atmospheric pressure, $\tilde{\mu}_i(T,p^0)$ values are taken from the JANAF thermochemical tables (https://janaf.nist.gov/) [171]. Combining equations (3-28b) and (3-28c), the following expression can be obtained:

$$\begin{aligned}\gamma(T,p) = {} & E_{\mathrm{ads}}^{\mathrm{slab,ZPE}}(0\,\mathrm{K}) + \Delta G_{\mathrm{ads}}(T) - E_{\mathrm{clean}}^{\mathrm{slab}}(0\,\mathrm{K}) \\ & - \Sigma_i(n_i \times E_i^{\mathrm{ZPE}}(0\,\mathrm{K})) - \Sigma_i\left(n_i \times \tilde{\mu}_i(T,p^0)\right) \\ & - RT\Sigma_i(n_i \times \ln(p_i/p^0))\end{aligned} \tag{3-28e}$$

where the surface stability with i number gas phase species can be evaluated.

For the liquid phase, the chemical potential of species j depending on temperature and pressure can be expressed below:

$$\mu_j(T,p) = E_j^{\mathrm{ZPE}}(0\,\mathrm{K}) + \tilde{\mu}_j(T,p^0) + RT\ln\frac{p_j^{\mathrm{sat}}}{p^0} + V_j(p_j - p_j^{\mathrm{sat}}) \tag{3-28d}$$

where p_j^{sat} is the saturated vapour pressure of species j at temperature T, V_j is the unit volume of liquid phase j at temperature T.

Combining equations (3-28b) and (3-28d), the following expression can be obtained:

$$\begin{aligned}\gamma(T,p) = & E_{\text{ads}}^{\text{slab,ZPE}}(0\text{K}) + \Delta G_{\text{ads}}(T) - E_{\text{clean}}^{\text{slab}}(0\text{K}) \\ & - \Sigma_{i+j}\left(n_{i+j} \times E_{i+j}^{\text{ZPE}}(0\text{K})\right) - \Sigma_{i+j}\left(n_{i+j} \times \tilde{\mu}_{i+j}(T,p^0)\right) \\ & - RT\Sigma_i\left(n_i \times \ln\left(p_i/p^0\right)\right) - RT\Sigma_j\left(n_j \times \ln\left(p_j^{\text{sat}}/p^0\right)\right) \\ & - \Sigma_j\left(n_j \times V_j\left(p_j - P_j^{\text{sat}}\right)\right)\end{aligned} \tag{3-28f}$$

where the surface stability with i number gas phase species and j number liquid phase species can be evaluated.

When the energy terms are able to be calculated by DFT methods, we can naturally define the average binding energies for different adsorbing species as follows:

$$E_i^{\text{AVG, }n} = 1/n \times \left(E_{\text{ads}}^{\text{slab,ZPE}}(0\text{K}) - E_{\text{clean}}^{\text{slab}}(0\text{K}) - n \times E_i^{\text{ZPE}}(0\text{K})\right) \tag{3-29}$$

where $E_i^{\text{ZPE}}(0\text{K})$ is the ZPE-corrected total energy of isolated species i, and n is the number of adsorbing species i.

3.5 Energetic span model

Researchers and industry professionals relied on varied and often non-standardised methods to gauge catalytic activity for various catalysts, which makes it difficult to compare results across different studies. Moreover, without a clear metric, it was challenging to determine the effectiveness of a catalyst in accelerating a reaction, especially when considering the role of active sites. The absence of a standardised measure also hindered the optimisation of catalytic processes, as there was no clear benchmark to aim for or measure against.

The introduction of the turnover frequency (TOF) can address these challenges head-on,

offering a universal standard to assess the catalytic activity that could be applied across various catalytic systems and conditions [172]. It is defined as the number of catalytic cycles that each active site on a catalyst can complete per unit of time. Mathematically, TOF can be represented as:

$$\text{TOF} = \frac{\text{Number of product molecules formed}}{\text{Number of active sites on the catalyst} \times \text{Time}} \tag{3-30}$$

Here, the number of product molecules formed is the total number of product molecules produced in a given time, and the number of active sites refers to the number of catalytically active sites available on the catalyst. Considering the entire catalyst, the TOF can be rewritten as:

$$\text{TOF} = \frac{\text{Rate of product formation}}{\text{Number of active sites on the catalyst}} \tag{3-31}$$

The concept of TOF not only facilitates a more accurate comparison of different catalysts but also provides deeper insights into the intricacies of catalytic reactions. If we have the kinetic rate of the reaction, we can express TOF as:

$$\text{TOF} = \frac{r}{[C] \times n_s} \tag{3-32}$$

where r is the kinetic rate of the reaction (*e.g.*, moles of product formed per liter per second, mol/L·s), $[C]$ is the concentration of the catalyst (*e.g.*, moles of catalyst per liter, mol/L) and n_s is the number of active sites per mole of catalyst (*e.g.*, sites/mol). The reaction rate in many catalytic reactions can be expressed using rate laws derived

from the reaction mechanism as the function of reaction rate constant and concentrations of reactants. However, the traditional model focuses on the energy barrier of the rate-determining step to predict catalytic activity and it can sometimes oversimplify multi-step reactions [120]. Many catalytic reactions involve multiple steps, each with intermediates and transition states. For such reactions, the rate-determining step alone might not provide a comprehensive picture of the overall reaction kinetics.

In organic chemistry, the concept of the reactivity-selectivity principle, also known as the Hammond postulate, suggests that the structure of a transition state resembles either the reactants or the products, depending on which is higher in energy. Sebastian Kozuch and Jan M. L. Martin extended this idea to catalysis, suggesting that the entire reaction pathway, including both forward and reverse barriers, should be considered. And they proposed the Energy Span Model (ESM) in the context of understanding and predicting catalytic activity [121]. This model employs the fact that neither the highest transition state nor a single elementary reaction step could always determine the efficiency of a catalytic cycle [122, 123]. They posited that the energetic span, defined as the energy difference between the highest transition state and the most stable intermediate along the reaction pathway, is a crucial determinant of catalytic activity.

The primary assumption of the ESM is that reactions with a smaller energetic span are generally more catalytically active, leading to higher TOFs. This is because both the forward and reverse barriers (from the stable intermediate to the transition state and vice versa) play a role in determining the overall reaction rate. If the energetic span is

minimised, the barriers to both forward and reverse reactions are reduced, leading to faster reaction rates and higher TOFs. The ESM identifies two states, TOF-determining transition state (TDTS) and TOF-determining intermediate (TDI), possessing the largest degree of control on TOF. The TDTS and TDI are not necessarily the highest and lowest states among the many states in the catalytic cycle, nor do they always appear within one single step. The TDTS-TDI energy difference and the reaction energy of the catalytic cycle define an energetic span which determines TOF. Originally developed for organic metal complexes (OMCs), the applications of ESM in single atomic catalysts (SACs) have increasingly progressed owing to the structural and conceptual similarities between the ligand-bond transition metal centre of OMCs and the support-bound atomic site of SACs [173-175].

The efficiency of explored reaction routes can be evaluated by TOFs, which were calculated from their respective free energy profiles using the ESM. The TOF expression of the ESM within the steady-state assumption is as follows:

$$\mathrm{TOF} = \frac{k_B T}{h} \frac{e^{-\Delta G_r/RT} - 1}{\sum_{i,j=1}^{N} e^{(T_i - I_j - \delta G_{i,j})/RT}} \tag{3-33}$$

where k_B, h and R are Boltzmann, Planck and gas constants, respectively; T is the reaction temperature; ΔG_r is Gibbs free energy of reaction at given temperature and pressure; T_i and I_j are the free energies of the i^{th} transition state and j^{th} intermediate, respectively. The value of $\delta G_{i,j}$ depends on the ordering of T_i and I_j along the N-step catalytic cycle. If T_i appears after I_j, then $\delta G_{i,j}$ takes the value of

ΔG_r, otherwise 0.

$$\delta G_{i,j} = \begin{cases} \Delta G_r & \text{if } i \geq j \\ 0 & \text{if } i < j \end{cases} \tag{3-34}$$

For many cases, only one transition state and one intermediate among the many states in the catalytic cycle determine the TOF, namely, the TDTS and the TDI. These key states can be located by assessing the normalised degree of TOF control (X_{TOF}) as follows:

$$X_{\mathrm{TOF},\,T_i} = \frac{\sum_j e^{(T_i - I_j - \delta G_{i,j})/RT}}{\sum_{ij} e^{(T_i - I_j - \delta G_{i,j})/RT}};\; X_{\mathrm{TOF},\,I_j} = \frac{\sum_i e^{(T_i - I_j - \delta G_{i,j})/RT}}{\sum_{ij} e^{(T_i - I_j - \delta G_{i,j})/RT}} \tag{3-35}$$

The normalised X_{TOF,T_i} and X_{TOF,I_i} are both in the range of [0, 1]. Only state with significant X_{TOF} value (usually approaching 1) can be identified as TDTS or TDI. Once determined, the energetic span δE is defined as:

$$\delta E = \begin{cases} T_{\mathrm{TDTS}} - I_{\mathrm{TDI}} & \text{if } TDTS \text{ appears after } TDI \\ T_{\mathrm{TDTS}} - I_{\mathrm{TDI}} - \Delta G_r & \text{if } TDTS \text{ appears before } TDI \end{cases} \tag{3-36}$$

3.6 Computational details

The overall methodology was based on DFT calculations with several appropriate numerical corrections. Then, the surface phase evolution of the catalytic surface under the H_2/H_2O atmosphere was simulated based on *ab initio* thermodynamics and reaction rate constants (kinetics). Finally, the TOF derived from ESM was calculated for yielding

the reaction route on different surfaces.

3.6.1 Electronic structure calculations

Periodic density functional theory (DFT) calculations were carried out employing the plane-wave-based Vienna *ab initio* simulation package (VASP) code [176, 177]. The influence of ionic cores on the valence electrons was accounted for by the projector augmented wave (PAW) method, as implemented by Kresse *et al.* [152, 178]. The residual Hellmann-Feynman forces on the atoms converged to 0.02 $eV \cdot Å^{-1}$ in the atomic structure relaxations to obtain the energies and geometries of the most stable configurations, while the total energy converged to 10^{-4} eV in the electronic minimisation. The Perdew-Burke-Ernzerhof functional of generalised gradient approximation (GGA-PBE) [141], which was broadly recognised to be well suited for the molybdenum carbides catalysts, was selected to depict the exchange and correlation of electrons [48, 66, 98, 108, 113, 118, 179]. The Kohn-Sham equations were solved using a plane-wave basis with an energy cut-off of 415 eV, the value of which was validated to be appropriate to get converged calculations for the catalysis on carbides [107, 114] and was also validated in the later section. A 10×10×10 Γ-centred Monkhorst-Pack [150] mesh grid was used in bulk fcc MoC optimisation for the first Brillouin zone *k*-point sampling. The Gaussian electron smearing method with a smearing width σ of 0.05 eV was used to ensure energy errors within 1 meV per atom.

3.6.2 Transition state calculations

The structures of transition states were mainly located *via* the dimer method [180, 181], and occasionally, the climbing image nudged elastic band (CI-NEB) [156, 182] method was also used. The dimer method and CI-NEB have been incorporated in to the VASP as VTST (Transition State Tools for VASP).

The harmonic frequencies of adsorbates and isolated molecules were calculated by the central difference method. All frequencies of the local minimum were real, whereas one imaginary frequency emerged in each transition state, which was further confirmed to vibrate in the desired direction as visualised by the Jmol software [183].

3.6.3 Correction of calculations

The vdW correction [148] with Becke-Johnson damping [184] (DFT-D3(BJ)) was implemented in order to consider van der Waals interactions by adding the corrected terms to the electronic energies.

Zero-point energy (ZPE) corrections were added to the electronic energy at 0 K, while the entropy corrections were also included for higher temperatures. Both the ZPE and entropy corrections were calculated using VASPKIT [185] software based on the harmonic frequencies.

3.6.4 Convergence test

Although there is already a large amount of literature on similar systems or even the same

system giving cutoff values for the valence electron wavefunction basis set during calculations, this thesis cautiously validated the choice of energy cutoff. Energy-cutoff testing for fcc MoC with the adsorption energy of OH* and H_2O* under different energy-cutoff calculations was carried out.

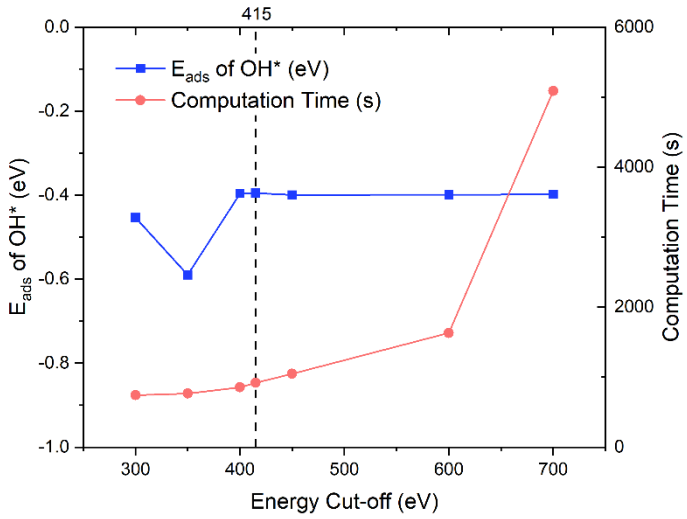

Figure 3.2 Energy cut-off testing for the binding energy of OH* on fcc MoC.

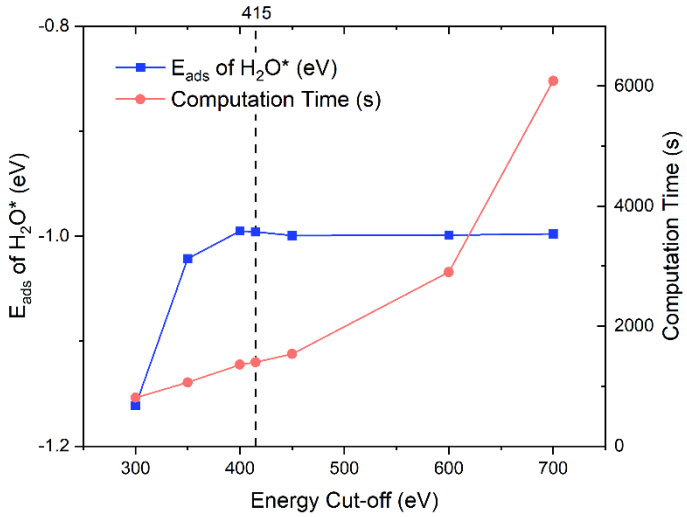

Figure 3.3 Energy cut-off testing for the binding energy of H_2O* on fcc MoC.

From the above results, it can be seen that the selection of energy cut-off in this thesis (415 eV) provides a better balance between accuracy and computational cost.

Chapter 4 Results and Discussion (I): Surface phase evolution

Metal-doped fcc MoC catalysts recently showed unprecedented reactivity in the low-temperature water-gas shift reaction for H_2 production. However, the structure-reactivity relationship was still obscure due to the complexity of the surface chemistry, and the synthesised fcc MoC often exhibited both (111) and (001) facets [48, 66, 68, 91]. The situation is even more complicated due to the surface phase structure evolving during the reaction, leading to distinct performances from the original surfaces.

As reviewed in Chapter 2, the surface phase on the (111)-Mo surface under the H_2O/H_2 atmosphere has an influence on the physicochemical properties of the surface and consequently on the relevant reactions (WGS, MSR, *etc.*) [108]. A parallel study of the (001) surface is a prerequisite for comprehensive studying of low temperature water-gas shift reactions on Pt_1/fcc MoC.

In this chapter, the surface phase evolution on the (001) surface in an H_2O/H_2-rich atmosphere is studied from kinetic and thermodynamic aspects. The stable configurations of surface species (H_2O*, OH, O*, H_2*, and H*) at various levels of coverage and their formation rates considering coverage effects were investigated on the (001) surface. The DFT and the transition state theory were employed to calculate the energy profiles and reaction rates, respectively, while the *ab initio* atomistic thermodynamics were employed to identify the stable configurations of the surface phase. The detailed method and model

have already been clearly illustrated in the previous Chapter 3. At the end of this chapter, we will summarise that how the surface species evolved on the (001) surface under the mixture of H_2O and H_2. Unless otherwise mentioned, the results of (111)-Mo cited from ref. [108] for the purpose of comparison between (001) and (111)-Mo, while such comparison is necessary for the later comprehensive studies in Chapters 6 and Chapter 7 of the WGS reaction through Pt-doped fcc MoC.

4.1 Model setup

4.1.1 fcc MoC (001) surface

A periodic supercell slab model, referenced and adjusted from an optimised bulk structure by Jimenez-Orozco *et al.* [114], was constructed to simulate the fcc MoC (001) surface. This slab model contains six layers of atoms and was verified in similar systems, including the adsorption energies with slab thickness on (001) [114] and the hydrocarbon interaction on tungsten carbide [186].

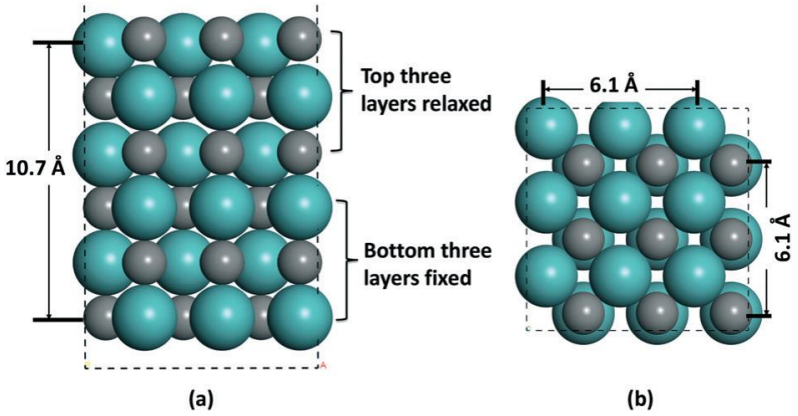

Figure 4.1 Surface slab model of fcc MoC (001) in (a) side view and (b) top view (green balls represent Mo atoms; grey balls represent C atoms).

As shown in Figure 4.1, the three bottommost atomic layers were fixed to provide an appropriate environment for the other fully relaxed atomic layers in the employed supercell. There are 9 Mo atoms and 9 C atoms in each layer, and a vacuum gap of 15 Å was created between the periodic slabs to avoid interactions with the neighbour slab in the direction perpendicular to the surface. The first Brillouin zone of this slab model was sampled using a 4×4×1 Γ-centred Monkhorst–Pack mesh grid [150].

4.1.2 Simulation conditions

Ab initio thermodynamics was used to calculate the (001) surface phase diagram. The calculated phase diagram pressures were from 10^{-10} to 10 MPa for the H_2 partial pressure and from 10^{-3} to 10 MPa for the H_2O partial pressure, where 1.553 is the critical point for the gas-liquid phase of water. The temperature of 473.15 K was used to construct the phase diagram to facilitate comparison with the reported experiments and to provide a more reliable investigation.

4.2 Results and discussion of molecular H_2O adsorption

No matter the mechanism, the dissociation of water is the most important first step in the water-gas shift reaction, giving the surface oxygenated species. There are nine possible sites for the adsorption of water molecules on the (001) surface. The most stable configurations of H_2O adsorption on the (001) surface at different monolayer (ML) coverages from 1/9 to 1 ML were illustrated in Figure 4.2. The parenthesis below each subfigure noted the average binding energy (eV) of water with ZPE correction and surface

oxidation degree (%) of Mo sites and C sites, respectively.

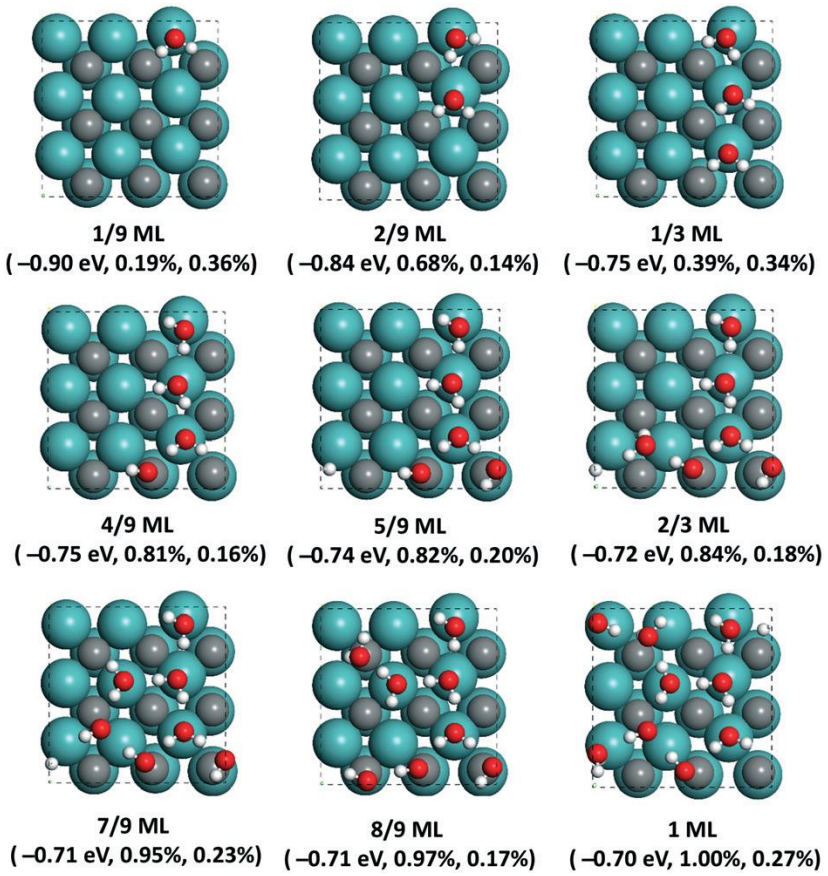

Figure 4.2 The H_2O adsorption configurations on the fcc MoC (001) surface.

The O atom of the first adsorbed water molecule (n = 1, 1/9 ML) coordinated with the Mo atom with a distance of 2.33 Å while the two O–H bonds were parallel to the two Mo–C bonds, similar to the Mo/C mixed (101) surface of hexagonal Mo_2C [187]. The H atoms had a slight negative charge, preferring approaching positively charged Mo sites (averagely at +1.193e), and the O atom had a slight positive charge, preferring approaching the negatively charged C sites (averagely at −1.193e). With the adsorption of H_2O, the Mo site was oxidised as the charge of the Mo site increased by 0.166e. The average binding energy of the first water molecule on the (001) surface of fcc MoC is

−0.90 eV, which was close to that on the molybdenum-terminated (111) surface of the fcc MoC (−0.87 eV) [108] and that on the MXene (0001) surface of the Mo_2C (−0.92 eV) [188], but it showed more stability than the mixed Mo/C (101) surface of hexagonal Mo_2C with a binding energy of −0.52 eV [187]. The configuration of water adsorption while the coverage increased no more than 1/3 ML was similar to that of 1/9 ML coverage, except for the formation of weak hydrogen bonds between water molecules. The hydrogen bond formed had average lengths of 2.27 Å at 2/9 ML and 2.25 Å at 1/3 ML. In contrast, it was found [108] that the average hydrogen bond length on the (111)-Mo surface was 1.88 Å at 2/9 ML and that was 1.85 Å at 1/3 ML, which indicated the formation of stronger hydrogen bonds on the (111)-Mo surface than those on the (001) surface. As the surface continued to adsorb H_2O, the role of hydrogen bond interactions gradually became apparent. As the coverages increased from 4/9 ML to 1 ML, the average hydrogen bond lengths ranged from 1.78 Å to 1.95 Å, significantly stronger than those of the coverages from 1/9 ML to 1/3 ML.

As shown in Figure 4.2, the average adsorption energies decreased as the increase of adsorbed H_2O on the MoC (001) surface. By contrast, those on the (111)-Mo surface displayed a volcano curve as the rising of adsorbed H_2O coverage [108]. Also, the average adsorption energy on (111)-Mo is smaller than on the (001) surface, suggesting that the absorption strength on the (001) surface is slightly weaker. The water-adsorbed surfaces were oxidised to varying degrees. The more water adsorbed, the more the oxidation of the Mo sites increased, but there was no linear pattern in the oxidation of the C sites.

4.3 Results and discussion of surface phase species

4.3.1 Formation of surface OH* *via* H_2O* dissociation

(1) Different levels of H_2O* coverage

The H_2O* dissociation on the (001) surface, considering the coverage level of H_2O*, was studied based on the most stable configurations of the adsorbed water on the (001) surface.

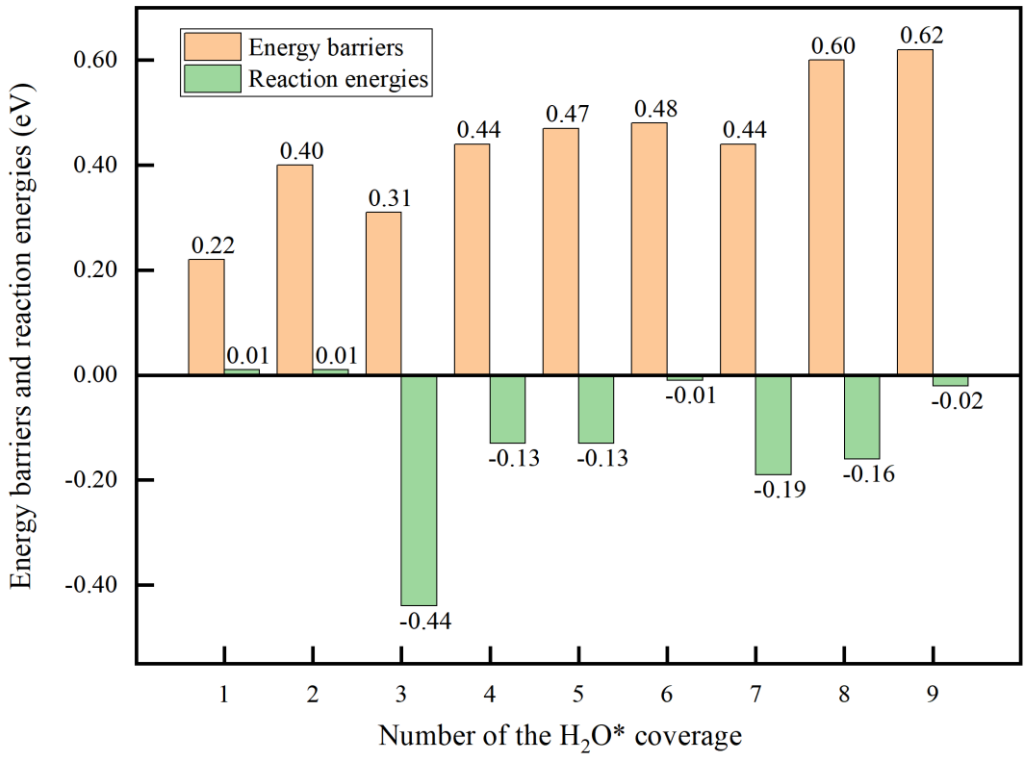

Figure 4.3 Energy barriers and reaction energies for H_2O*dissociation with *n* H_2O* adsorption.

Figure 4.3 presents the Boltzmann averaged energy barriers and reaction energies [189] with adsorbed H_2O* coverage levels from 1/9 ML to 1 ML. The H_2O adsorption states were selected as the reference. The Boltzmann averaged energies were calculated by

$E = \sum_{i=1}^{m}[E_i \exp(-E_i/RT)]/\sum_{i=1}^{m}[\exp(-E_i/RT)]$, where E_i is the energy barrier or reaction energy of one water dissociation site, and there are m different sites at a specified coverage. The results including the potential energy profile and the detail energetic aspects are summarised in Figure S1 and Table S1.

On the (001) surface, the activation of the O–H bond in H_2O* was mainly occurred by the Mo–C pair site while the H* adsorbed on the C site and the O* adsorbed on the Mo site, respectively (Figure S1). The average length of O–H bond of the adsorbed water molecule was 1.33 Å in the transition state, and the average distance of C···H was 1.36 Å, indicating the formation of the C–H bond (Table S1). The dissociated H atom adsorbed on the C site had an average distance of 1.11 Å while the OH* group remained on the Mo site with an average Mo–OH bond length of 2.14 Å.

The H_2O* dissociation was kinetically facile on the (001) surface at 1/9 ML, with an energy barrier of only 0.22 eV, whereas that on the (111)-Mo surface was 0.33 eV [108]. Besides, the reaction energy on the (001) surface was 0.01 eV, exhibiting an exothermic process, but that on the (111)-Mo surface was −1.01 eV [108]. When the coverage of H_2O* on the (001) surface rose from 1/9 to 1 ML, the energy barriers increased within the range of 0.22 to 0.62 eV in a staged trend. In contrast, those on the (111)-Mo surface showed a rapid decrease from 0.33 to 0.08 eV as the coverage raised to 1/3 ML and then a slow decrease to 0.03 eV as the coverage was raised further [108]. Averaging the energy barriers over the whole range of different coverages, the averaged energy barrier on the (001) surface is significantly higher than on the (111)-Mo surface (0.44 eV *vs.* 0.12 eV)

(Table S1) [108]. On the other hand, the reaction energies on the (001) surface were with values between ~0 and −0.2 eV, showing weak exothermicity. However, those on the (111)-Mo surface exhibited obvious exothermicity, ranging from −1.0 to −2.0 eV [108].

As described, both the (001) surface and (111)-Mo surface could dissociate adsorbed water molecules easily to form surface OH* species, while the OH* species were more facile to be generated on the (111)-Mo surface.

(2) Different levels of OH* coverage

The adsorbed H_2O* can also be dissociated on the (001) surface with formed OH*.

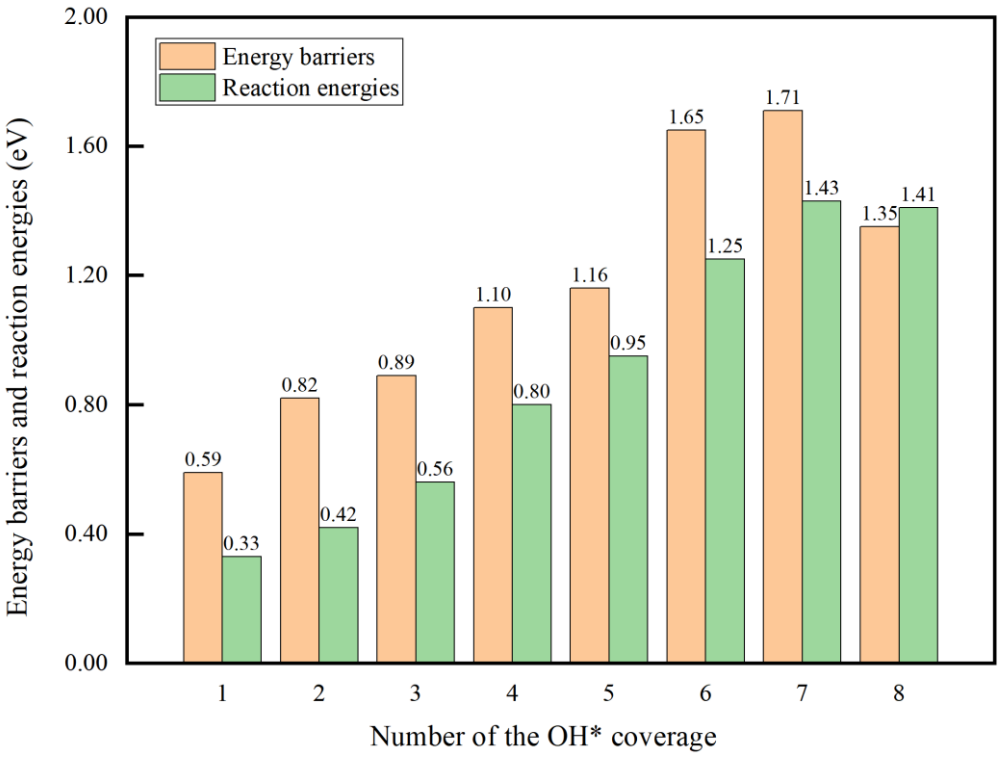

Figure 4.4 Energy barriers and reaction energies for H_2O* dissociation with *n* OH* adsorption.

Figure 4.4 presented the Boltzmann averaged energy barriers and reaction energies over those of H_2O* dissociation at various OH* coverages from 1/9 ML to 8/9 ML. The H_2O adsorption states were selected as the reference. The results including the potential energy profile and the detailed energetic aspects are summarised in Figure S2 and Table S2.

The activation mode of an adsorbed water molecule on the (001) surface with OH* was similar to that on the surface with H_2O* discussed previously. The main events in this activation were breaking the O–H bond and forming the C–H bond. However, breaking the O–H bond had a longer average length when interacting with OH* species (1.41 Å) than when interacting with H_2O* (1.33 Å) during the transition state, as illustrated in Table S1 and Table S2. This inspired the possibility that the reaction would become more difficult due to the larger structure change during the transition states. Comparing the results in Figure 4.3 and 4.4, it can be seen that the transition states for the H_2O* dissociation with OH* adsorbed have higher energy barriers for activation of the O–H bond than the case with H_2O* adsorbed. As the OH* coverage increased, the energy barrier of the H_2O* dissociation also increased, and it would be greater than 1 eV when the OH* species coverage was greater than 1/3 ML. In this case, it can be concluded that the high OH* coverage makes the H_2O* dissociation on the (001) surface kinetically difficult. Moreover, the increasing reaction energy from 0.33 to 1.41 eV also indicates that the dissociation of H_2O* on the (001) surface was thermodynamically unfavourable as the OH* coverage increased.

The energy barrier and reaction energy displayed in Figure 4.4 were processed by

Boltzmann-averaging over several possible configurations with different interactions between H_2O* and OH*. As a matter of fact, the H_2O* dissociation was affected by the interactions between dissociating H_2O* and adsorbed OH* species due to different numbers and strengths of hydrogen bonds. The discussion of hydrogen bonds is out of the main line of this thesis and will not be discussed here; details can be found in the published literature [179].

4.3.2 Configurations of surface OH*

There are top sites and bridge sites of Mo atoms on the (001) surface where the OH* can theoretically be adsorbed, while only adsorption on the top site was stable, forming a Mo–O bond with an average length of 1.98 Å in the direction perpendicular to the surface. During the optimisation of the DFT calculations, the OH* adsorbed on the bridge site was unstable and eventually transferred to the top site. Therefore, the calculations in this chapter only discuss OH* at the top sites.

At each coverage level, various configurations of OH* adsorption might have different stabilities. Thus, possible configurations in a total number of 76 were calculated as shown in supplementary information Figure S3. Only the most stable configurations are depicted in the figure below. In a similar way to the process during the dissociation of the water molecule, hydrogen bonds play an important role in stable configurations at different coverages. In the case of OH* at 2/9 ML coverage, the most stable configuration had a hydrogen bond with a length of 1.61 Å between two OH* species (Figure S3(b)(1)),

which shows the lower value of the average binding energy of 0.32 eV than that of the configuration without hydrogen bond (Figure S3(b)(3)). For the 1/3 ML coverage, there were two hydrogen bonds with the lengths of 1.64 and 1.62 Å, respectively in the most stable configuration (Figure S3(c)(1)), reducing the surface energy by 0.57 eV compared to weak interactions between OH* groups (Figure S3(c)(6)). Likewise, when the OH* coverage was 4/9 ML, the presence of two hydrogen bonds with lengths of 1.65 and 1.84 Å reduced the surface energy by 0.70 eV, as shown in Figure S3(d)(1) and (9). The strength and number of hydrogen bonds broken affect the H_2O* dissociation to different extents.

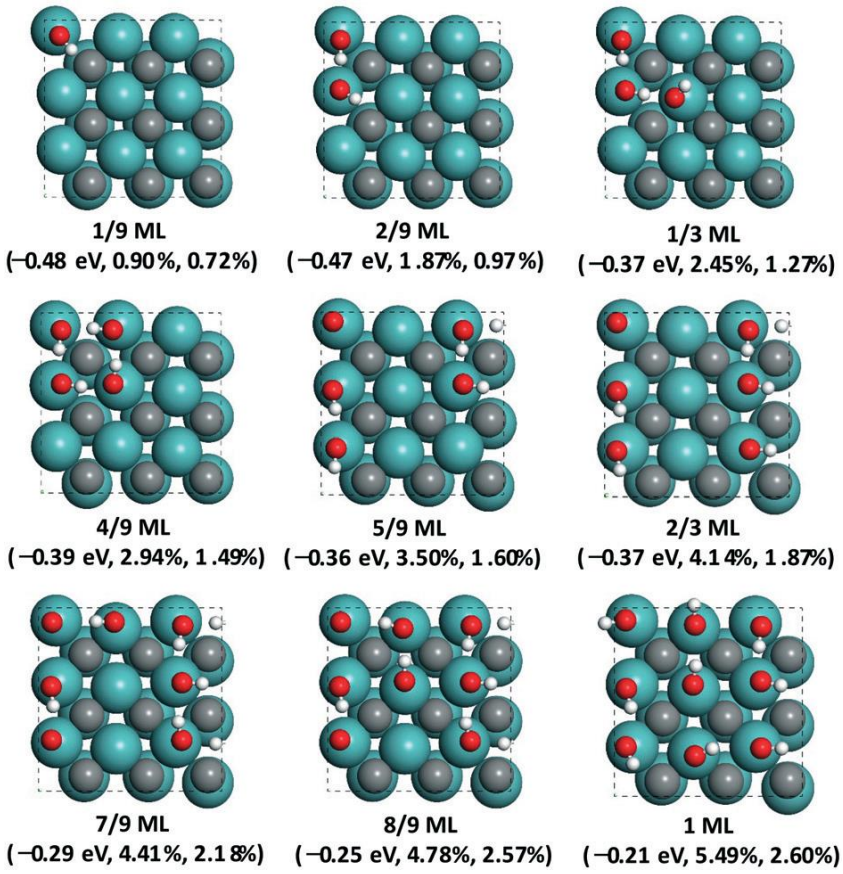

Figure 4.5 Configurations of OH* adsorbed on the fcc MoC (001) surface.

Figure 4.5 illustrates the configurations on the (001) surface adsorbed with different numbers of OH* species, with coverage ranging from 1/9 to 1 ML. From left to right, each subfigure shows the average binding energy of OH* and the surface oxidation degrees of Mo sites and C sites, respectively. The energy references were the gaseous H_2O and H_2.

The surface binding energy of OH* increased from −0.48 to −0.21 eV as the OH* coverage on the (001) surface increased. With a similar trend, that increased from −1.65 to −1.31 eV with increasing OH* coverage on the (111)-Mo surface [108], showing a relatively stronger binding strength than that on the (001) surface. The reactive top-site OH* on the (001) surface had an average surface binding energy of −0.48 eV at 1/9 ML, while at the same coverage, the reactive top-site OH* on the (111)-Mo surface had an average binding energy of −1.02 eV [108], showing stronger binding strength. Comparing the binding energies between H_2O* species (Figure 4.2) and OH* species (Figure 4.5), the H_2O* species showed a higher binding strength on the (001) surface at each coverage, whereas in contrast the OH* species showed a higher binding strength on the (111)–Mo surface [108]. As the OH* coverage increased, the oxidation degree of the sites on the MoC (001) surface gradually increased while similarly that of the (111)-Mo surface gradually increased [108].

4.3.3 Formation of surface O* *via* OH* dissociation

In the previous section, the configurations of OH* adsorbed on the (001) surface were

discussed, and the most stable configurations at each coverage were given, as shown in Figure 4.5. Based on the formed OH*, the formation of surface O* involves two pathways: direct deprotonation and hydroxyl disproportionation, as depicted in Figure 4.6.

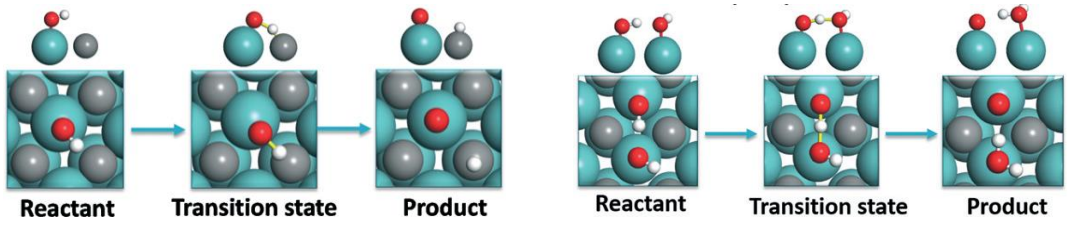

(a) direct deprotonation

$$n\,OH^* \longrightarrow (n-1)OH^* + H^* + O^*$$

(b) hydroxyl disproportionation

$$n\,OH^* \longrightarrow (n-2)OH^* + H_2O^* + O^*$$

Figure 4.6 Diagram of surface O* formation *via* (a) direct deprotonation and (b) hydroxyl disproportionation.

Table 4.1 and 4.2 illustrate the energy barriers and reaction energies for the two pathways, respectively. The detailed results of potential energy profiles and structures were shown in Figure S4 and Figure S5.

Table 4.1 The energy barrier and the reaction energy of the O* formation from surface OH* *via* the direct deprotonation.

n	$\Delta E^{\neq}_{\mathrm{TS,ZPE}}$	$\Delta E^{\neq}_{\mathrm{TS}}$	$\Delta E_{r,\mathrm{ZPE}}$	ΔE_r	$d^{\neq}_{\mathrm{O\cdots H}}$
1	0.72	0.85	0.01	0.03	1.334
2	1.00	1.13	0.44	0.46	1.365
3	1.36	1.52	0.65	0.68	1.344
4	1.34	1.50	0.63	0.67	1.342

n	$\Delta E^{\neq}_{\mathrm{TS,ZPE}}$	$\Delta E^{\neq}_{\mathrm{TS}}$	$\Delta E_{r,\mathrm{ZPE}}$	ΔE_r	$d^{\neq}_{\mathrm{O\cdots H}}$
5	1.43	1.58	0.78	0.83	1.330
6	1.84	2.00	1.23	1.28	1.431
7	1.62	1.77	0.89	0.92	1.400
8	1.54	1.67	0.74	0.75	1.380
9	1.52	1.65	0.98	1.00	1.330
Average	**1.37**	**1.52**	**0.71**	**0.74**	**1.362**

Note: $\Delta E^{\neq}_{\mathrm{TS,ZPE}}$ and $\Delta E_{r,\mathrm{ZPE}}$ are the energy barrier and the reaction energy with zero-point correction in units of eV while removing the subscript ZPE indicates the values without zero-point correction. The O–H bond length in the transition state is denoted by $d^{\neq}_{\mathrm{O\cdots H}}$ in the unit of Å.

In the direct deprotonation pathway, the main step is breaking the O–H bond in OH* and forming the C–H bond on a Mo–C pair site. The calculated results showed that the average angle of Mo–O–H decreased from 110° to 83°, indicating an apparent O–H bond bending towards the C site (Table 4.1 and Figure S4). The average length of the O–H bond was 1.00 Å in the initial state and increased to 1.36 Å in the transition state accompanied by a decrease in the distance between the H and C sites from 2.75 Å to 1.35 Å. Finally, the O* was generated on the top-site Mo site with an average distance between the O and Mo sites of 1.72 Å. The energy barriers were between 0.72 and 1.84 eV with an average of 1.37 eV, while the reaction energies ranged from 0.01 to 1.23 eV with an average of 0.71

eV. This high energy barrier and endothermicity revealed that the formation of O* *via* the direct deprotonation pathway on the (001) surface was unfavourable in both the kinetics and the thermodynamics. In contrast, the energy barrier was averaged at only 0.80 eV on the (111)-Mo surface, while the reaction energy was averaged at −0.90 eV [108].

Table 4.2 The energy barrier and the reaction energy of O* formation from surface OH* *via* the hydroxyl disproportionation.

n	$\Delta E_{\mathrm{TS,ZPE}}^{\neq}$	$\Delta E_{\mathrm{TS}}^{\neq}$	$\Delta E_{r,\mathrm{ZPE}}$	ΔE_r	$d_{\mathrm{O\cdots H}}^{\neq}$
2	0.00	0.02	−0.13	−0.18	1.135
3	0.00	0.06	−0.03	−0.06	1.185
4	0.00	0.04	−0.23	−0.24	1.153
5	0.00	0.05	−0.17	−0.20	1.164
6	0.03	0.13	−0.12	−0.13	1.196
7	0.00	0.03	−0.27	−0.29	1.130
8	0.00	0.01	−0.35	−0.40	1.105
9	0.00	0.04	0.04	−0.33	1.133
Average	**0.00**	**0.05**	**−0.16**	**−0.23**	**1.150**

In the hydroxyl disproportionation pathway, a proton is transferred between two neighbouring hydroxyl groups to form the top site O* and H_2O*. The results, as seen in Table 4.2 and Figure S5, showed that the formation of the O* was kinetically more favourable than that in the direct deprotonation pathway due to low energy barriers and

mild exothermicity with an average value of −0.23 eV. In the hydroxyl disproportionation, the transition state structure was only slightly changed compared to the reactants and the length of the O–H bond was only stretched by 0.15 Å, while this value was 0.36 Å in the direct deprotonation pathway, which can be seen as the cause of the low energy barriers. In addition, the presence of the hydrogen bonds in the hydroxyl disproportionation pathway could promote the proton transfer between the neighbouring OH* species, but this would hinder the deprotonation of OH* directly to some extent. A similar phenomenon can also be found in reference [187] that the hydrogen bonds played analogous role in the formation of the O* *via* disproportionation on the (101) surface of hexagonal Mo_2C.

In addition, based on this discussion, it can be learnt that the disproportionation pathway is the main source of O* obtained on the MoC (001) surface.

4.3.4 Configurations of surface O*

As mentioned in the previous section and in Tables 4.1 and 4.2, the primitively generated O* usually occupied the top site of the Mo atom. Here, additional studies of the structural evolution of the generated surface O* species was required by using the AIMD method. The evolution of the O* species at the coverage of 1/9 ML with time up to 3700 fs at 473.15 K was calculated as shown in Figure 4.7 while the initial configuration was a top-site O* configuration with the Mo–O bond directly normal to the (001) surface.

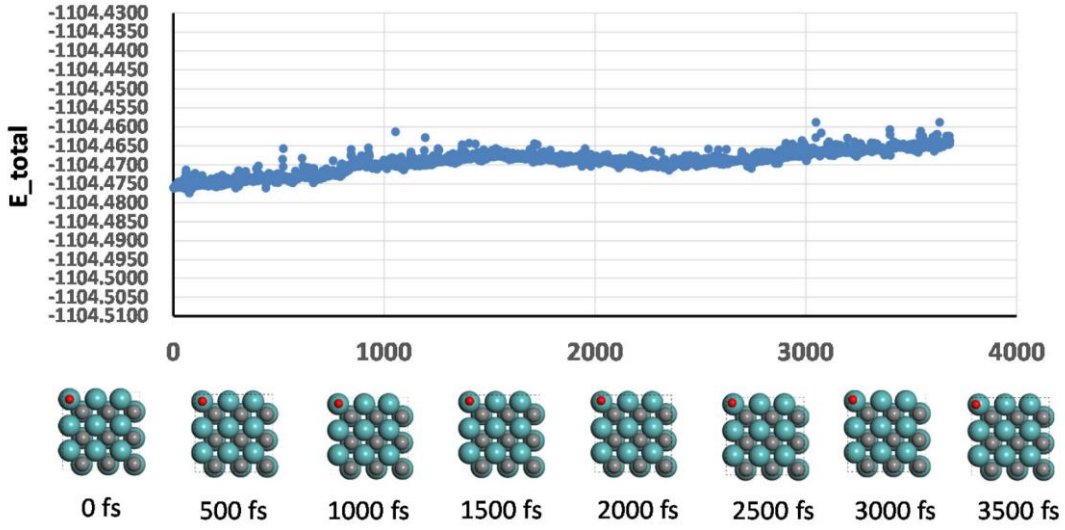

Figure 4.7 Structural evolution of top-site O* on the (001) surface at the coverage of 1/9 ML and temperature of 473.15 K.

The results showed that, except for a few small fluctuations, the O* remained at the top site after a calculation of 3700 fs, which implies a stable configuration for the top site Mo.

The most stable configurations at each coverage level of the adsorbed O* species on the (001) surface were shown in Figure 4.8. The average binding energy of O* (eV), the degree of oxidation of the Mo sites and the C sites are shown below each sub-figure. The gaseous H_2O and H_2 were used as reference.

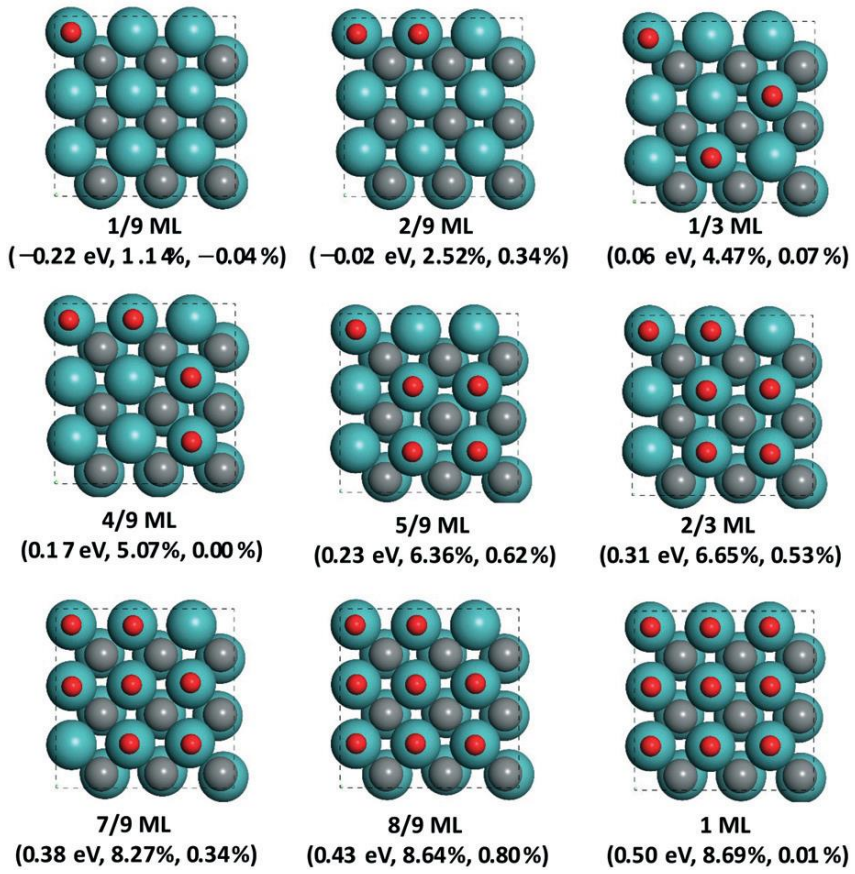

Figure 4.8 Configurations of O* species adsorbed on the fcc MoC (001) surface.

An increasing trend in the average binding energy with increasing O* coverage. When the coverage of the O* species exceeded 2/9 ML, the average binding energy values became positive, indicating a weak surface binding strength of O* and the thermodynamically unfavourable formation of O*.

To give a brief summary of the O-containing species (H_2O*, OH*, O*), the order of the surface binding strength on the (001) surface was H_2O* (−0.76 eV) > OH* (−0.35 eV) > O* (0.20 eV), while that on the(111)-Mo surface was O* (−1.58 eV) > OH* (−1.50 eV) > H_2O* (−0.94 eV) [108], where in brackets are the surface binding energies averaged over

the coverages. Overall, the (001) surface exhibited significantly weaker surface binding strength with respect to O-containing species than the (111)-Mo surface.

4.3.5 Formation of surface H* species *via* H_2* dissociation

The generated H* species would bond with a Mo site or a C site on the (001) surface in the form of Mo–H* or C–H*. It should be noted that the (001) surface has the potential for further generation of CH*x* species, but this is beyond the scope of this thesis. In this work, it was considered the assumption that the H* species originate only from C–H* species and Mo–H* species, which was based on the study of the hydrogenation reaction on the fcc MoC (001) surface carried out by Jimenez-Orozco *et al.* [114]. Their studies also revealed that the H* coverage could strongly influence the reaction. Prats *et al.* [190] investigated the H_2* dissociation on the (001) surface of fcc MoC but did not consider the coverage effects. On the other hand, due to the presence of a reforming atmosphere (H_2/H_2O), the catalytic surface inevitably needs to take into account the already present H_2* species.

As depicted in Figure 4.9, the dissociation of H_2* species on the (001) surface involved two elementary reaction steps. The breaking of the H–H bond in H_2* to form the Mo–H* and C–H* species occurred in the first step (R1→TS1→P1), followed by the formation of another C–H* species by migration of the H* in the Mo–H* species to a bare nearby C site (P1→TS2→P2).

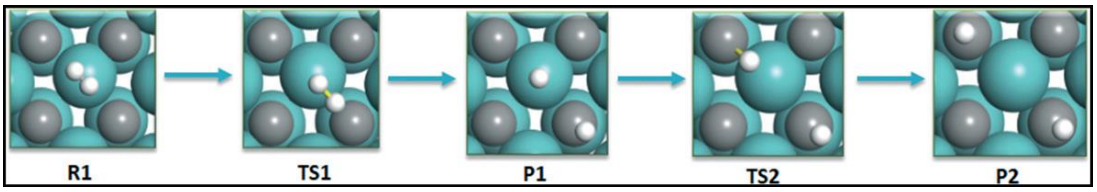

Figure 4.9 Elementary reaction steps in H_2* dissociation

For different H_2* coverages, this process can be concluded by the following formula to form $C–H^*$ species:

$$n\,H_2^* \xrightarrow{\text{Step 1}} (n-1)\,H_2^* + Mo–H^* + C–H^* \xrightarrow{\text{Step 2}} 2\,C–H^* \quad \text{with} \quad n = 1–9\,.$$

And for different H* coverage, the first step can be written as the following formula:

$$n\,C–H^* + H_2^* \rightarrow (n+1)\,C–H^* + Mo–H^* \quad \text{with} \quad n = 1–8\,.$$

For each elementary reaction step above, Table 4.3 shows the energetic aspects of surface H* formation by H_2* dissociation at different H_2* and H* coverages. In this table, the energy barriers for steps 1 and 2 with ZPE correction are denoted as $\Delta E^{\neq}_{\mathrm{TS1,ZPE}}$ and $\Delta E^{\neq}_{\mathrm{TS2,ZPE}}$, respectively while the reaction energies for steps 1 and 2 with ZPE correction are denoted as $\Delta E_{r1,\mathrm{ZPE}}$ and $\Delta E_{r2,\mathrm{ZPE}}$, respectively with the unit of eV. The reference states for steps 1 and 2 are the H_2 adsorption state and the intermediate products (Mo–H* +C–H*) respectively. The dissociating H–H bond length in H_2* dissociation is given in Å denoted as $d^{\neq}_{\mathrm{H\cdots H}}$.

Table 4.3 The energy barrier and the reaction energy of H* formation through H_2* dissociation at various H_2* and H* coverage.

n	At different H_2* coverages					At different H* coverages		
H_2*/H*	$\Delta E^{\neq}_{\mathrm{TS1,\,ZPE}}$	$\Delta E_{r1,\,\mathrm{ZPE}}$	$d^{\neq}_{\mathrm{H\cdots H}}$	$\Delta E^{\neq}_{\mathrm{TS2,\,ZPE}}$	$\Delta E_{r2,\,\mathrm{ZPE}}$	$\Delta E^{\neq}_{\mathrm{TS1,\,ZPE}}$	$\Delta E_{r1,\,\mathrm{ZPE}}$	$d^{\neq}_{\mathrm{H\cdots H}}$
1	0.22	−0.10	1.066	0.31	−0.78	0.27	−0.12	1.040
2	0.43	0.11	1.065	0.31	−0.79	0.53	0.22	1.139
3	0.56	0.011	1.132	0.18	−0.75	0.78	0.30	1.139
4	0.54	0.00	1.120	0.18	−0.83	0.67	0.24	1.157
5	0.49	−0.04	1.053	0.20	−0.72	0.68	0.38	1.188
6	0.47	−0.06	1.055	0.20	−0.72	0.97	0.54	1.081
7	0.50	−0.01	1.031	0.34	−0.70	0.56	0.20	1.109
8	0.47	−0.09	1.053	0.22	−0.67	0.62	0.27	1.119
9	0.48	−0.06	1.053	0.21	−0.68	—	—	—
Average	**0.46**	**−0.03**	**1.070**	**0.24**	**−0.74**	**0.64**	**0.25**	**1.122**

As shown in Table 4.3, in the first step of H_2* dissociation, as the H_2* coverage increased from 1/9 to 1/3 ML, the energy barriers increased from 0.22 to 0.56 eV, and then fluctuated and became stable as the H_2* coverage increased further. This is supported by calculations by Prats *et al.* [190], who calculated an energy barrier of 0.39 at 1/8 ML coverage, a value between the present work at 1/9 ML coverage of 0.22 eV and 2/9 ML coverage of 0.43 eV. The dissociation of H_2* species to the Mo–H* and C–H* species was almost in equilibrium as the reaction energies were close to zero with an average value of −0.03 eV. Then, the generated Mo–H* species was easily transformed into a C–H* species because the average energy barrier was only 0.24 eV and exothermic with an average reaction energy of −0.74 eV. As demonstrated in Figure S6, on the (001) surface, the generated H* species preferentially occupied the C sites and then the Mo sites. For the effect of the H_2* dissociation with adsorbed H*, the average energy barrier was increased by 0.18 eV and the average reaction energy was increased by 0.28 eV.

4.4 Results and discussion of surface phase structure evolution

4.4.1 Kinetic aspects

As found in previous sections, the formation and configuration of the surface phase on the (001) surface were different from those on the (111)-Mo surface [96]. Here, the evolution of surface species on the (001) surface was investigated. The results are shown in Table 4.4, calculating the reaction rate constants (k) for surface species at different coverages (θ) from 1/9 to 1.

Table 4.4 The reaction rate constants of elementary reactions at 473.15 K.

		Surface OH* formation		Surface O* formation			Surface H* formation	
n	θ	n H_2O*	n OH*	n OH* deprotonation	n OH* disproportionation		n H_2*	n H*
					$k_{forward}$	$k_{reverse}$		
1	1/9	6.4×10^{9}	2.3×10^{8}	6.0×10^{4}	—	—	1.8×10^{10}	4.7×10^{9}
2	2/9	4.5×10^{8}	5.6×10^{6}	1.0×10^{2}	5.3×10^{12}	4.7×10^{11}	3.4×10^{7}	3.6×10^{5}
3	1/3	6.4×10^{8}	1.0×10^{5}	4.0×10^{-2}	6.2×10^{12}	3.6×10^{12}	1.4×10^{6}	6.0×10^{2}
4	4/9	7.3×10^{7}	5.7×10^{3}	5.2×10^{-2}	7.0×10^{12}	4.1×10^{10}	3.5×10^{6}	3.6×10^{3}
5	5/9	1.5×10^{8}	1.4×10^{1}	1.1×10^{-2}	8.4×10^{12}	1.3×10^{11}	9.9×10^{6}	6.4×10^{3}
6	2/3	1.6×10^{7}	3.1×10^{-5}	2.1×10^{-7}	2.3×10^{12}	9.5×10^{10}	7.4×10^{7}	3.5×10^{0}
7	7/9	2.2×10^{8}	2.3×10^{-6}	2.5×10^{-5}	6.3×10^{12}	1.9×10^{10}	1.8×10^{7}	1.1×10^{5}
8	8/9	1.2×10^{7}	7.6×10^{-3}	2.5×10^{-4}	8.4×10^{12}	3.9×10^{9}	5.5×10^{7}	1.9×10^{4}
9	1	8.7×10^{6}	—	1.1×10^{-3}	3.0×10^{12}	7.1×10^{9}	6.5×10^{7}	—

In the calculation of the vibrational partition functions, frequencies below 50 cm^{-1} were shifted to 50 cm^{-1} to eliminate errors associated with low frequency modes. The reaction pathway with the lowest energy barrier was selected for each coverage.

The OH* formation rate constants *via* H_2O* dissociation on (001) surface were in the order of 10^6 to 10^9 s^{-1}, but those with co-adsorbed OH* showed a drastic decrease from 10^8 to 10^{-6} s^{-1}. In contrast, as reported in the literature [108], the reaction rate constants for OH* formation on the (111)-Mo surface were in the order of 10^9 to 10^{12} s^{-1}, exhibiting higher reaction rates.

The surface O* can be generated from the formed OH* species by either deprotonation or disproportionation, as discussed previously in Section 4.3.3. From the data in Table 4.4, the disproportionation reaction calculated significantly higher reaction rate constants than the direct deprotonation reaction, and even 3 to 6 orders of magnitude faster than the OH* formation *via* H_2O* dissociation. Notwithstanding this, the reverse disproportionation reaction (H_2O*+O*→2OH*) also had high reaction rate constants that are 1 to 3 orders of magnitude lower than those of the forward reaction and are 1 to 3 orders of magnitude higher than those of OH* formation *via* H_2O* dissociation. It means that once H_2O* is converted to OH* species and then quickly disproportionated to O* species, at the same time, the surface O* species can be reduced into OH* by the reverse disproportionation at comparable reaction rates. The reverse disproportionation reaction in this work had an average energy barrier of 0.17 eV, which was comparable to the reported energy barrier

on the hexagonal Mo_2C (101) surface at 0.15 eV [187].

The molecular H_2 and molecular H_2O would compete for the same Mo–C pair site on the (001) surface, influencing the catalytic performance. Therefore, it is important to compare the relative stability of the dissociated H* and the generated O-containing species. It can be seen from Table 4.4 that the rate constants of the H* formation at different H_2* coverages were of comparable magnitude to those of the OH* formation at different H_2O* coverages, indicating that it was easy to form the H* species. Although the reaction rate constants obviously decreased when the surface was covered with the H* species, their orders of magnitude were still not negligible (higher than 10^3).

From a kinetic point of view, the species, including OH*, O*, and H*, were all readily formed on the (001) surface and were present in large quantities. Besides this kinetic consideration, the relative stabilities governed by thermodynamics would also influence the composition of the species that existed on the (001) surface under the H_2O/H_2 atmosphere. On the one hand, this composition would affect the reaction properties. For example, it has been found by Jimenez-Orozco *et al.* [114] that the (001) surface of MoC with higher H* coverage facilitated the hydrogenation of ethylene, while we can naturally conclude that this surface is unfavourable for the water-gas shift reaction. The reaction mechanism could be influenced by the surface species, which is determined by the relative stabilities of these species. Therefore, it is important next to discuss the thermodynamic aspects of surface phase evolution.

4.4.2 Thermodynamic aspects

The (001) surface of fcc MoC readily forms OH*, O* and H* species under the H_2O/H_2 atmosphere, with OH* and O being favourable for the water-gas shift reaction. *Ab initio* thermodynamics were implemented to obtain the relative stabilities of possible species formed on the (001) surface under the H_2O/H_2 atmosphere, which were displayed in the surface phase diagram.

For the construction of the phase diagram, the most stable configurations of H_2O*, OH*, O* and H* discussed earlier and the most stable surface mixed species, *e.g.* [H_2O*+OH*], [H_2O*+OH*+O*], [H_2O*+OH*+H*], were all considered. Referring to the experimental data in studies [47, 48, 66-68, 191], a pressure of H_2 ranging from 10^{-10} to 10 MPa and a pressure of H_2O ranging from 10^{-3} to 10 MPa at a temperature of 473.15 K were used in this computational study. The saturation vapour pressure of water is 1.55 MPa at a reaction temperature of 473.15 K and the vapour will condense to the liquid water if the pressure is increased further.

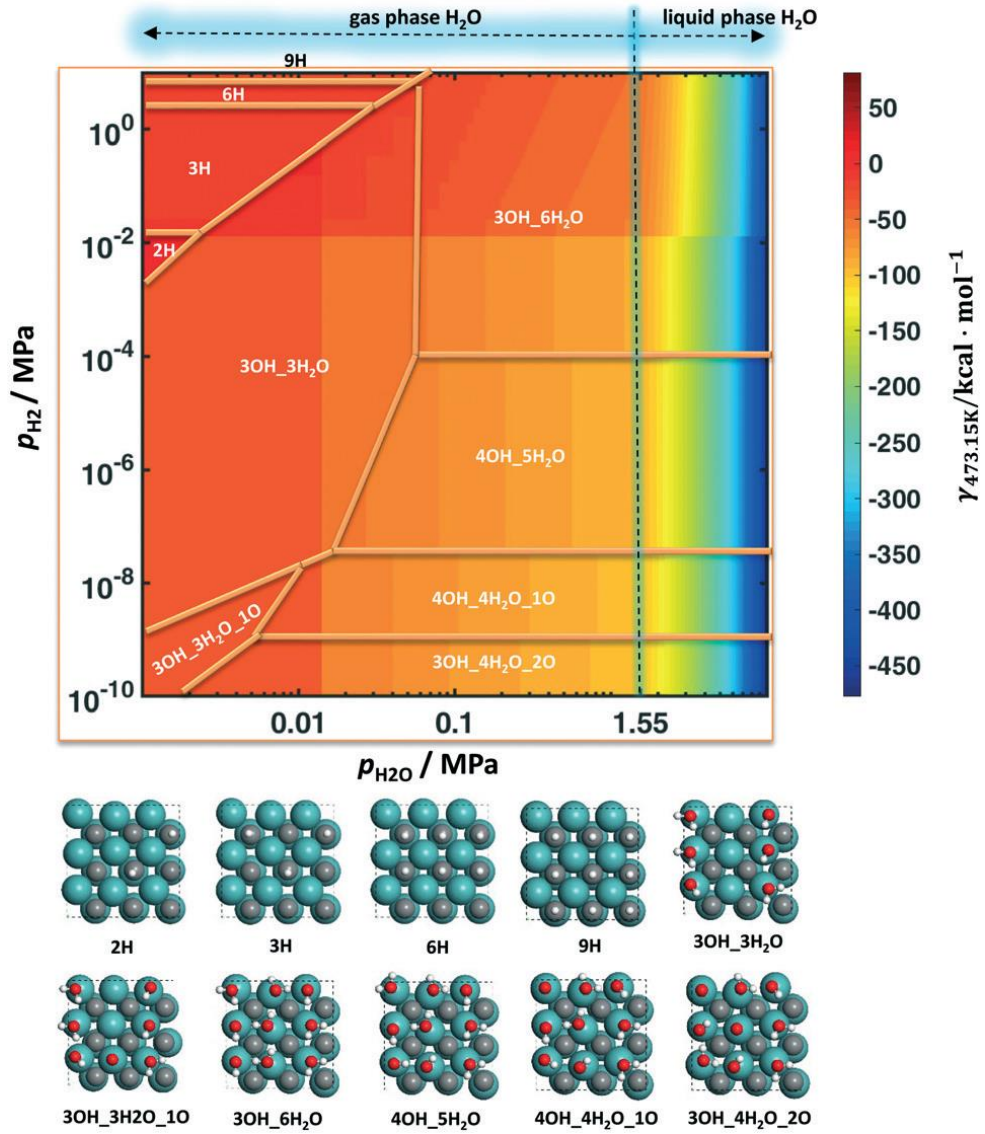

Figure 4.10 The fcc MoC (001) surface phase diagram at 473.15 K.

The constructed surface phase diagram has been summarised in Figure 4.10, which shows the stabilities of the surface species on the (001) surface in a H_2O/H_2 environment, with the configurations of the different phase structures at the bottom. As there were nine sites on the (001) surface where the mixture of surface species could be adsorbed, the expression '4OH_4H_2O_1O' denotes 4 OH*, 4 H_2O*, and 1 O* on the (001) surface, the same below.

The (001) surface species were mainly the O-containing species, a mixture of H_2O*, OH* and O* species. When the H_2 pressure was less than 3×10^{-8} MPa, the constitution of the surface phase was mainly of 4OH_4H_2O_1O, 3OH_3H_2O_1O and 3OH_4H_2O_2O. It indicates that the surface phase structure at the start of the water-gas shift reaction, has both OH* and O* species existing on the surface. With the increase in hydrogen pressure, the surface OH* composition increased as the decrease in the surface O* composition (3OH_4H_2O_2O → 4OH_4H_2O_1O). It also means that as the hydrogen production reaction proceeds, the surface is gradually covered with more OH* species. When the hydrogen pressure exceeded 10^{-7} MPa, the surface O* species disappeared completely (4OH_4H_2O_1O → 4OH_5H_2O), while it can be inferred that the O* species were first reduced to the OH* species and then the OH* formed the H_2O*. A further increase in H_2 pressure would convert the surface OH* species to surface H_2O* (4OH_5H_2O → 3OH_6H_2O). Keeping the H_2 pressure constant and reducing the H_2O pressure could result in a decrease in O-containing species. For example, with fixed H_2 pressure close to 10^{-5} MPa, the (001) surface phase structure would be converted from 4OH_5H_2O to 3OH_3H_2O by decreasing H_2O pressure from 10 to 10^{-3} MPa. The surface started to present H* species when the H_2O pressure was close to 10^{-3} MPa and the H_2 pressure was above 10^{-3} MPa, and the further increase in H_2 pressure would lead to an increase in the coverage of the H* species.

In view of the above, the formation of the OH* or O* species was easier than that of the H* species on the (001) surface, signifying the important catalytic role of the (001)

surface. The Sabatier principle states that the binding strength between the catalyst surface and the intermediates should be neither too strong nor too weak [102-105]. The order of the surface binding strengths of OH* and O* species at 1/9 ML coverage on fcc MoC can be obtained by combining the results in this chapter for the (001) surface with those in the literature [108] for the (111)-Mo surface, as follows: O* on (111)-Mo (−1.78 eV) > OH* on (111)-Mo (cavity site, −1.65 eV) > OH* on (111)-Mo (bridge site, −1.40 eV) > OH* on (111)-Mo (top site, −1.02 eV) > OH* on (001) (−0.48 eV) > O* on (001) (−0.22 eV). The OH* and O* species on the (001) surface showed relatively lower binding strengths, suggesting that the (001) surface may have qualitatively better reactivity. However, the specific reaction pathways in water-gas shift reactions are still not negligible, and this will be further clarified and compared in later chapters.

4.5 Summary

This chapter systematically calculated the surface phase structure evolution on the (001) surface of fcc MoC in an H_2O/H_2 environment. Based on the DFT method, we first carried out the investigation of the dissociation of H_2O*, OH* with different coverages and the configuration of the dissociated OH*, O* to study the most stable configurations of the species. During the study of the O* configuration, the *ab initio* molecular dynamics method was additionally implemented for confirmation purposes. Following these analyses, the surface phase structure evolution in kinetic aspects was performed to investigate the possible species on the (001) surface. Finally, the *ab initio* thermodynamics was used to obtain the phase diagram at 473.15 K to consider the relative

stabilities of these species in the thermodynamic aspects.

It was found that the species including OH*, O*, and H* were all readily formed on the (001) surface according to the reaction rate constants, but the comprehensive investigation showed that the H_2O*, OH*, and O* species tended to cover the (001) surface instead of H*, justifying the importance of the evolved surface in the water-gas shift reaction.

Chapter 5 Results and Discussion (II): WGS on original surface of Pt_1/fcc MoC

In the previous chapter, a detailed study of the (001) surface demonstrated results that were quite different from those in the literature for the (111)-Mo surface [108]. While the (111)-Mo surface is prone to be covered by an O* layer or OH* layer, the evolution of the (001) surface could lead to a surface phase mixed with H_2O, OH and O* species. There are controversies on which surface plays the dominant role in water-gas shift reaction and which kind of mechanism is preferred by different surfaces. In this chapter, different routes (the associative route, the redox route, and the water-assisted associative route) for the WGS on original Pt_1 doped fcc MoC catalysts were presented, considering the difference between (111) and (001) facets. Then, the energetic span model evaluated and compared the TOF of different catalytic cycles on different facets.

5.1 Model setup

5.1.1 Pt doped fcc MoC (111)-Mo surface

The clean and Pt doped (111)-Mo surface of fcc MoC was represented by a periodic *p*(3×3) supercell slab model as the side and top views in Figure 5.1 (a) and (b). The five layers of Mo atoms and five layers of C atoms were alternatively stacked, with each layer consisting of 9 atoms in a 3×3 arrangement with a total thickness of 11.3 Å. The vacuum gap between the adjacent periodic slabs in the direction perpendicular to the surface was set to 15 Å for the (111)-Mo models to avoid artificial interactions between the periodic

slabs. The top six layers of the Pt_1/(111)-Mo slab model (including Pt) were relaxed in structure optimisation with the bottom four layers fixed. A 4×4×1 Γ-centred Monkhorst-Pack [150] mesh grid was used for the first Brillouin zone *k*-point sampling for this slab model.

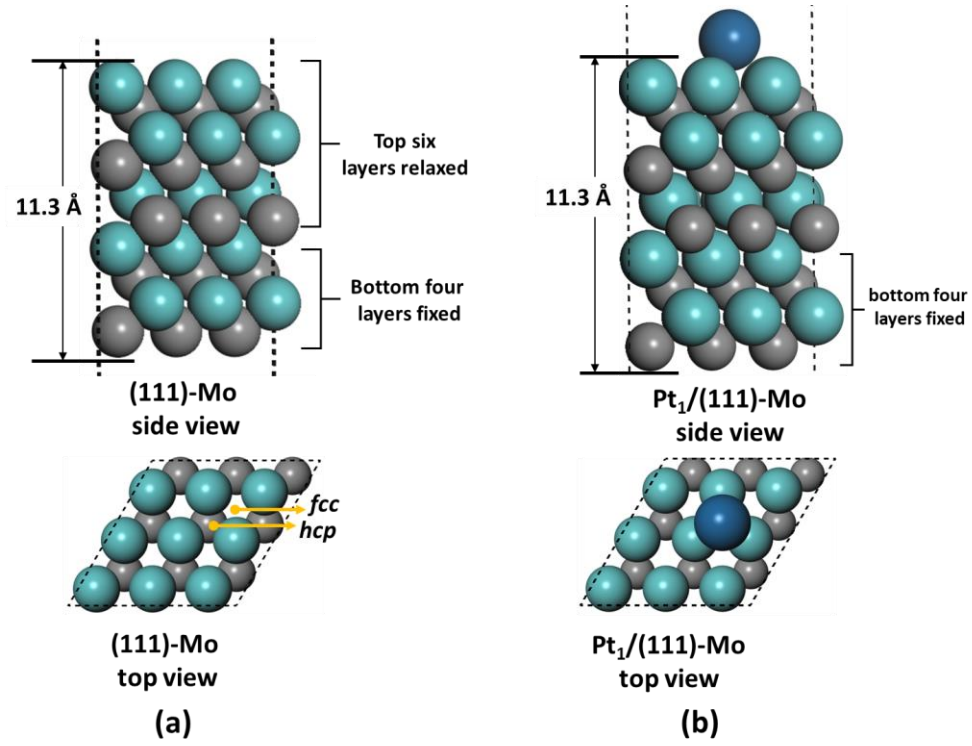

Figure 5.1 Surface slab models of (a) clean fcc MoC (111)-Mo surface and (b) Pt-doped (111)-Mo surface (Green balls: Mo; grey balls: C; blue balls: Pt; only the two topmost layers were presented in top view for clarity).

The lattice parameter was validated as structure as the calculated value was 4.34 Å in this work, and the experiment value was 4.27 Å in reference [192]. The distance between adjacent Mo atoms was also validated as the calculated value in this work was 3.07 Å while the calculation result from Lin *et al.* was 3.06 Å [48]. It can be seen from the top

view in Figure 5.1 (a) that there are two sites for Pt doping, namely, the hcp site (hexagonal closed-pack) and the fcc site (face-centred cubic). The calculation showed that the Pt anchored on the hcp site has a 0.2 eV higher stability than that on the fcc site, and the energy barrier of Pt migration from the hcp site to the fcc site was 0.32 eV. Thus, the Pt_1/(111)-Mo slab model was constructed with Pt anchoring on the hcp site, which was also supported by the results of Li *et al.* [193].

5.1.2 Pt doped fcc MoC (001) surface

The clean and Pt-doped (001) surface was represented by a periodic *p*(3×3) supercell slab model as the side and top views in Figure 5.2 (a) and (b). The (001) surface slab model possessed six layers with a total thickness of 10.9 Å, where each layer was constituted by a mixture of 9 Mo and 9 C atoms. Three topmost layers of the Pt_1/(001) slab model (including Pt) were relaxed in structure optimisation with the bottom three layers fixed. The vacuum gaps between the adjacent periodic slabs in the direction perpendicular to the surface were both set to 15 Å for the (001) model to avoid artificial interactions between the periodic slabs. A 4×4×1 Γ-centred Monkhorst-Pack [150] mesh grid was used for the first Brillouin zone *k*-point sampling for this slab model.

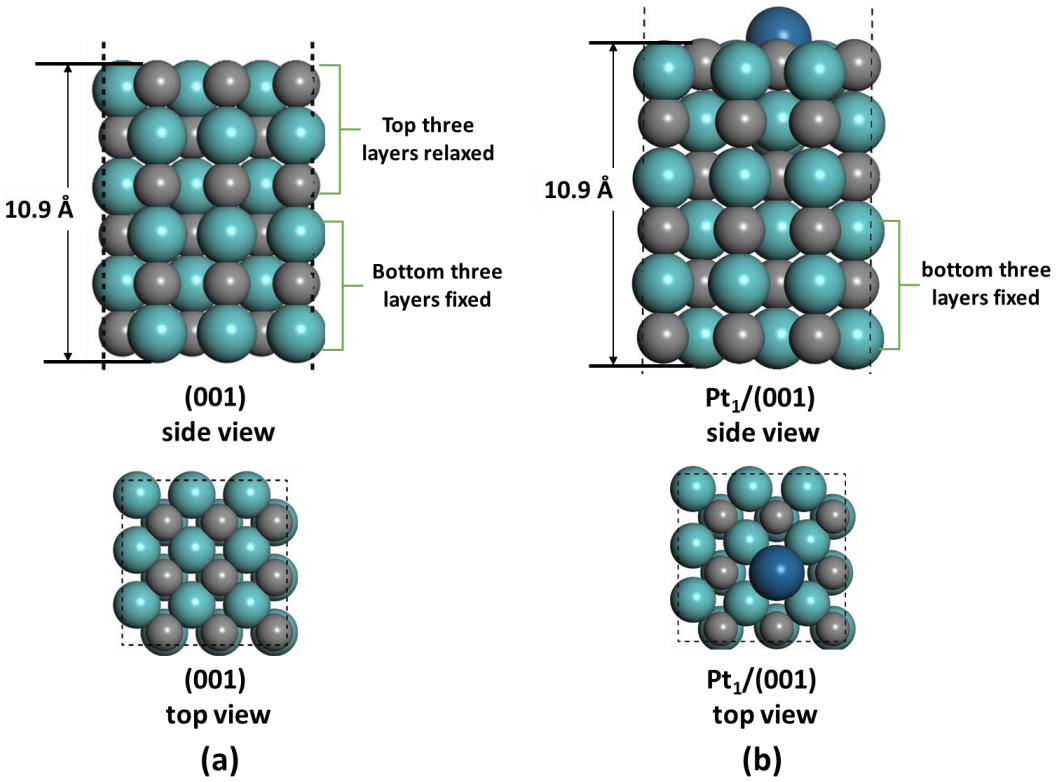

Figure 5.2 Surface slab models of (a) clean fcc MoC (001) surface and (b) Pt-doped (001) surface (Green balls: Mo; grey balls: C; blue balls: Pt; only the two topmost layers were presented in top view for clarity).

Similar to the (111)-Mo surface, the lattice parameter and the distance between adjacent Mo atoms were validated with the reference [48, 192]. The Pt atom directly replaced one surface C atom resulting in the Pt coordinating to 4 nearest Mo atoms at a distance of 2.7 Å, the model of which was in accord with that used by Wang *et al.* [113] and energetically more favourable than the Pt replacing one surface Mo atom or adsorbing on the (001) surface.

5.1.3 Simulation conditions

Detailed studies of WGS reactions performed on Pt_1/fcc MoC used a gas phase composition that has been experimentally reported. Unless noted otherwise, all Gibbs free energy changes of the catalytic cycles are calculated at 423.15 K and 1 atm pressure with full reformate gas phase composition (26% H_2O, 11% CO, 26% H_2, 7% CO_2 and 30% N_2) [47, 66].

5.2 Results of the original Pt_1/(111)-Mo surface

5.2.1 The associative route

In the associative mechanism, the CO first reacts with one OH group of adsorbed H_2O to form a surface carboxyl intermediate (HO–CO*), and then the further dehydrogenation of HO–CO* species leads to CO_2 and H_2. The free energy profile of this route has been calculated and is shown in Figure 5.3.

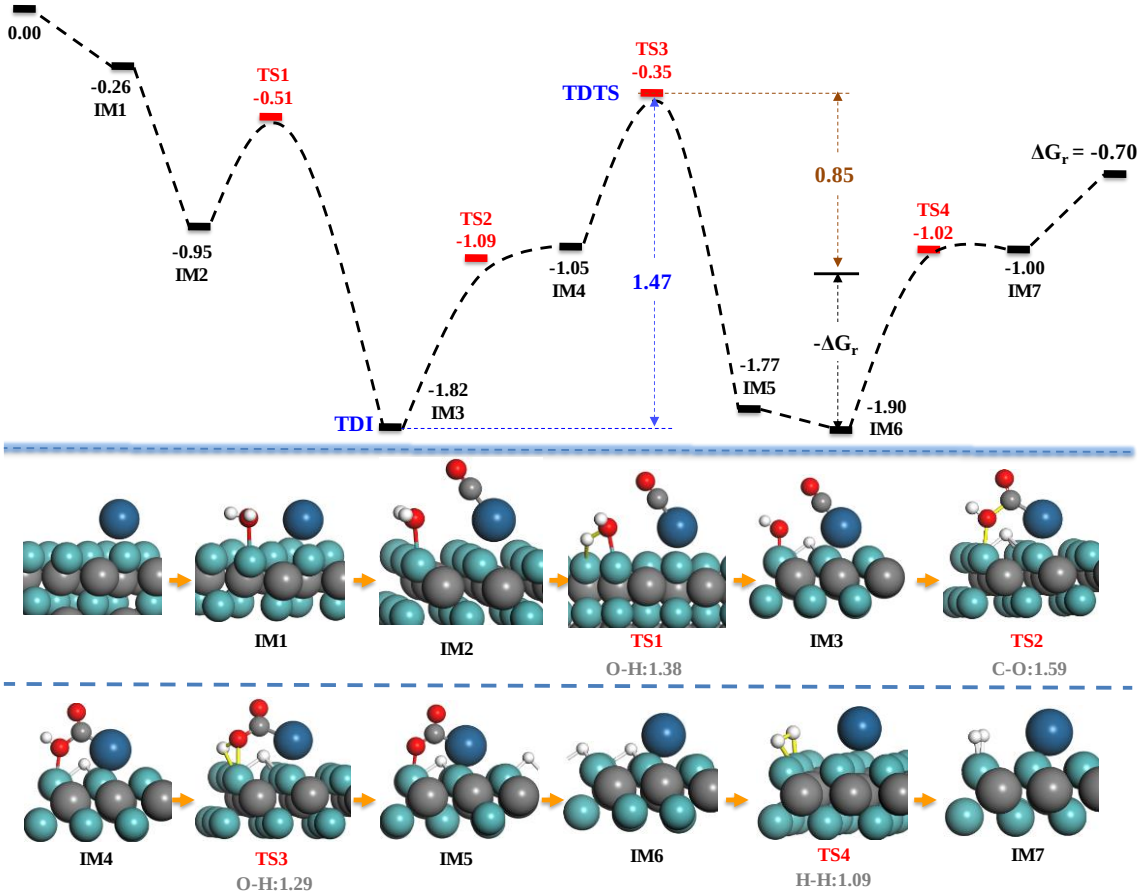

Figure 5.3 Free energy profile for the associative route on the original Pt_1/(111)-Mo surface.

The activation of the O–H bond in H_2O leading to the surface OH* group (IM2 → TS1 → IM3) is a necessary step in the associative route. The energy barrier for O–H cleavage of H_2O was 0.44 eV with an O···H distance of 1.38 Å, showing an excellent ability of H_2O activation. The reaction energy of −0.87 eV was fairly exothermic, indicating strong hydrophilicity of the fresh (111)-Mo terminated surface. It should be noted that the OH* generated by H_2O activation was the top-site type (IM3), where the OH* resided on top of a Mo site forming one Mo–O bond. As shown in ref. [108], the configuration of the top-site OH* made its O atom highly exposed and reachable by other molecules such as

CO. In the second step, CO combines with the top site OH* to form a HO–CO* intermediate (IM3 → TS2 → IM4) with an energy barrier of 0.73 eV. The C–(OH) bond length of the resulting HO–CO* intermediate (IM4) is only ~0.05 Å shorter than that of the transition state (TS2). Meanwhile, the energy barrier of the C–(OH) bond cleavage was negligibly small (0.04 eV), showing that the formed HO–CO* intermediate could readily dissociate back to CO and OH*. Otherwise, the highly unstable intermediate HO–CO* may also have the chance of dehydrogenation to CO_2 *via* O–H bond cleavage (TS3), whereas its reaction rate was about 10^7 times slower than that of the C–(OH) bond cleavage leading to CO and OH*. The final step was the binding of two chemisorbed H* atoms (IM6), leading to H_2 (IM7), which was kinetically and thermodynamically unfavoured. In contrast, the H–H bond cleavage of H_2 leading to surface chemisorbed H* overcame only a small barrier (0.02 eV) and released significant energy (0.90 eV), signifying a strong H-affinity of the fresh (111)-Mo terminated surface.

Among the many intermediate states of the free energy profile, the energy positions of IM3 (H/OH/CO co-adsorption) and IM6 (H adsorption) were rather too low, indicating that the (111)-Mo terminated surface had a too strong binding strength towards H, OH and CO species. The degree of TOF control (X_{TOF}) of IM3 was ~1.00, with those of other intermediates negligible, while the HO–CO* dehydrogenation (TS3) had the largest X_{TOF} of ~1.00. Thus, IM3 was identified as the TOF-determining intermediate (TDI) and the TS3 was identified as the TOF-determining transition state (TDTS). The energetic span (δE) determined by TS3 and IM3 formed the largest 'energy barrier' in the direction

of the forward reaction (equations (3-35) and (3-36)). The energy difference between the transition state of highest energy (TS3) and the intermediate of lowest energy (IM6) was 1.55 eV, whereas the effective 'energy barrier' was significantly reduced to 0.85 eV due to the compensation by the reaction energy (ΔG_r) shown in Figure 5.3 and equation (3-36).

5.2.2 The redox route

In the redox mechanism, the CO is oxidised directly by surface O* species to form CO_2 generated through the dehydrogenation of H_2O on the substrate. The free energy profile of this route has been calculated and is shown in Figure 5.4.

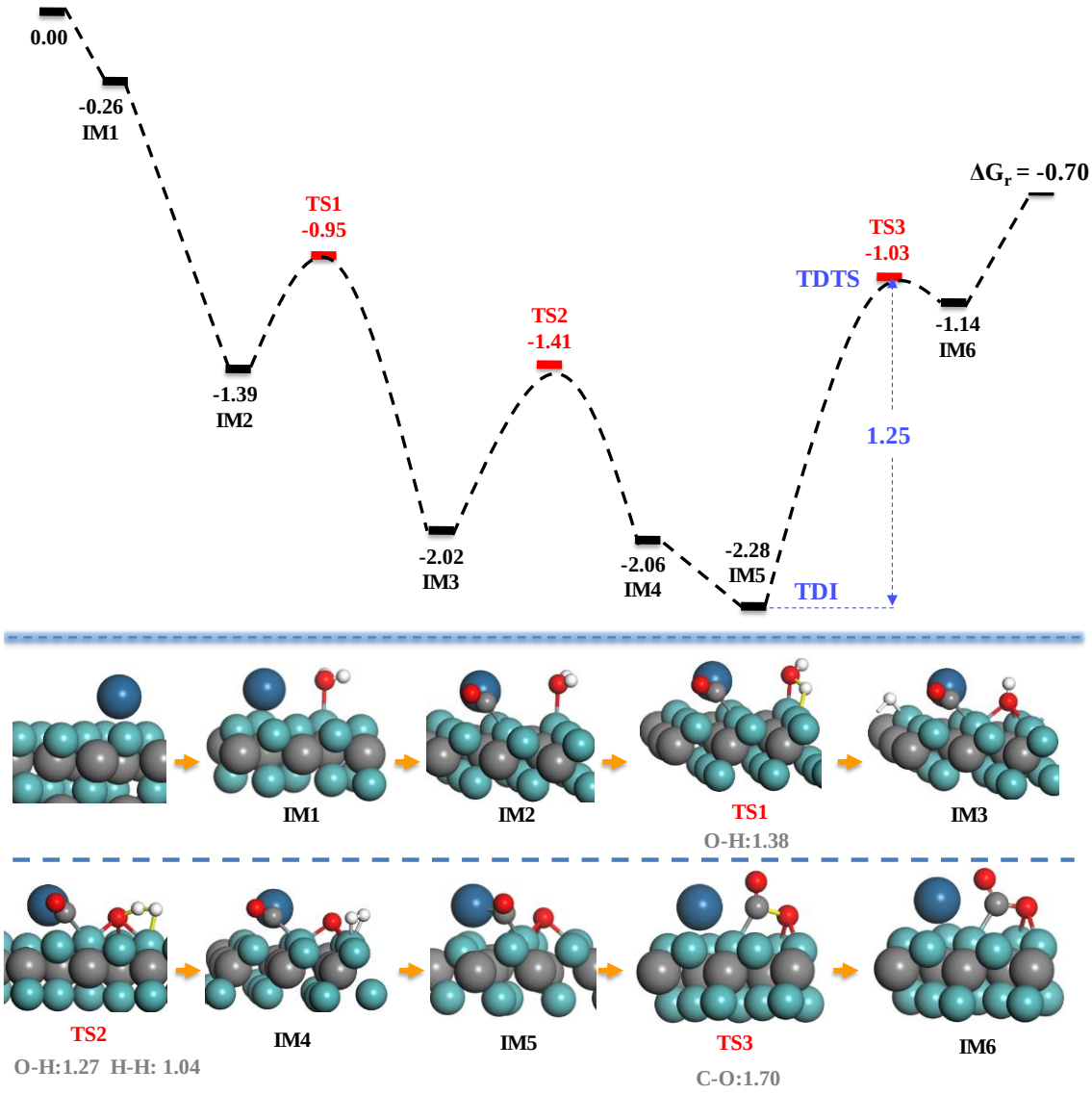

Figure 5.4 Free energy profile for the redox route on the original Pt_1/(111)-Mo surface.

The formation of surface O* species by complete H_2O dehydrogenation was an important step. The activation of the first O–H bond in H_2O was kinetically and thermodynamically favourable with an energy barrier of 0.44 eV (IM2 → TS1) and a reaction energy of −0.63 eV (IM2 → IM3). The generated OH* was a cavity-site type (adsorbing at the *hcp* or *fcc* site), where the O atom of OH* is bonded to three surface Mo atoms of triangular

arrangement. According to the research by literature [108], the cavity-site OH* with a T_d-like symmetry was more prone to dehydrogenate rather than react with other molecules due to its large steric hindrance around the O atom. The dehydrogenation of OH* to form surface O* was accompanied by a H–H bond formation (TS2), where the surface H* resulted from H_2O activation bonded with the H atom of OH* to produce one H_2 molecule and one surface O* (IM4). The H-assisted OH* dehydrogenation crossed an energy barrier of 0.61 eV (TS2) and was nearly thermodynamically neutral. The final step was the oxidation of adsorbed CO by surface O* to produce CO_2 (IM5 → TS3 → IM6). The CO adsorbed at the Pt–Mo interface with its C atom bonding to the Pt and Mo sites (IM5). The distance of Pt···C increased from 2.07 Å in IM5 to 2.87 Å in TS3, whereas C···O distance decreased from 3.25 Å in IM5 to 1.70 Å in TS3, and finally to 1.37 Å in the CO_2 molecule. The energy barrier of the CO oxidation step was 1.25 eV, whereas its reverse reaction, *i.e.,* dissociation of CO_2 to form CO and O*, could readily occur with a small energy barrier of 0.11 eV. With atomic arrangement equivalent to the (111)-Mo surface here, the MXene Mo_2C (0001) surface was also predicted to possess excellent CO_2 dissociation ability [194].

The TDTS and TDI happened to be in one elementary reaction step − the CO oxidation step, which was usually considered as the rate-determining step in the WGS reaction [71]. Thus, the energetic span was equal to the energy barrier of the CO oxidation step in this case shown in Figure 5.4.

5.2.3 The H_2O-assisted associative route

The H_2O-assisted associative route in the WGS reaction was recently proposed by Tong and Xu *et al*. [118]. This route is characterised by how CO combines with the OH group to form the HO–CO* intermediate compared to the associative route. In this route, the OH group of the HO–CO* intermediate was not from the surface-bonded OH*, but directly from physically adsorbed water molecules. Thus, O* species were usually already available on the surface before this reaction step occurred. Using the reconstructed surface models of fcc $TiC_x(111)O_y(OH)_z$ and $MoC_x(111)O_y(OH)_z$, they showed the steps of HO–CO* formation and its further dehydrogenation to CO_2 and H*. However, the surface dehydrogenation step results were not supplied, which was necessary to restore the substrate. Thus, they could not accurately compare the efficiency of the H_2O-assisted associative route with those of redox or associative routes, but only *via* certain elementary reaction steps.

Here, as shown in Figure 5.5, the Pt_1/(111)-Mo surface model doped with one surface O* was used, while the efficiency of the full Mo–O layer surface model was further considered and compared in the later chapter.

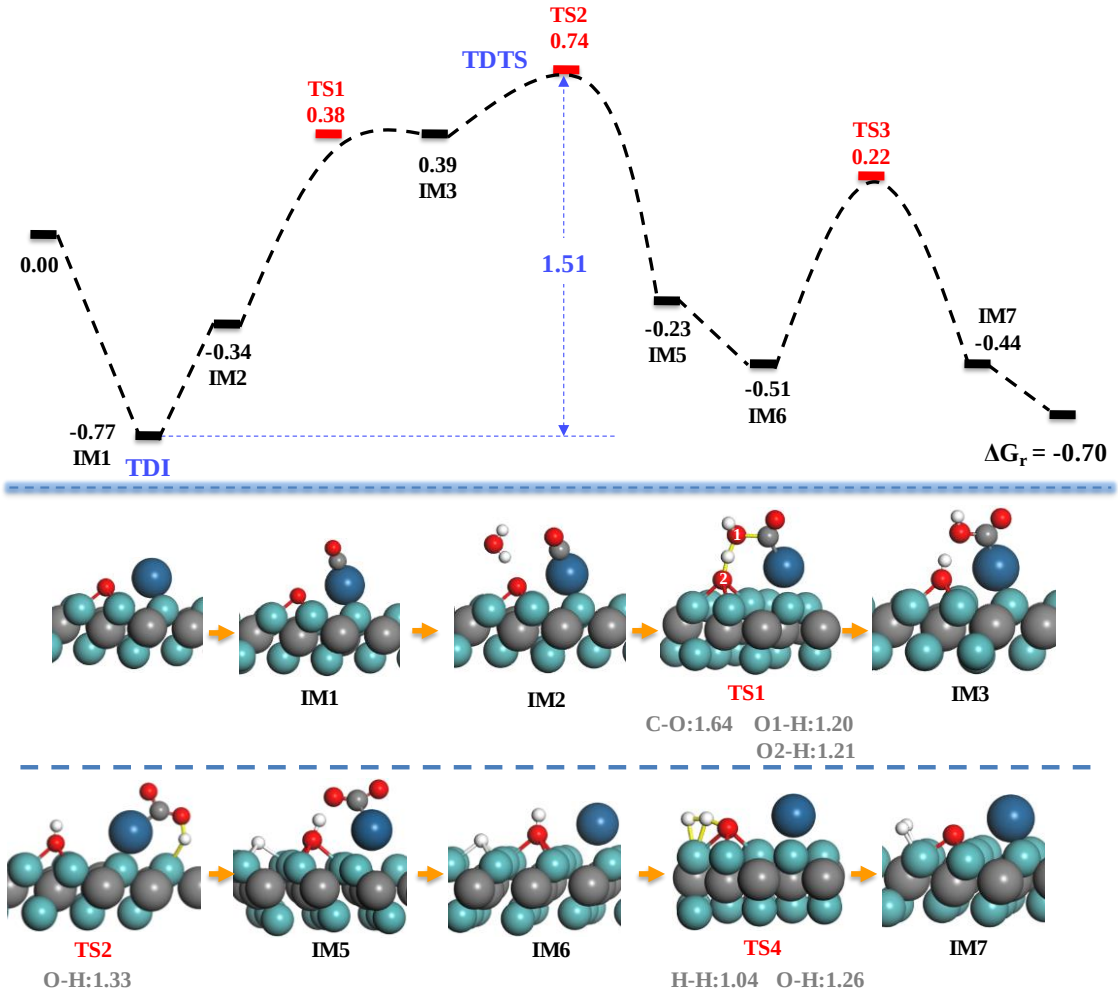

Figure 5.5 Free energy profile for the H_2O-assisted associative route on the original Pt_1/MoC (111)-Mo surface.

In the H_2O-assisted associative route, CO adsorbed on top of the Pt site, while the H_2O weakly interacted with the surface O* *via* a hydrogen bond of 1.85 Å (IM2). The physical adsorption of H_2O *via* the hydrogen bond elevated the free energy position by ~0.43eV, which was due to the fact that the weak van der Waals interaction could not compensate the entropy reduction effect at the WGS temperature (423.15 K). In the subsequent HO–CO* formation step (IM2 → TS1 → IM3), the surface O* captured one H atom from the

physiosorbed H_2O molecule, while the retained OH group combined with CO. The energy barrier of this elementary reaction step was 0.72 eV, which was significantly lower than that of the redox route (1.25 eV, IM5 → TS3 → IM6 in Figure 5.4) and comparable with that of the associative route (0.73 eV, IM3 → TS2 → IM4 in Figure 5.3). The formed HO–CO* intermediate was highly unstable, which would easily decompose back to CO and H_2O with negligible energy barrier. Besides, the HO–CO* intermediate could also directly transfer its H atom to the Mo site, which led to CO_2 and surface H* atom with an energy barrier of 0.33 eV (TS2). Similar to the redox route in Figure 5.4, the H_2 molecule was produced *via* the H-assisted OH* dehydrogenation, where the surface H* atom combined with the H atom of OH* to form one H_2 molecule (TS3).

The energy barrier of this step was 0.73 eV and almost thermodynamically neutral. The CO adsorption state (IM1) was identified as the TDI, while the HO–CO* dehydrogenation (TS2) was identified as the TDTS. The energetic span was 1.51 eV.

5.3 Results of the original Pt_1/(001) surface

5.3.1 The associative route

Wang *et al.* [113] proposed two possible pathways of the associative route for the WGS reaction on the original M_1/fcc-MoC (001) surface model (M_1 referred to Rh_1, Pd_1, Pt_1 and Au_1), namely, the M_1-site pathway and the Mo-site pathway.

In the M_1-site pathway, the doping metal atom directly participated in the reaction acting as a site for CO initial adsorption and subsequent activation processes. In the Mo-site

pathway, the Mo atom adjacent to the doping metal atom acted as the active site for the WGS reaction, with the doping atom as an electronic promoter enhancing the reactivity of the Mo site. However, they did not strictly establish the complete catalytic cycles, only considering certain elementary reaction steps. Their comparisons are for the different metal-doped (001) surface models based on the energy barriers of selected elementary reaction steps. Thus, in order to systematically and strictly compare the catalytic efficiencies of the original (001) surface with that of the (111) surface, the complete catalytic cycles on the (001) surface model should be established as requested by the ESM model.

(1) Mo-site pathway

As depicted in Figure 5.6, the adsorption of H_2O on the (001) surface was 0.12 eV endothermic, whereas it was 0.26 eV exothermic on the (111)-Mo surface (Figure 5.3), signifying less hydrophilicity of the (001) surface than that of the (111)-Mo surface.

The O–H cleavage of H_2O on the (001) surface was also facile with an energy barrier slightly higher than that on the (111)-Mo surface (0.57 *vs.* 0.44 eV), whereas the reaction energy of H_2O activation on the (001) surface was endothermic at 0.38 eV compared to that exothermic at 0.87 eV on the (111)-Mo surface, indicating a significant weaker H_2O chemisorption strength on the (001) surface.

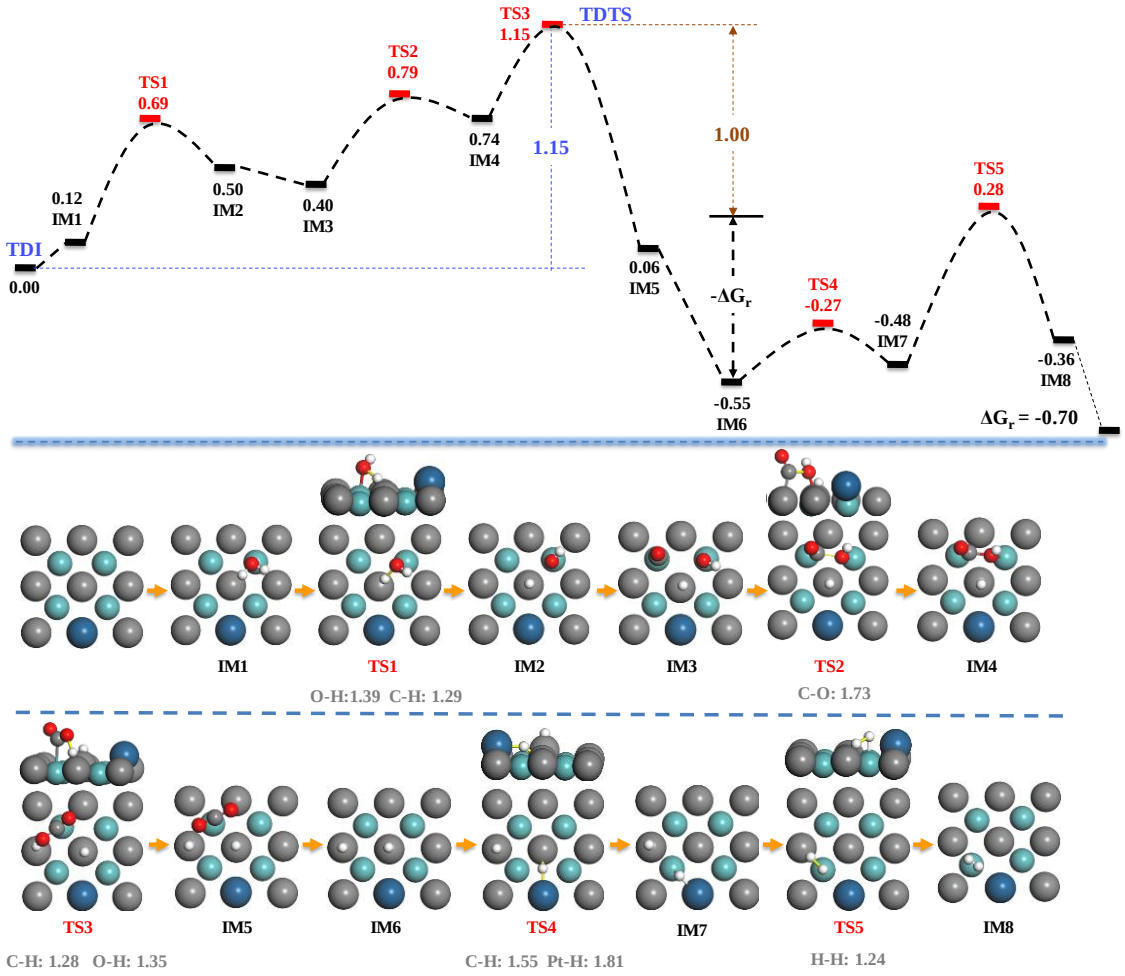

Figure 5.6 Free energy profile for the Mo-site pathway of associative route on the original Pt_1/MoC (001) surface.

In the Mo-site pathway, CO adsorbed on the Mo atom adjacent to the formed Mo–OH* group (IM3), and the subsequent combination of CO with the OH* formed the HO–CO* intermediate (IM4) with a small energy barrier of 0.39 eV. The formed HO–CO* intermediate was highly unstable and could readily dissociate back to CO and OH* with an energy barrier of only 0.05 eV. Though the elementary step of HO–CO* dehydrogenation to CO_2 was also kinetically and thermodynamically favourable (IM4 → TS3 → IM5), the first two steps (TS1 and TS2) were all endothermic, which pushed up

the energy position of TS3, thus making the dehydrogenation more difficult to occur than it looked like. After the desorption of CO_2 in IM5, two H* atoms remain on the surface, which would desorb as one H_2 molecule. One of the two H* atoms first migrated from the C site to the Pt–Mo interfacial site, forming a Pt–H bond of 1.80 Å and overcoming an energy barrier of 0.28 eV (IM6 → TS4 → IM7). Then, the combination of the two H* atoms in IM7 resulted in one H_2 molecule accompanied by the breaking of the C–H and Pt–H bonds. The energy barrier of the latter step was significantly larger than that of the H-migration step (0.76 *vs.* 0.28 eV).

The HO–CO* dehydrogenation transition state (TS3) was identified to be the TDTS, and the energetic span was 1.15 eV. The energy difference between TS3 and IM6 was as large as ~1.70 eV, but the actual hindrance formed by them was much smaller due to the compensation of the reaction energy (ΔG_r, Figure 5.6).

(2) M_1-site pathway

In the M_1-site pathway, CO adsorbed on the Pt site (IM3 in Figure 5.7) instead of the adjacent Mo site (IM3 in Figure 5.6) after H_2O activation. The adsorption strength for CO on the Pt site was significantly stronger than that on the adjacent Mo site (−0.73 *vs.* −0.1 eV), indicating a stronger electron-donating ability of Pt. The H_2O activation to form surface OH* appeared to be easier at the Pt–Mo interface (TS1 in Figure 5.7) than that on the more distant Mo site (TS1 in Figure 5.6), and the resulting surface OH* bonded to Pt (2.26Å) and Mo (2.13 Å) sites at the Pt–Mo interface, while only a Mo–O bond (2.01 Å)

formed on the more distant Mo site. The combination of CO with OH* on the Pt site had an energy barrier larger than that on the Mo site (0.72 *vs.* 0.39 eV), which showed a similar trend supported by Wang and co-workers [113]. The formed HO–CO* intermediate on the Pt site (IM4 in Figure 5.7) seemed to be more stable than that on the Mo site (IM4 in Figure 5.6), where the C–O dissociation barrier of HO–CO* on the Pt site was larger than that on Mo site (0.23 *vs.* 0.05 eV). The following HO–CO* dehydrogenation (TS3), H* migration (TS4) and combination of surface H* atoms (TS5) had comparable energy barriers with those in the Mo-site pathway.

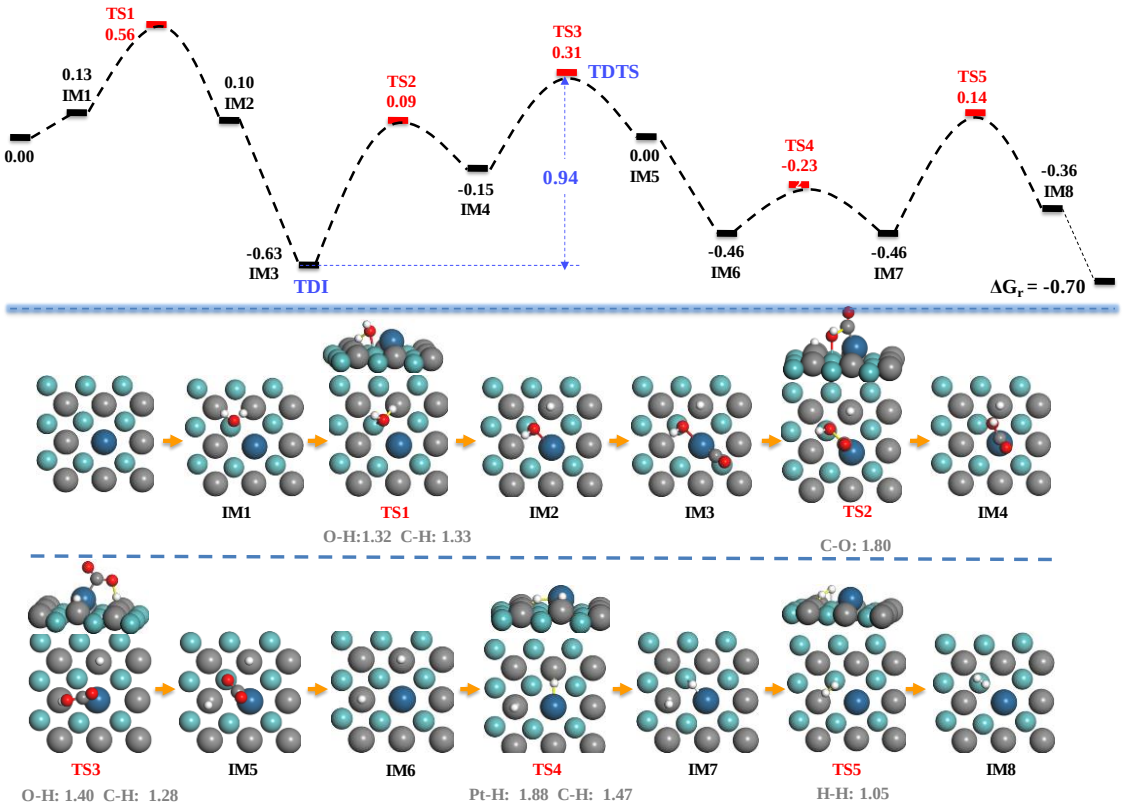

Figure 5.7 Free energy profile for the M_1-site pathway of associative route on the original Pt_1/MoC (001) surface.

The HO–CO* dehydrogenation transition state (TS3) was the TDTS same as that of the Mo-site pathway, whereas the CO adsorption state (IM3) was located as the TDI due to the significant adsorption strength of CO on the Pt site.

5.3.2 The H_2O-assisted associative route

By analogy with the H_2O-assisted associative route on the original (111)-Mo surface (Figure 5.5), a similar route on the original (001) surface model was also explored and established, as shown in Figure 5.8.

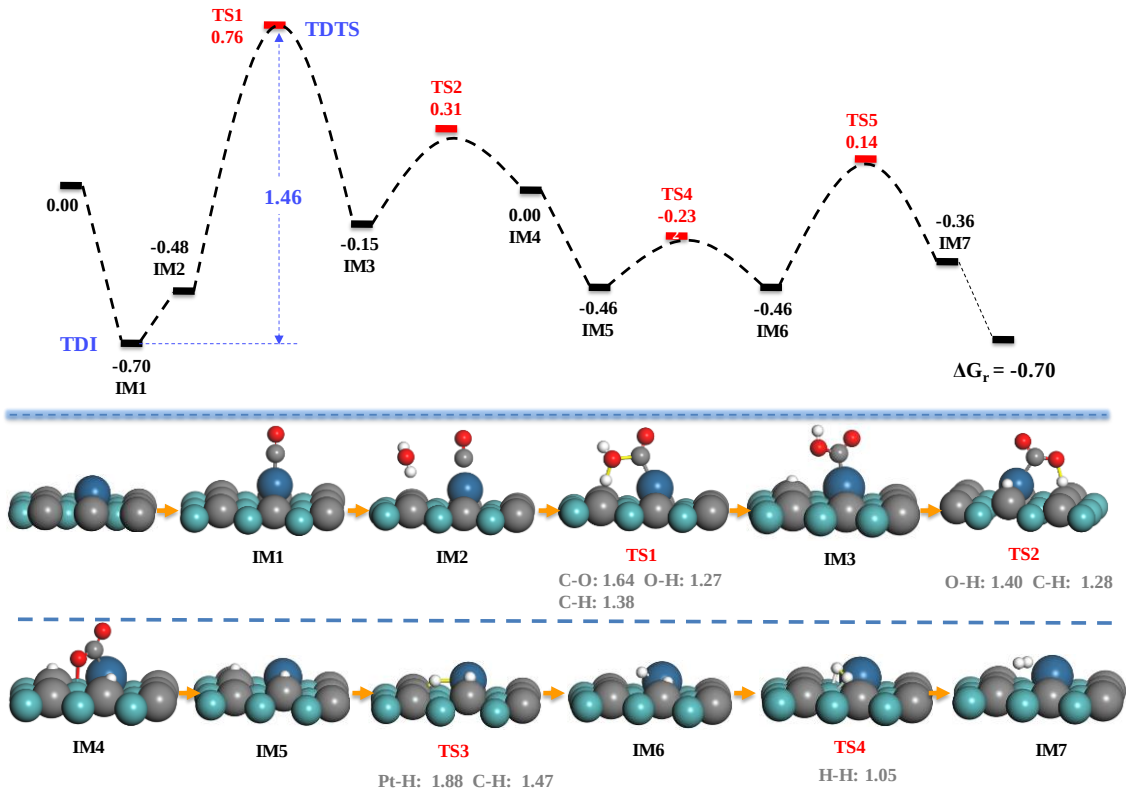

Figure 5.8 Free energy profile for the H_2O-assisted associative route on the original Pt_1/MoC (001) surface.

Adsorption of CO on the Pt site was followed by one H_2O anchoring to a nearby C site

through a weak hydrogen bond of 2.16 Å (IM2). Adsorption of CO lowered the free energy position by ~0.70 eV, whereas the co-adsorption of H_2O *via* hydrogen bond elevated the free energy position by ~0.22eV due to the entropy reduction effect at 423.15 K. In the subsequent HO–CO* formation step (IM2 → TS1 → IM3), the surface C site captured one H atom from the physiosorbed H_2O molecule, while the CO combined with the leftover OH group to form the HO–CO* intermediate. The energy barrier of the HO–CO* formation step was significantly larger than that on the MoC (111)-Mo surface (1.24 *vs.* 0.72 eV), which may be ascribed to the less efficiency of the H transfer between C and O on the MoC (001) surface (Figure 5.8, TS1) than that between both O atoms on the MoC (111)-Mo surface (Figure 5.5, TS1). The subsequent dehydrogenation of HO–CO* to CO_2 occurred *via* the H transfer between the HO–CO* and another C site overcoming an energy barrier of 0.46 eV. After CO_2 desorption, the surface dehydrogenation steps were all the same with those of the associative route (Figure 5.6).

The HO–CO* intermediate formation (TS1) was the TDTS, while the CO adsorption state (IM1) was the TDI. The energetic span was 1.46 eV, notably larger than the associative routes (Figure 5.6 and Figure 5.7).

5.4 Discussion of WGS on the original Pt_1/fcc MoC surface

The catalytic efficiencies of the specific surface phase structures were evaluated and compared *via* their respective turnover frequency (TOF), which could be determined by the energetic span model (ESM) [121]. The ESM model breaks the limitations of the

elementary reaction step as the 'primitive unit' in the catalytic cycle. Instead, the actual 'energy barrier' or the energetic span (equations (3-35) and (3-36)) depends on all the permutations between intermediates and transition states of a catalytic cycle, thus incorporating much more comprehensive kinetic information. In most cases, the ESM model showed that conclusions based only on the energy barriers of elementary reaction steps or on the single rate-determining step could not reflect the actual situation.

Taking the three reaction routes on the original Pt_1/(111)-Mo surface as an example, the energy barriers of ~0.44 to 0.88 eV in the associative route (Figure 5.3) and of ~0.35 to 0.73 eV in the H_2O-assisted associative route (Figure 5.5) were obviously lower than those of ~0.44 to 1.25 eV in the redox route (Figure 5.4). In the language of the 'rate-determining step', the energy barrier for the rate-determining step of 0.88 eV in the associative route (IM6→TS4 in Figure 5.3) and of 0.73 eV in the H_2O-assisted associative route (IM5→TS3 in Figure 5.5) were both lower than that of 1.25 eV in the redox route (IM5→TS3 in Figure 5.4). Thus, one may conclude that the efficiency order of the routes on the original (111)-Mo surface was H_2O-assisted associative route > associative route > redox route. However, using the energetic span (δE) of the ESM model, which considers all the energy states in a catalytic cycle (equations (3-35) and (3-36)), the efficiency order was redox route (1.25 eV, Figure 5.4) > associative route (1.47 eV, Figure 5.3) ~ H_2O-assisted associative route (1.51 eV, Figure 5.5), which was opposite to that depending on energy barriers of the elementary reaction steps.

Besides the comparisons among the efficiencies of different reaction routes, the concept

of the rate-determining step could also mislead the structure–performance relationship conclusion. For example, the energy barriers of the total five elementary reaction steps in the Mo-site pathway of the associative route on the original Pt_1/(001) surface (Figure 5.6) were 0.57 eV (H_2O activation, TS1), 0.39 eV (HO–CO* intermediate formation, TS2), 0.41 eV (HO–CO* dehydrogenation, TS3), 0.28 eV (H* migration, TS4) and 0.76 eV (H_2 formation, TS5), respectively. Thus, from the concept of the rate-determining step, the H_2 formation step was the one most frustrating the catalytic efficiency. However, it would be misleading for researchers to focus on how to improve the dehydrogenation ability of the substrate for better catalytic reactivity. Instead, the HO–CO* dehydrogenation transition state was the one mostly limiting the TOF according to the ESM method, where the HO–CO* dehydrogenation state possessed a significantly larger normalised degree of TOF control (X_{TOF}, equation (3-35)) than the H_2 formation state (0.9997 *vs.* 0.0002) indicating that finding new pathways of higher activity in HO–CO* dehydrogenation (TS3, Figure 5.6) could accelerate TOF to the maximum extent. It should be noted here that the aforementioned argument based on the X_{TOF} holds true if only no obvious changes occurred in the energy states of other intermediates or transition states when the energy states of TDTS or TDI were changed.

Table 5.1 compares the TOF values and TOF-determining states of various WGS routes on original Pt doped (111)-Mo and (001) surfaces, and in this table different routes are replaced by abbreviations, A for the associative route, R for the redox route and WA for the H_2O-assisted associative route.

Table 5.1 TOF values and TOF-determining states of various WGS routes on original Pt doped (111)-Mo and (001) surfaces.

Surface Phase	Route	TOF (h^{-1})	TDI (figure no., label)	TDTS (figure no., label)
Pt_1/(111)-Mo	A	1.18×10^{-1}	H/OH/CO co-adsorption (Fig. 5.3, IM3)	HO–CO* dehydrogenation (Fig. 5.3, TS3)
Pt_1/(111)-Mo	R	4.87×10^{1}	O/CO co-adsorption (Fig. 5.4, IM5)	CO oxidation (Fig. 5.4, TS3)
Pt_1/(111)-Mo	WA	3.21×10^{-2}	CO adsorption (Fig. 5.5, IM1)	HO–CO* dehydrogenation (Fig. 5.5, TS2)
Pt_1/(001)	A(Mo-site)	6.21×10^{2}	gas phase CO and H_2O (Fig. 5.6)	HO–CO* dehydrogenation (Fig. 5.6, TS3)
Pt_1/(001)	A(Pt-site)	1.95×10^{5}	H/OH/CO co-adsorption (Fig. 5.7, IM3)	HO–CO* dehydrogenation (Fig. 5.7, TS3)
Pt_1/(001)	WA	1.16×10^{-1}	CO adsorption (Fig. 5.8, IM1)	HO–CO* formation (Fig. 5.8, TS1)

For the three reaction routes on the original Pt_1/(111)-Mo surface (Figures 5.3–5.5 and Table 5.1), the redox route was the most efficient one with TOF of 48.7 h^{-1} at 423.15 K, the TOF of which was comparable with that of 1.72 h^{-1} on Pt_1/TiO_2 [175] and of 3.64 h^{-1} on Pt_1/MgO [195] at 298.15 K for the CO oxidation reactions. The TDTS and TDI of the redox route (Figure 5.4) happened to be in one reaction step − the CO oxidation step, whereas they were in different reaction steps on the other two routes (Figures 5.3 and 5.5). By comparison, the catalytic efficiency of the original Pt_1/(001) surface was significantly larger than that of the original Pt_1/(111)-Mo surface, where the TOFs of the associative routes on the original Pt_1/(001) surface were 1 to 4 orders of magnitude larger than the redox route on the original Pt_1/(111)-Mo surface (Table 5.1). The large discrepancy of the catalytic efficiencies between the original Pt_1/(111)-Mo and Pt_1/(001) surfaces could be explained by the principle of Sabatier [102-104], which claims that the surface binding strength of intermediates should be neither too weak nor too strong, in other words, only the moderate surface binding strength will lead to the most efficient catalytic cycle. Note that both the associative route and the redox route belong to the Langmuir-Hinshelwood [196, 197] category, where the reaction proceeds between CO adsorbing on the metal site and H_2O dissociative adsorption on the substrate. Thus, the catalytic efficiencies of the associative or the redox routes cannot avoid Sabatier's rule. The (111)-Mo surface of fcc MoC was found to be much more hydrophilic than the (001) surface, where the surface binding strength towards the O-containing species (H_2O, OH* and O*) was much stronger on the (111)-Mo surface than that on the (001) surface. Consistently, the

energetic positions of the intermediates in the redox or the associative routes on the original Pt_1/(111)-Mo surface (Figures 5.3 and 5.4) were significantly lower than those on the original Pt_1/(001) surface (Figures 5.6 and 5.7), which greatly decelerate the turnover speed of the intermediates on the original Pt_1/(111)-Mo surfaces. Instead of dissociative adsorption of H_2O on the substrate like in the redox and associative routes, the H_2O to be reacted pre-adsorbed on the surface *via* a weak hydrogen bond (Figures 5.5 and 5.8) in the H_2O-assisted associative route. Due to the low efficiency of H-transfer in HO–CO* intermediate dehydrogenation (Figure 5.5, TS2) and HO–CO* intermediate formation (Figure 5.8, TS1), both the original Pt_1/(111)-Mo and Pt_1/(001) surfaces showed relatively lower TOFs of the H_2O-assisted associative route compared with those of the associative and the redox routes (Table 5.1).

5.5 Summary

This chapter presented DFT studies of the water-gas shift reaction on the original Pt_1/fcc MoC surface considering the effects of different crystal facets ((111) *vs.* (001)) and different reaction routes (redox route, associative route, and H_2O-assisted associative route). The catalytic efficiencies were quantified *via* the TOF calculated by the ESM. For the original (111)-Mo surfaces, the redox route (4.87×10^{1} h^{-1}) was more efficient than the associative route (1.18×10^{-1} h^{-1}) and the H_2O-assisted associative route (3.21×10^{-2} h^{-1}). Meanwhile, for the original (001) surfaces, the associative routes *via* the Pt-site pathways (1.95×10^{5} h^{-1}) showed significantly higher TOFs than the Mo-site pathways (6.21×10^{2} h^{-1}) and the H_2O-assisted associative route (1.16×10^{-1} h^{-1}).

Chapter 6 Results and Discussion (III): WGS on evolved surface of Pt_1/fcc MoC

The catalytic performance of heterogeneous catalysts is closely related to the surface phase reconstructions resulting from the interactions between the original surfaces and the reactants/products. In the previous chapter, the evolution of the surface phase structure of the (001) surface was systematically investigated, and the (001) surface exhibited rather different evolution patterns compared to that of the (111)-Mo surface [108]. Under the H_2/H_2O atmosphere, surfaces with different physicochemical properties were expected to exhibit different surface phase structural evolution patterns. It was therefore important to explore and compare the catalytic efficiencies of different surface phase structures. The original (001) surface was mostly covered by a mixture of surface OH* and H_2O*. In contrast, the original (111)-Mo surface was readily covered with OH* groups due to the fast kinetics of H_2O activation. The surface OH* layer would gradually dehydrogenate to form a more thermodynamically stable Mo–O monolayer.

In this chapter, different routes (the associative route, the redox route, and the water-assisted associative route) for the water-gas shift on the evolved surface of Pt_1/fcc MoC were presented, considering the difference between (111) and (001) facets. The energetic span model, which was introduced in Chapter 3, is employed to evaluate and compare the TOF of different catalytic cycles on different facets of Pt_1/fcc MoC catalysts.

6.1 Construction of the evolved surface

The original surfaces exposed under the H_2O/H_2 atmosphere would quickly be covered by formed species, leading to different reactive properties, which is also the important basis for this thesis. In this section, the original surfaces covered with species such as H_2O*, OH*, and O* are denoted as $(H_2O)_x(OH)_y(O)_z$ and reasonable covering surfaces would be constructed for subsequent discussion, as shown in Figures 6.1 ~ 6.4.

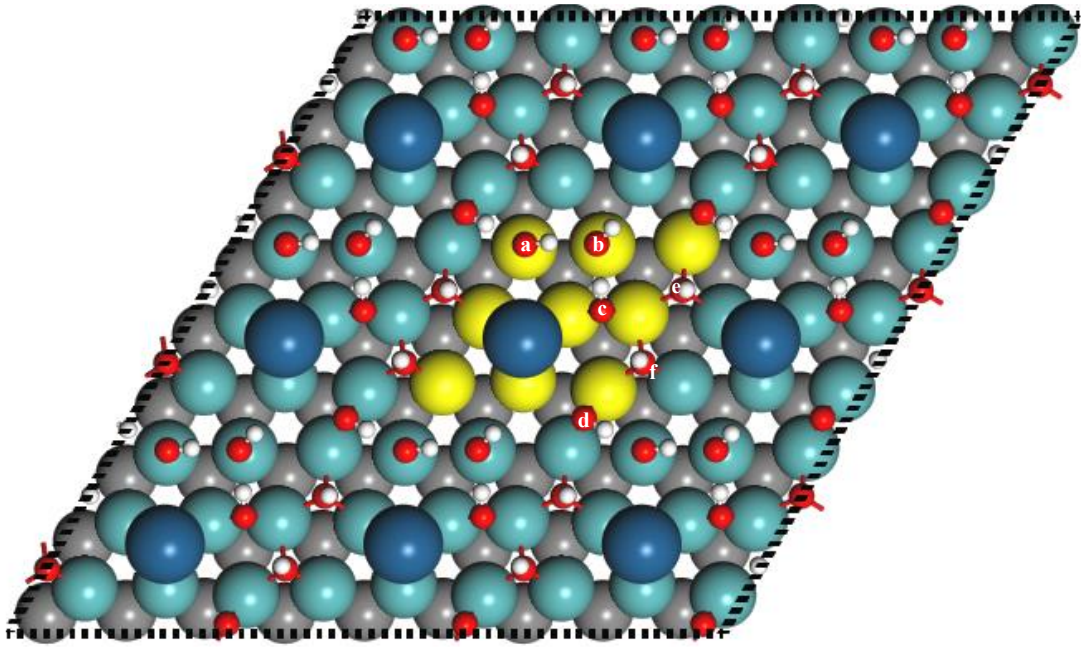

Figure 6.1 Surface phase structure of Pt_1/(111)-$Mo(OH)_{3/4}$ ML (top view).

Figure 6.1 shows the top view of the surface phase structure with 3/4 ML OH* coverage, denoted as Pt_1/(111)-$Mo(OH)_{3/4\ ML}$. The Mo atoms highlighted in yellow constituted the periodic surface of *p*(3×3) supercell model used in this study, and the six OH groups labelled from a to f were the corresponding surface OH groups on this model. Here, green balls represent Mo atoms, grey balls represent C atoms, blue balls represent Pt atoms, red

balls represent O atoms, and white balls represent H atoms, only the top two layers were presented in the top view for clarity (this notation is same in the following three figures).

There were three types of OH* in Pt_1/(111)-$Mo(OH)_{3/4\ ML}$, which were called the top site (a, b), bridge site (c, d) and cavity site OH* (e, f), depending on the number of bonds formed between Mo and OH*. According to [108], the cavity site OH* is the only stable configuration with surface OH* coverage (θ_{OH}) ≤ 4/9 ML, while the top site and bridge site OH* will emerge on the surface structures with θ_{OH} ≥5/9 ML, and the hydrogen bonds contribute a lot to the stability of top site and bridge site OH*.

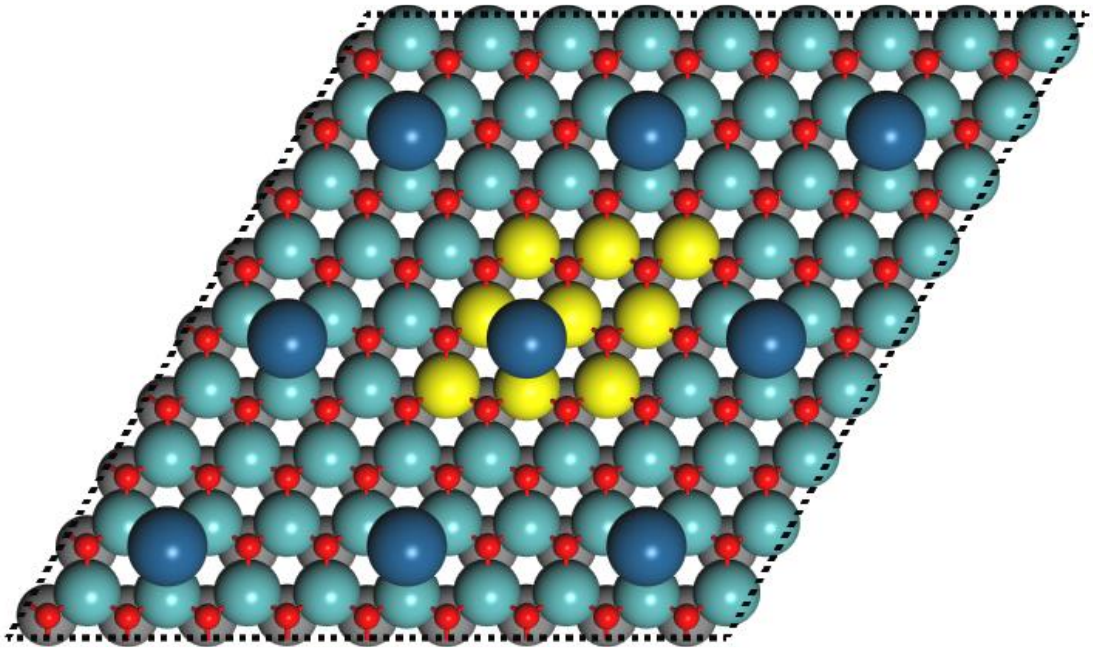

Figure 6.2 Surface phase structure of Pt_1/(111)-$Mo(O)_{1ML}$ (top view).

Figure 6.2 shows the top view of the surface phase structure with 1 ML O* coverage, denoted as Pt_1/(111)-$Mo(O)_{1ML}$. The Mo atoms highlighted in yellow constituted the periodic surface of $p(3\times3)$ supercell model used in this study. The cavity site O* is

consistently the most stable configuration with surface O* coverage ranging from 0 to 1 ML. The DFT and AIMD results showed that the top site O* was highly unstable and readily evolved into cavity site O* with strong surface binding strength. Furthermore, the hcp site O* was always more stable than the fcc site O*, which was also supported by the DFT calculations by Xu *et al*.

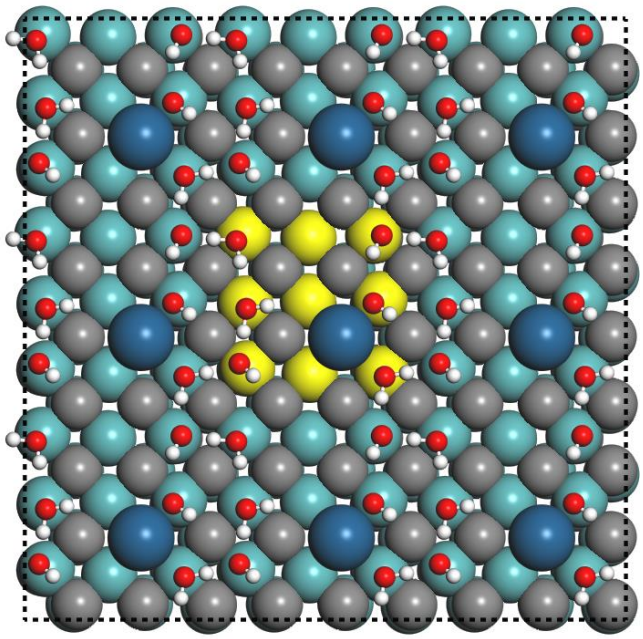

Figure 6.3 Surface phase structure of $Pt_1/(001)\text{-}(H_2O)_{3/8ML}(OH)_{3/8ML}$.

Figure 6.3 shows the top view of the surface phase structure with 3/8 ML H_2O coverage. The Mo atoms highlighted in yellow constituted the periodic surface of $p(3\times3)$ supercell model used in this study.

The surface phase diagram of (001) surface in the previous chapter showed that stable surface phase structures usually contained 1/3 to 4/9 ML OH* groups with other sites vacant or adsorbed by H_2O under most of the WGS gas phase compositions. The

$Pt_1/(001)\text{-}(H_2O)_{3/8ML}(OH)_{3/8ML}$ surface phase structure was thus accordingly constructed.

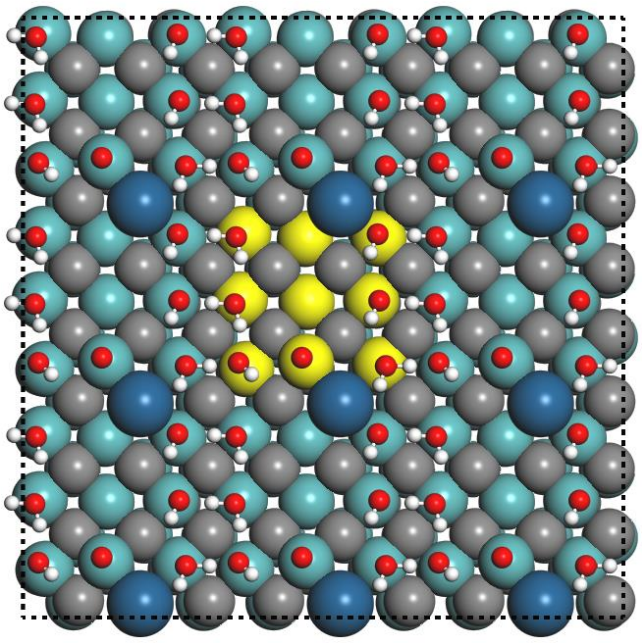

Figure 6.4 Surface phase structure of $Pt_1/(001)\text{-}(H_2O)_{3/8ML}(OH)_{3/8ML}(O)_{1/8ML}$.

Figure 6.4 shows the top view of the surface phase structure with 1/8 ML O*, 3/8 ML H_2O and 3/8 ML OH* coverage. The Mo atoms highlighted in yellow constituted the periodic surface of *p*(3×3) supercell model used in this study.

The surface phase diagram of the (001) surface in the previous chapter showed that the (001) surface was usually covered by OH* groups and physiosorbed H_2O molecules in the typical WGS reaction conditions, whereas a small proportion of surface OH* could further dehydrogenate to surface O* atoms at very low H_2 pressures. Thus, the $Pt_1/(001)\text{-}(H_2O)_{3/8ML}(OH)_{3/8ML}(O)_{1/8ML}$ surface model was constructed according to the results of the surface phase diagram.

6.2 Results of the $Pt_1/(111)\text{-}(H_2O)_x(OH)_y(O)_z$ surface

According to the literature [108], the (111)-Mo surface was readily covered by surface OH* in the initial stage of the WGS reaction, and the gradual dehydrogenation of surface OH* would finally transform the Mo–OH surface layer into a Mo–O* surface layer, the process being driven by thermodynamics. Therefore, both the Mo–OH surface layer and Mo–O surface layer have been considered in this study.

6.2.1 The associative route

For the WGS mechanism on the $Pt_1/(111)\text{-}Mo(OH)_{3/4}$ ML surface phase (Figure 6.1), the existence of surface OH* groups fostered the associative route, where the combination of CO with OH* led to CO oxidation and surface OH* consumption. There were three types of OH* on the (111)-Mo surface, called the cavity site, bridge site and the top site OH*, depending on the number of bonds formed between Mo and OH* [108]. The top site OH* was the most reactive one with the least steric hindrance around its O atom, and it could exist stably on surfaces with OH* coverage of no less than 5/9 ML. Considering the OH coverage in this case (> 5/9 ML), the top site OH* was selected to participate in the reaction directly.

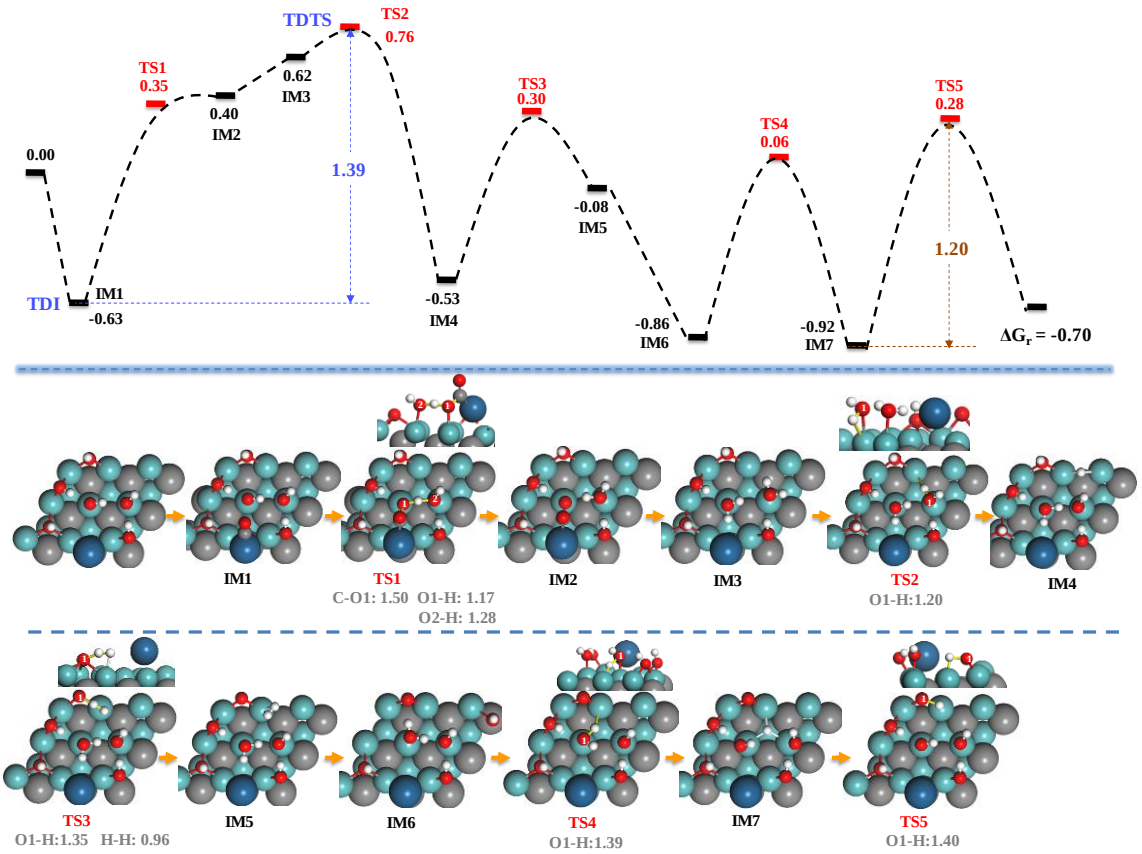

Figure 6.5 Free energy profile for the associative route on the Pt_1/(111)-$Mo(OH)_{3/4}$ ML surface phase.

As shown in Figure 6.5, the adsorption strength of CO on the Pt site (IM1) was still strong compared with those on the original surfaces (Figure 5.3). Following the CO adsorption, the combination of CO with two top-site OH* groups occurred, where the HO–CO* intermediate formation with the first OH* and its subsequent dehydrogenation to CO_2 with the second OH* proceeded simultaneously (TS1). The energy barrier at 0 K with the ZPE correction was 0.92 eV which was in accord with that of 0.91 eV calculated by Ma *et al*. [48]. After CO_2 desorption, one H_2O adsorbed on the vacant Mo site previously occupied by the OH* group (IM3). Then, two H_2O molecules existed on the surface (IM3),

while one was generated in place during CO_2 formation, and the other was replenished from the gas phase. Activation of the first H_2O molecule resulted in a surface H* atom and regeneration of a top site OH* (TS2). Desorption of the surface H* in IM4 was assisted by a nearby cavity site OH* group, the H atom of which combined with the surface H* to form a H_2 molecule with itself dehydrogenated to the surface O* atom (TS3). Then, activation of the second H_2O molecule led to the second top site OH* regeneration and another surface H* formation (TS4). Finally, the migration of the surface H* to the surface O* atom restored the cavity site OH* and the whole surface (TS5).

The CO adsorption state (IM1) was TDI, while the activation of H_2O (TS2) was TDTS. For the associative route, the energetic span showed that the catalytic efficiency of the Mo–OH layer phase (1.39 eV, Figure 6.5) was comparable with that of the original surface (1.47 eV, Figure 5.3).

6.2.2 The redox route

Figure 6.6 shows the redox route on the Mo–O monolayer phase. CO firstly adsorbed on the Pt site with a significant adsorption energy of −0.82 eV. Then, the CO was oxidised by an adjacent surface O* atom to form CO_2. The distance of Pt···C increased from 1.93 Å in IM1 to 2.02 Å in TS1, whereas C···O distance decreased from 3.00 Å in IM1 to 1.61 Å in TS1, and finally to 1.33 Å, forming a C–O bond.

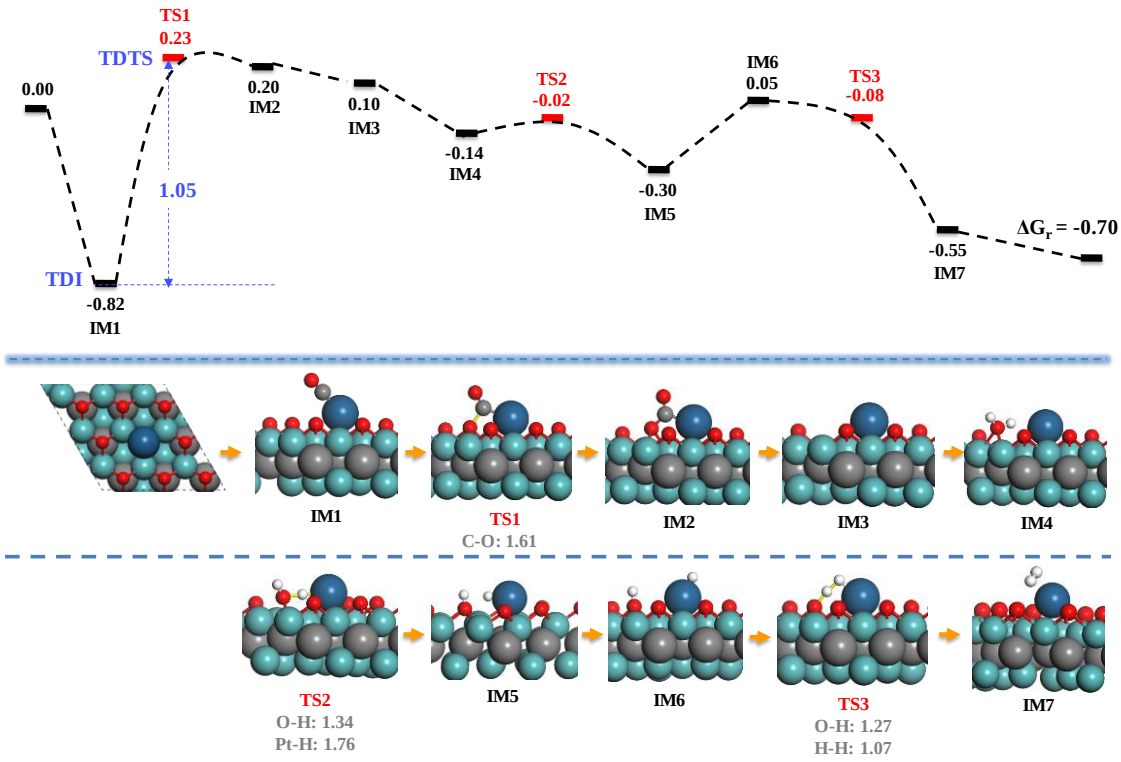

Figure 6.6 Free energy profile for the redox route on the Pt_1/(111)-$Mo(O)_{1ML}$ surface phase.

The energy barrier of the CO oxidation step on Mo–O monolayer of the MoC (111)-Mo surface was lower than that on the original one (1.04 *vs.* 1.25 eV), which may be ascribed to the weakened surface binding strength of O* with coverage increasing [108]. It should be noted here that the corresponding reverse reaction, *i.e.* CO_2 dissociation to CO and surface O*, was facile with a negligible energy barrier of 0.03 eV. The spontaneous desorption of the CO_2 left an O* vacancy (O_v) on the Mo-O monolayer surface (IM3) with a free energy change of −0.1 eV. One H_2O molecule then filled the O_v site near the Pt site with an adsorption energy of −0.24 eV. During the subsequent O–H activation of the adsorbed H_2O, the cleaved H atom transferred to the nearby Pt site forming a Pt–H

bond, while the retained OH* filled the O_v site. The energy barrier of H_2O activation on the Pt–O_v site was only 0.12 eV, which was lower than those on the original (111)-Mo (Figure 5.3 and Figure 5.4) and (001) surfaces (Figure 5.6 and Figure 5.7). After a migration of the H* to a proper position on the Pt site (IM5→IM6), the combination of two H* atoms from the Pt–H* and the OH* formed a H_2 molecule with a negligible energy barrier, and the desorption of the H_2 from the Pt site finally restored the Mo-O layer phase.

Similar to that on the original MoC (111)-Mo surface (Figure 5.4), the TDTS and TDI happened to be the transition state (TS1) and reactant (IM1) in the CO oxidation step, respectively. The energetic span of 1.04 eV on the Mo-O layer phase was smaller than that of 1.25 eV on the original surface (Figure 5.4).

6.2.3 The H_2O-assisted associative route

Figure 6.7 shows the H_2O-assisted associative route on the Mo–O monolayer phase. Same with the associative route (Figure 6.5) or the redox route (Figure 6.6), the adsorption of CO on the Pt site was an indispensable step, and the binding strength was also strong (IM1).

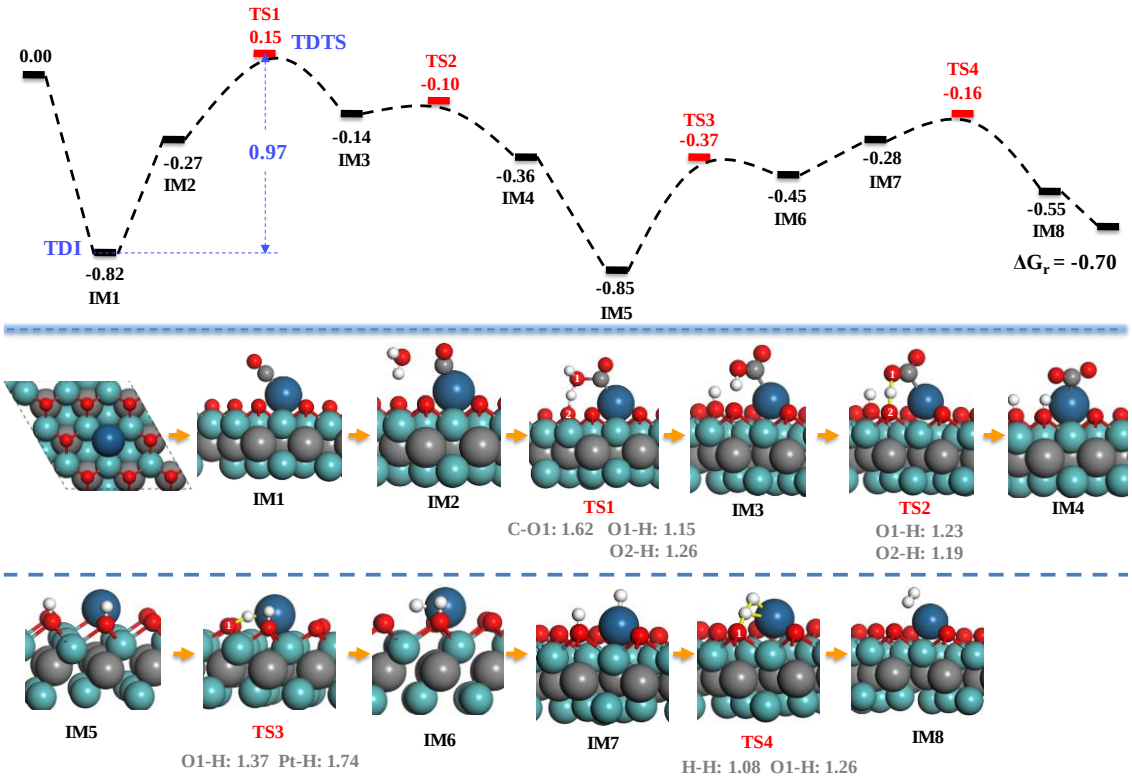

Figure 6.7 Free energy profile for the H_2O-assisted associative route on the Pt_1/(111)-$Mo(O)_{1ML}$ surface phase.

Following the CO adsorption, one H_2O molecule was weakly attached to the Mo–O monolayer through the hydrogen bond, which pulled up the free energy position by ~0.55 eV due to the relatively larger entropy reduction effect compared to the van der Waals interaction. Then, one O* of the surface Mo–O monolayer abstracted one H atom from the hydrogen-bonded H_2O molecule, while the CO* bonded with the retained OH group to form an HO–CO* intermediate. The energy barrier for the HO–CO* intermediate formation was only 0.42 eV which was obviously lower than that of 0.72 eV on the original (111)-Mo surface (Figure 5.5). The formed HO–CO* intermediate could readily dehydrogenate to CO_2 with the cleaved H atom transferring to another O* site of the

surface Mo–O layer (TS2). The energy barrier for the HO–CO* dissociating back to CO and H_2O was larger than its further dehydrogenation to CO_2 (0.29 *vs.* 0.04 eV), which could greatly accelerate the WGS reaction. After CO_2 desorption, the two surface OH* formed should dehydrogenate to restore the surface Mo–O layer. Firstly, one of the two OH* delivered its H atom to the nearby Pt site to form a surface Pt–H species (IM5 → TS3 → IM6). Secondly, after a migration of the H* to the proper position on the Pt site (IM6→IM7), the combination of the two H* atoms from Pt and the surface OH* formed one H_2 molecule (TS4), whose desorption finally restored the surface Mo–O layer.

Compared with the same route on the MoC (111)-Mo surface, the TDTS now changed from the HO–CO* dehydrogenation (TS2 in Figure 5.5) to HO–CO* formation (TS1 in Figure 6.7) due to the fact that multiple surface O* sites on Mo–O layer facilitated the HO–CO* dehydrogenation, whereas the TDI were both the CO adsorption state (IM1 in Figure 5.5 and Figure 6.7) indicating that the strong CO binding strength was unfavourable towards the WGS reaction.

6.3 Results of $Pt_1/(001)\text{-}(H_2O)_x(OH)_y(O)_z$ surface

According to the results and discussion in Chapter 4, the (001) surface of fcc MoC was usually covered by OH groups and physiosorbed H_2O molecules in the typical WGS reaction conditions, while a small proportion of surface OH* could further dehydrogenate to surface O* atoms at very low H_2 pressures. Thus, the surfaces covered with H_2O/OH and H_2O/OH/O were considered here. Similar to the routes on the original MoC (001)

surfaces, the Mo-site and M_1-site pathways of the associative route were established on the evolved MoC (001) surfaces. Besides, the feasibility of the redox route was also considered on the (001) surface covering with H_2O/OH/O. The evolved Pt_1/(001)-$(H_2O)_x(OH)_y(O)_z$ surface phases are shown in Figure 6.3 and Figure 6.4.

6.3.1 The associative route

(1) Mo-site pathway

For the Mo-site pathway of the associative route, as shown in Figure 6.8, the combination of the adsorbed CO with the existing surface OH* group must surmount an energy barrier of ~0.80 eV (TS1), which was larger than that of 0.39 eV on the original MoC (001) surface (TS2 in Figure 5.6).

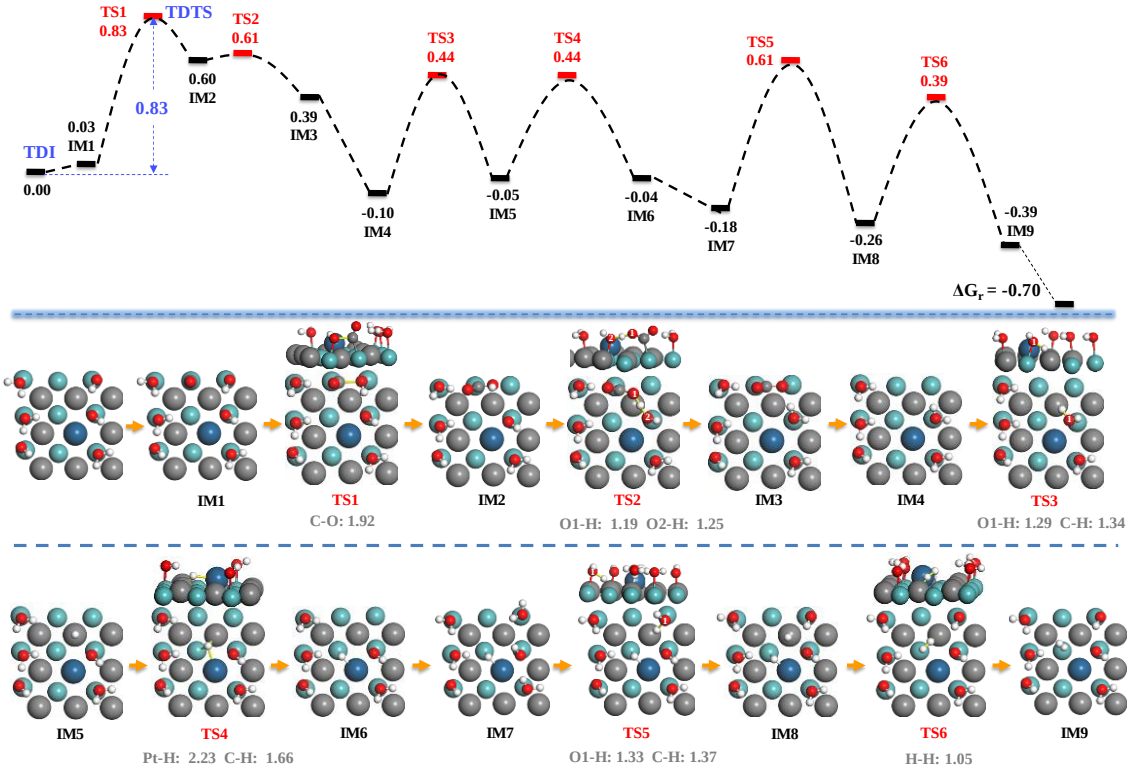

Figure 6.8 Free energy profile for the Mo-site pathway of associative mechanism on the $Pt_1/(001)\text{-}(H_2O)_{3/8ML}(OH)_{3/8ML}$ surface phase.

The increased energy barrier was aroused by the weakening or breaking the hydrogen bonds formed between the OH* and the surrounding H_2O molecules during the combination of CO with OH*. The lengths of hydrogen bonds between the OH* and the surrounding H_2O molecules increased from 1.78 and 1.53 Å in the reactant (IM1) to 1.93 and 3.53 Å in the transition state (TS1), respectively. By contrast, hydrogen bonds had no such resistance on the original surface (TS2 in Figure 5.6). Once the HO–CO* intermediate (IM2) is formed, its further dehydrogenation to CO_2 could readily occur *via* H transfer between the HO-CO* and a second OH* group (TS2). With the aid of the surface OH*, the dehydrogenation energy barrier was decreased from 0.41 eV on the

original surface (TS3 in Figure 5.6) to 0.01 eV here. Until IM4, two OH* groups participated in the CO conversion steps, one was consumed by its direct binding with CO (TS1), and the other was hydrogenated to form an H_2O molecule (TS2). After the desorption of CO_2, the replenishment and activation of H_2O to regenerate the two OH* groups were necessary (TS3 and TS5), meanwhile the migration (TS4) and combination (TS6) of H* atoms to form H_2 were also indispensable to finally restore the surface structure.

Compared with the original surface (Figure 5.6), the TDTS has changed from the HO–CO* dehydrogenation transition state to the HO–CO* formation transition state on the $Pt_1/(001)\text{-}(H_2O)_{3/8ML}(OH)_{3/8ML}$ surface phase (Figure 6.8). It was because the energy barrier of HO–CO* dehydrogenation could be significantly lowered with the assistance of abundant OH* groups on the $Pt_1/(001)\text{-}(H_2O)_{3/8ML}(OH)_{3/8ML}$ surface phase. Though the energy barrier of the HO–CO* formation step was larger, the energetic span of 0.83 eV on the $Pt_1/(001)\text{-}(H_2O)_{3/8ML}(OH)_{3/8ML}$ surface phase turned out to be lower than that of 1.15 eV on the original surface (Figure 5.6).

(2) M_1-site pathway

For the M_1-site pathway of the associative route (Figure 6.9), CO adsorbed on the Pt site with an adsorption energy significantly larger than that on the Mo site (−0.69 *vs.* 0.03 eV). However, the energy barrier for the combination of surface OH* and CO was almost the same as that on the Mo-site pathway (0.79 *vs.* 0.80 eV).

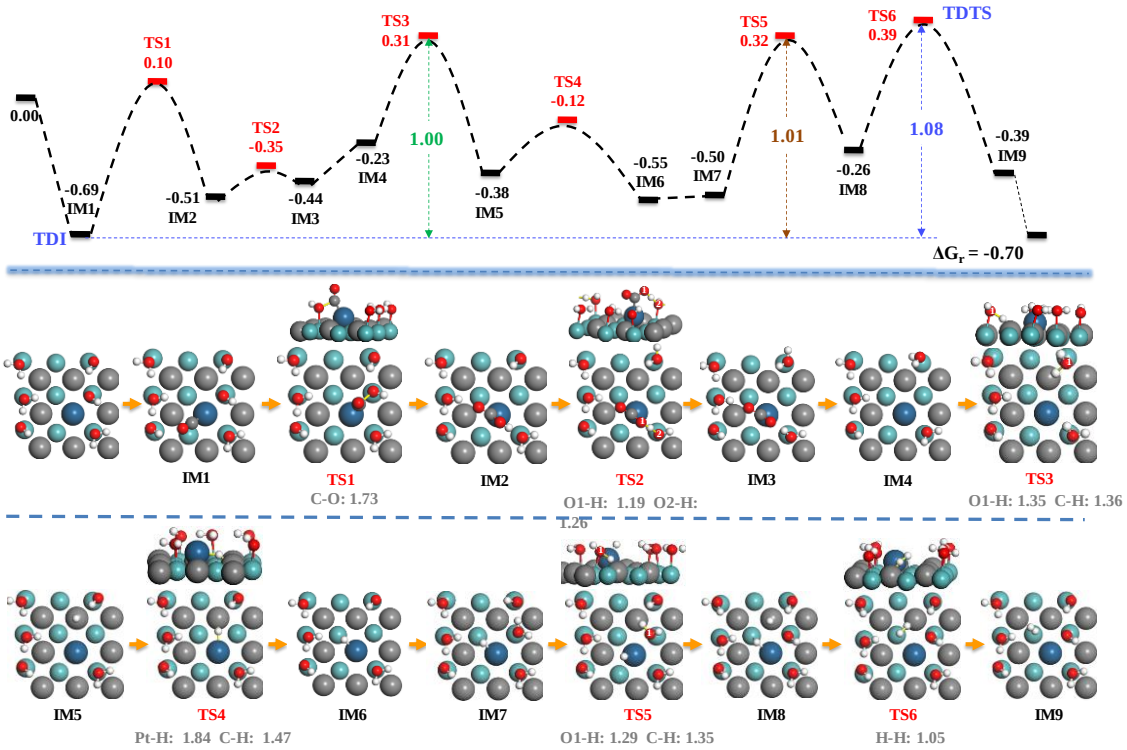

Figure 6.9 Free energy profile for the M_1-site pathway of associative route on the $Pt_1/(001)\text{-}(H_2O)_{3/8ML}(OH)_{3/8ML}$ surface phase.

The existence of multiple surface OH* facilitated the facile dehydrogenation of HO–CO* intermediate to CO_2 (TS2), the energy barrier of which was lower than that on the original (001) surface (0.16 *vs.* 0.46 eV in Figure 5.7). After the CO conversion to CO_2, the surface coverage of OH* was decreased, one was consumed in the HO–CO* formation, and the other transformed to H_2O during HO–CO* dehydrogenation. The subsequent steps consisted of the re-adsorption and activation of H_2O molecules (TS3 and TS5) to replenish the surface OH* groups as well as the migration and combination of H* atoms (TS4 and TS6) to produce H_2 molecules.

Due to the strong binding strength of the Pt site towards the CO molecule, the CO

adsorption state (IM1) was identified as the TDI. Due to the approximate energy positions of H_2O activation (TS3 and TS5) and H* combination (TS6), their energy differences based on IM1 as the reference point were close (1.00, 1.01 and 1.08 eV), which was also revealed by their non-zero X_{TOF} (0.07 for TS3, 0.11 for TS5 and 0.82 for TS6). The energetic span was chosen to be 1.08 eV (TS6 as the TDTS), larger than that of 0.83 eV *via* the Mo-site pathway (Figure 6.8).

6.3.2 The redox route

Similar to the situations of the associative route, two reaction pathways were considered in the redox route on the $Pt_1/(001)\text{-}(H_2O)_{3/8ML}(OH)_{3/8ML}(O)_{1/8ML}$ surface phase (Figure 6.4), where the CO oxidation occurred on the Mo site and Pt site were called Mo-site pathway and Pt-site pathway, respectively (Figure 6.10).

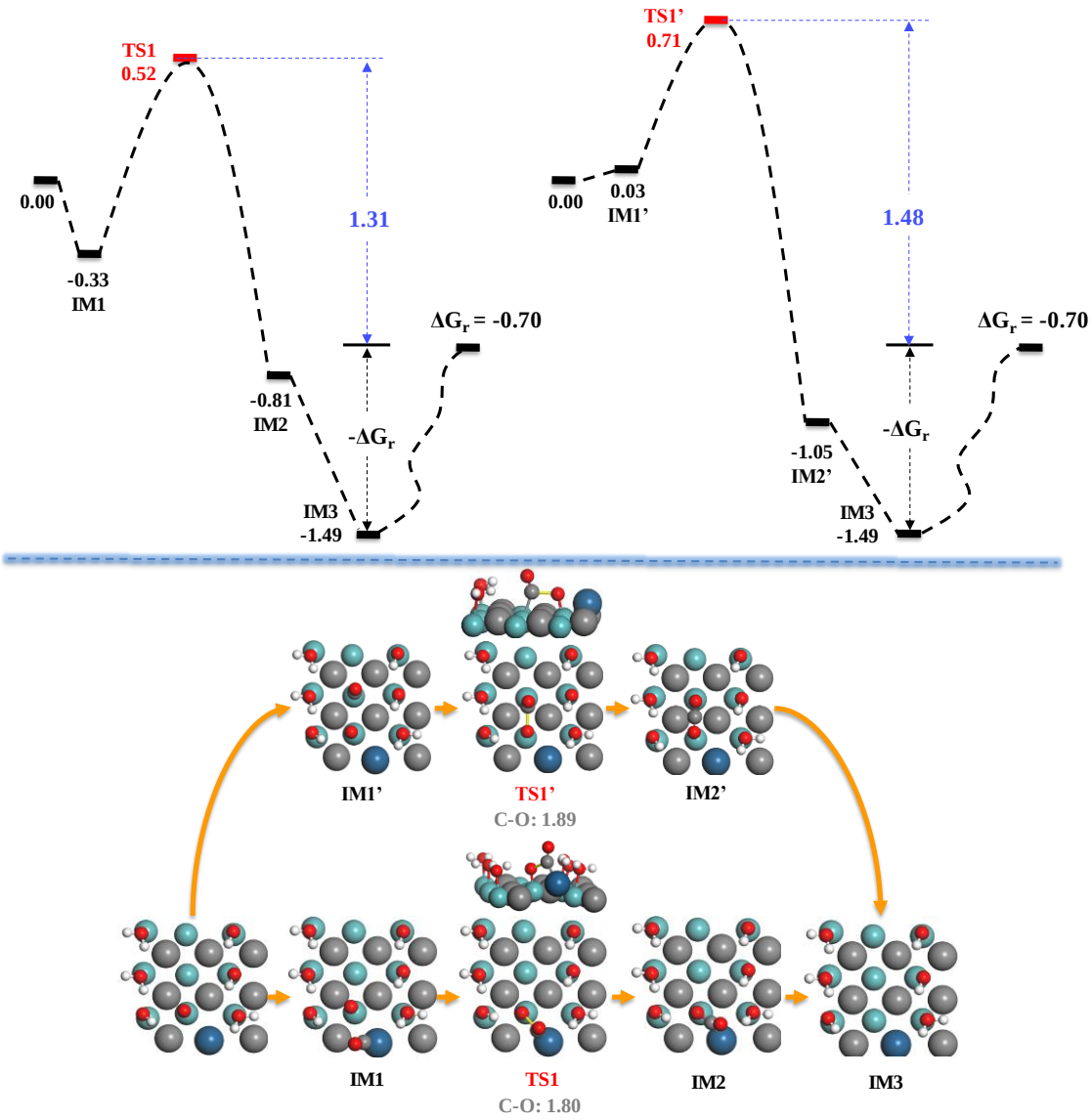

Figure 6.10 Part of free energy profile for the redox mechanism of Pt site (left) and Mo site (right) on the $Pt_1/(001)\text{-}(H_2O)_{3/8ML}(OH)_{3/8ML}(O)_{1/8ML}$ surface phase.

The Pt site had significantly stronger binding strength towards CO than the Mo site as indicated by a larger CO adsorption energy (−0.33 *vs.* 0.03 eV). The CO oxidation by the surface O* atom directly formed CO_2, the energy barriers of which were 0.85 (TS1) and 0.68 eV (TS1') on the Pt and Mo sites, respectively. The desorption of CO_2 in IM2 and IM2' resulted in the same surface structure as IM3. Thus, the subsequent surface O*

regeneration steps were the same (Figure 6.11).

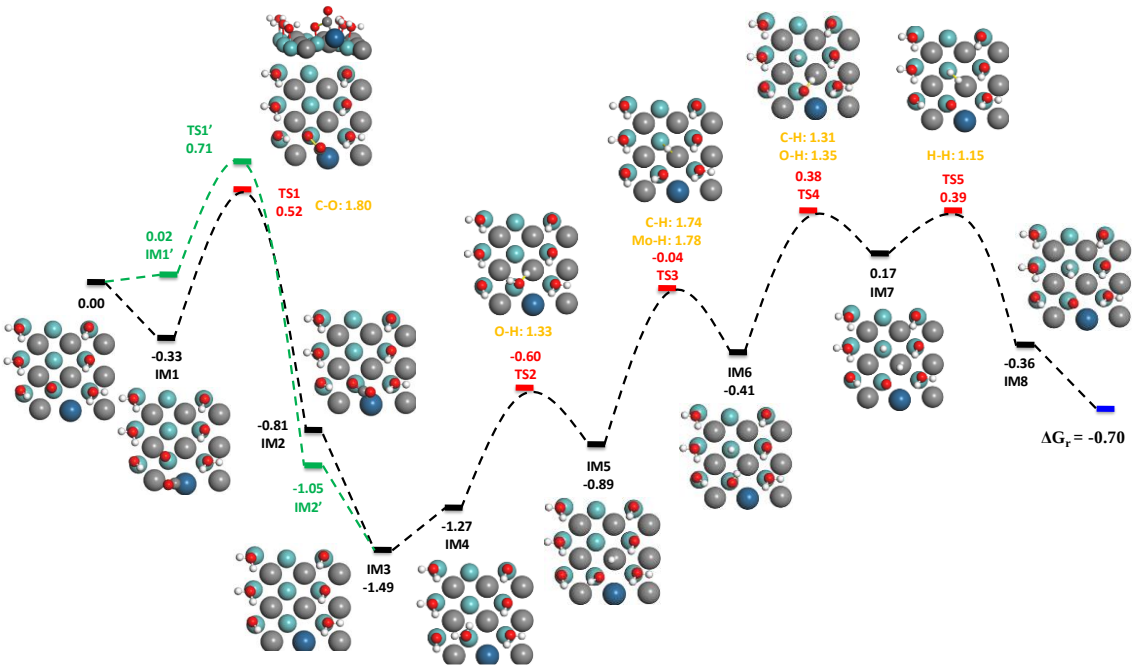

Figure 6.11 Free energy profile for the redox mechanism on the Pt_1/(001)-$(H_2O)_{3/8ML}(OH)_{3/8ML}(O)_{1/8ML}$ surface phase structures.

Based only on the CO oxidation step, the candidate energetic spans on the two reaction pathways were 1.31 and 1.48 eV, respectively (Figure 6.11), which were already significantly larger than those of the associative route (0.83 and 1.08 eV). The final energetic span based on the whole catalytic cycle should be no less than 1.30 eV, showing that the redox route on the (001) surface was much unfavourable.

6.4 Discussion of WGS on the evolved Pt_1/fcc MoC surface

The original Pt_1/(111)-Mo surface would quickly evolve to the Mo–OH layer phase (Figure 6.1) under the WGS atmosphere [108], and the surface OH* was the key reactive group fostering the associative route. The TOFs of the associative route on the Mo–OH

layer phase (Figure 6.5, 6.71×10^{-1} h^{-1}) showed a marginal increase compared with that on the original surface (Figure 5.3, 1.18×10^{-1} h^{-1}) and was still obviously lower than the redox route on the original Pt_1/(111)-Mo surface (Figure 5.4, 4.87×10^{1} h^{-1}). The Mo–OH layer phase was unstable and would gradually dehydrogenate to form the thermodynamically more stable Mo–O monolayer phase [108] (Figure 6.2), which was more suitable for the redox route (Figure 6.6) and the H_2O-assisted associative route (Figure 6.7). For the redox route on the original surface and the Mo–O monolayer phase, the TDTS and TDI were always the transition state and reactant of the CO oxidation step, respectively. Thus, the energy barrier of the CO oxidation step equalled to the energetic span (δE) of the whole catalytic cycle, and it decreased when the original surface evolved to Mo–O monolayer phase (1.25 vs. 1.04 eV, Figures 5.4 and 6.6).

Table 6.1 compares the TOF values and TOF-determining states of various WGS routes on original Pt doped (111)-Mo and (001) surfaces, and in this table, different routes are replaced by abbreviations, A for the associative route, R for the redox route and WA for H_2O-assisted associative route.

Table 6.1 TOF values and TOF-determining states of various WGS routes on evolved Pt doped (111)-Mo and (001) surfaces.

Surface Phase	Route	TOF (h^{-1})	TDI (figure no., label)	TDTS (figure no., label)
$Pt_1/(111)\text{-}Mo(OH)_{3/4ML}$	A	6.71×10^{-1}	CO adsorption (Fig. 6.5, IM1)	H_2O activation (Fig. 6.5, TS2)
$Pt_1/(111)\text{-}Mo(OH)_{1ML}$	R	1.21×10^{4}	CO adsorption (Fig. 6.6, IM1)	CO oxidation (Fig. 6.6, TS1)
$Pt_1/(111)\text{-}Mo(OH)_{1ML}$	WA	1.03×10^{5}	CO adsorption (Fig. 6.7, IM1)	HO–CO* formation (Fig. 6.7, TS1)
$Pt_1/(001)\text{-}(H_2O)_{3/8ML}(OH)_{3/8ML}$	A(Mo-site)	1.91×10^{6}	gas phase CO and H_2O (Fig. 6.8)	HO–CO* formation (Fig. 6.8, TS1)
$Pt_1/(001)\text{-}(H_2O)_{3/8ML}(OH)_{3/8ML}$	A(Pt-site)	3.12×10^{3}	CO adsorption (Fig. 6.9, IM1)	H_2 formation [a] (Fig. 6.9, TS6)
$Pt_1/(001)\text{-}(H_2O)_{3/8ML}(OH)_{3/8ML}(O)_{1/8ML}$	R(Mo-site)	$\leq7.48\times10^{-2}$	—	—
$Pt_1/(001)\text{-}(H_2O)_{3/8ML}(OH)_{3/8ML}(O)_{1/8ML}$	R(Pt-site)	≤7.92	—	—

Consequently, the TOF of the redox route on the Mo–O monolayer phase increased by about 3 orders of magnitudes compared with the original surface (1.21×10^{4} *vs.* 4.87×10^{1} h^{-1}, Table 6.1). The accelerated TOF of the redox route on the Mo–O monolayer was attributed to the weakened surface binding strength of O* atoms, which decreased by about 24% with O* coverage increasing from 1/9 ML to 1ML on the (111)-Mo surface [108], thus facilitating its easier detachment from the surface in the CO oxidation step. The TOF of the H_2O-assisted associative route increased sharply by about 7 orders of magnitudes when the original Pt_1/(111)-Mo surface phase evolved to the Mo-O monolayer surface phase (3.21×10^{-2} *vs.* 1.03×10^{5} h^{-1}, Table 6.1). The TDI was always the CO adsorption state on the two surfaces, while the TDTS changed from the HO–CO* dehydrogenation state on the original surface (Figure 5.5, TS2) to the HO–CO* formation state on the Mo–O monolayer phase (Figure 6.7, TS1). The δE on Mo–O monolayer phase reduced by 0.54 eV compared with that on the original surface, where the HO–CO* formation step contributed 0.18 eV to the δE reduction and the HO–CO* dehydrogenation contributed the remaining 0.36 eV to the δE reduction. The increased reactivity of O* atoms on the Mo–O monolayer facilitated the HO–CO* intermediate formation (Figure 6.7, TS1), while the H transfer between both O atoms in the HO–CO* dehydrogenation step on the Mo–O monolayer (Figure 6.7, TS2) was much efficient than that between the O and Mo site on the original surface (Figure 5.5, TS2).

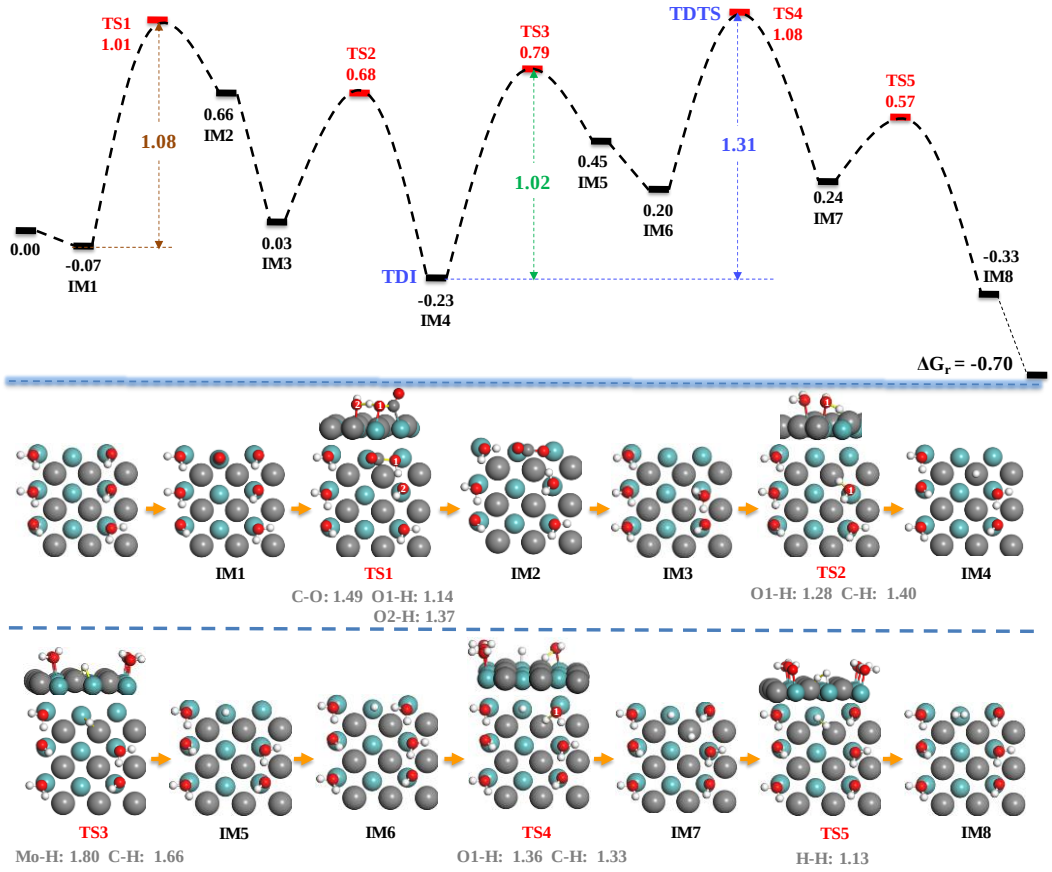

Figure 6.12 Free energy profile for the associative mechanism on the MoC (001)-$(H_2O)_{3/8ML}(OH)_{3/8ML}$ surface phase structures without Pt doping.

The surface phase diagram showed that the original MoC (001) surface would evolve to the surface phase constituted of OH* groups and H_2O molecules at most WGS atmosphere conditions as described in the previous Chapter. The increased coverage of surface OH* facilitated the dehydrogenation of HO–CO* intermediate in the associative route, the energy barriers of which decreased from 0.41 eV (Mo-site pathway, TS3 in Figure 5.6) and 0.46 eV (M_1-site pathway, TS3 in Figure 5.7) to 0.01 eV (TS2 in Figure 6.8) and 0.16 eV (TS2 in Figure 6.9), respectively. Correspondingly, the TDTS of the associative routes changed from the HO–CO* dehydrogenation on the original (001)

surface (Figures 5.6 and 5.7) to HO–CO* formation (Figure 6.8) or the H_2 formation (Figure 6.9). Both the original and the evolved (001) surfaces showed high TOFs of the associative route (Table 5.1 and 6.1). It should be noted here that the TOF of the (001) surface without Pt-doping was only 2.43×10^{-3} h^{-1} (Figure 6.12), which was significantly lower than that of 1.91×10^{6} h^{-1} (Table 5.1) on the corresponding (001) surface with Pt-doping, showing the necessary involvement of noble metal atom for high catalytic efficiency. Besides the OH* groups, the surface O* atoms were also predicted to have a certain probability of emerging on the (001) surface at the WGS reaction condition [179]. Thus, the redox route was also considered on an H_2O/OH/O mixed adsorbing surface phase structure (Figures 6.11 and 6.40). Based only on the CO oxidation step and the rule of energetic span definition, the actual energetic spans were predicted to be no less than 1.30 eV, which was much higher than those of the associative routes (Table 6.1). The TOFs of the redox route on the (001) surface were several orders of magnitudes lower than those of associative routes Table 6.1), signifying that the redox route played a minor role in the WGS reaction compared with the associative route. The calculations by Illas *et al.* [112] also showed that the associative route was actually the predominant mechanism on the Au_4/fcc MoC (001) surface, and the surface O* only occupied a minor proportion of species on the (001) surface.

6.5 Summary

Based on the simulation conditions of the previous chapter, this chapter investigated the water-gas shift reaction on the evolved surface of Pt_1/fcc MoC, considering the effects of

different predominant crystal facets and different reaction routes by DFT and ESM.

For the evolved (111)-Mo surfaces, the H_2O-assisted associative route (1.03×10^5 h^{-1}) showed the best reactivity due to surface phase evolution to the Mo–O monolayer phase. This phase structure evolution also significantly increased the TOF of the redox route (1.21×10^4 h^{-1}) compared to the original surface (4.87×10^1 h^{-1}). The associative route is always kept at relatively low TOF values during the evolutions of surface phase structures.

For the evolved (001) surfaces, the associative routes *via* the Mo-site or the Pt-site pathways consistently showed significant TOFs, whereas the redox route showed much lower TOFs, signifying its minor role in the WGS reaction. Notably, the associative routes *via* the Mo-site pathway (1.91×10^6 h^{-1}) displayed an obviously increase in the TOF compared to the original surface (6.21×10^2 h^{-1}), even higher than the Pt-site pathway (3.12×10^3 h^{-1}).

In summary, the original (111)-Mo surface cannot compete with the original or the evolved (001) surfaces in the WGS reaction. However, with the original (111)-Mo surface evolved to the thermodynamically more stable Mo–O monolayer phase, catalytic efficiencies of the redox route and the H_2O-assisted associative route could increase sharply to a level comparable with those of (001) surfaces. Thus, the (111)-Mo and (001) surfaces contributed comparably to the WGS reactions *via* different surface phase structures and routes.

Chapter 7 Conclusions and Further Research

7.1 Summary of the main conclusions

The fcc MoC decorated with highly dispersed Pt showed high reactivity in the low-temperature WGS reactions. It is significant to explore and clarify the origin of its high performance. Although many experiments have been reported recently for this type of catalyst, it is important to explore and elucidate the source of the high activity. The two active facets (111)-Mo and (001) of fcc MoC undergo evolutions of the surface phase structure in the realistic water-gas shift reaction atmosphere, *i.e.*, the H_2/H_2O mixtures, and thus exhibit different physicochemical properties. This work provided insights from first-principles methods on the low-temperature water-gas shift reaction with Pt_1/fcc MoC.

As a wrap-up, the following conclusions can be drawn:

(1) The species, including OH*, O*, and H*, were all readily formed on the (001) surface according to the reaction rate constants, but the comprehensive investigation showed that the H_2O*, OH*, and O* species tended to cover the (001) surface instead of H*, justifying the importance of the evolved surface in the water-gas shift reaction.

(2) Disregarding the evolution of the surface phase structure, the WGS reaction on the Pt_1/(111)-Mo surface occurred mainly through the redox mechanism, whereas on the Pt_1/(001) surface it occurred mainly through the associative mechanism on Pt site, and Pt_1/(001) was significantly more efficient than Pt_1/(111)-Mo by comparing the predicted TOFs (1.95×10^5 h^{-1} *vs.* 4.87×10^1 h^{-1}).

(3) Considering the evolution of the surface phase structure, the predicted results for the WGS reaction were quite different. The Mo–O monolayer phase on the (111)-Mo surface enabled redox and H_2O-assisted associative mechanisms to predominate, with TOFs of 1.21×10^4 h^{-1} and 1.03×10^5 h^{-1}, respectively. Whereas on the (001) surface, the associative mechanism still predominated, but the Mo site showed very promising activity (1.91×10^6 h^{-1}) compared to the Pt site (3.12×10^3 h^{-1}).

(4) From a macro perspective, the original (111)-Mo surface cannot compete with the original or the evolved (001) surfaces in the WGS reaction. However, with the original (111)-Mo surface evolved to the thermodynamically more stable Mo–O monolayer phase, catalytic efficiencies of the redox route and the H_2O-assisted associative route could increase sharply to a level comparable with those of (001) surfaces. Thus, the (111)-Mo and (001) surfaces exhibit similar catalytic efficiencies for the WGS reaction, although through different surface phase structures and pathways.

7.2 Recommendations for the future works

Although some interesting results have been discovered and discussed in this thesis, several works are still worth further studying. They are listed as follows:

- In this thesis, the (001) and (111)-Mo crystal facets were considered separately. However, when fcc MoC crystals are prepared in practice, both facets would coexist [91]. Further studies on the reaction mechanism under mixed crystalline facets should

also be considered, in combining with the already reported experimental results of structural characterisation.

- As can be seen from the results of this thesis, the Pt atom loaded on the surface changed the reaction route obviously. As a computational study, based on the framework in this thesis, other possible dispersed metal atoms (*e.g.,* Au, Ir, etc.) should be more comprehensively considered so that more systematic insights can be obtained. This would provide not only the interpretable information about the M_1/fcc MoC catalysts already prepared, but also the opportunity to accelerate the development of more efficient catalysts for low-temperature water-gas shift reactions.

- The specific temperatures used in this thesis for the analysis of the surface phase structure and the kinetic studies were used to be able to better validate with published experiments. In addition to performing the analyses, further consideration of the effects of variations in temperature is something that could be done in the future.

Supplementary Information A: Figures

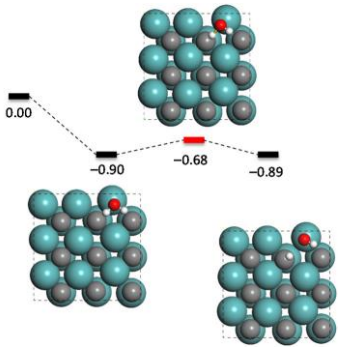

(1)

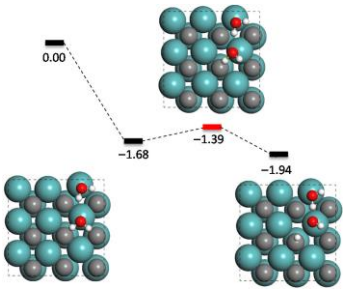

(2-a)

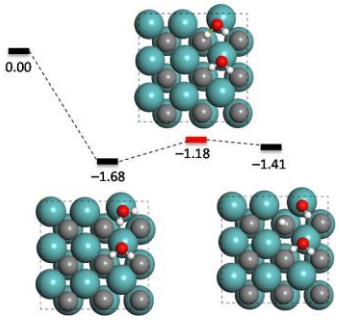

(2-b)

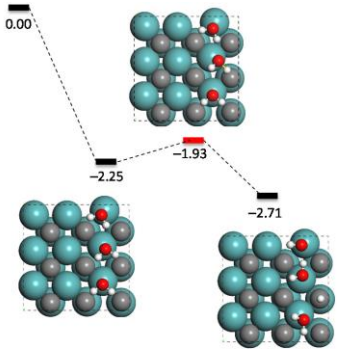

(3-a)

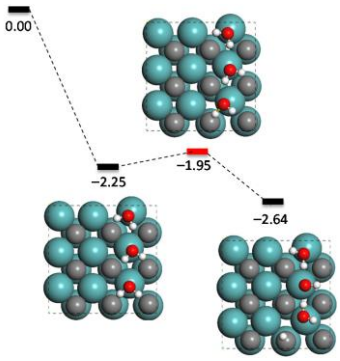

(3-b)

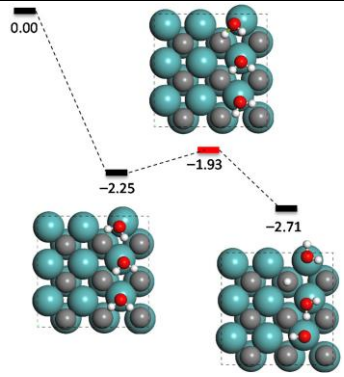

(3-c)

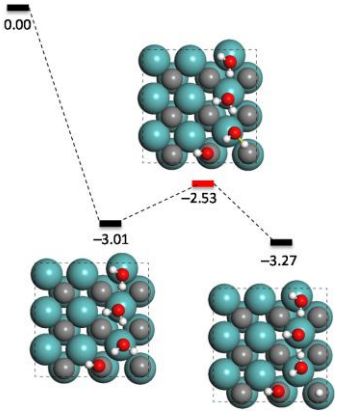

(4-a)

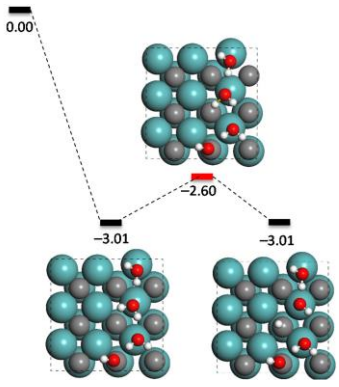

(4-b)

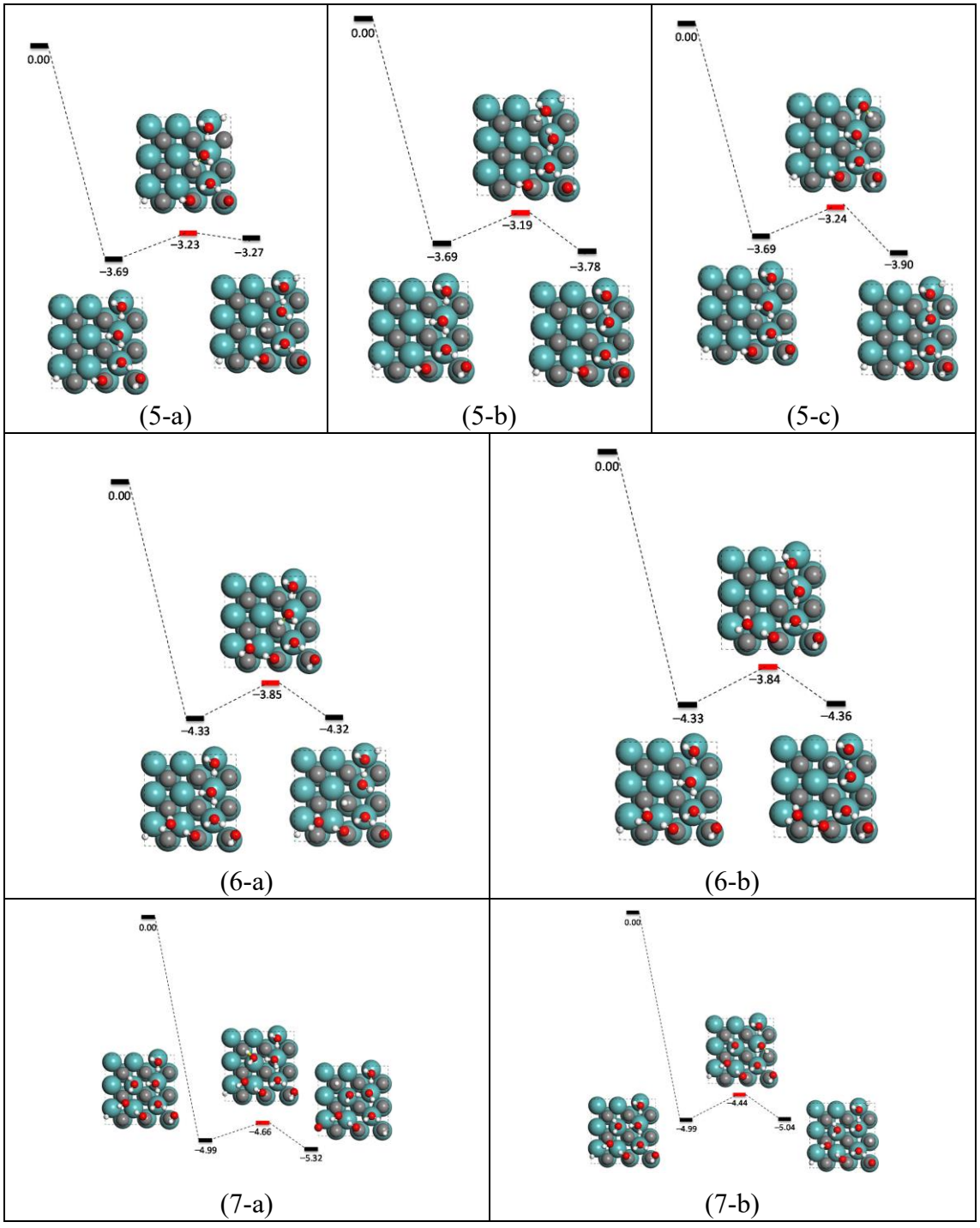

(5-a) (5-b) (5-c)

(6-a) (6-b)

(7-a) (7-b)

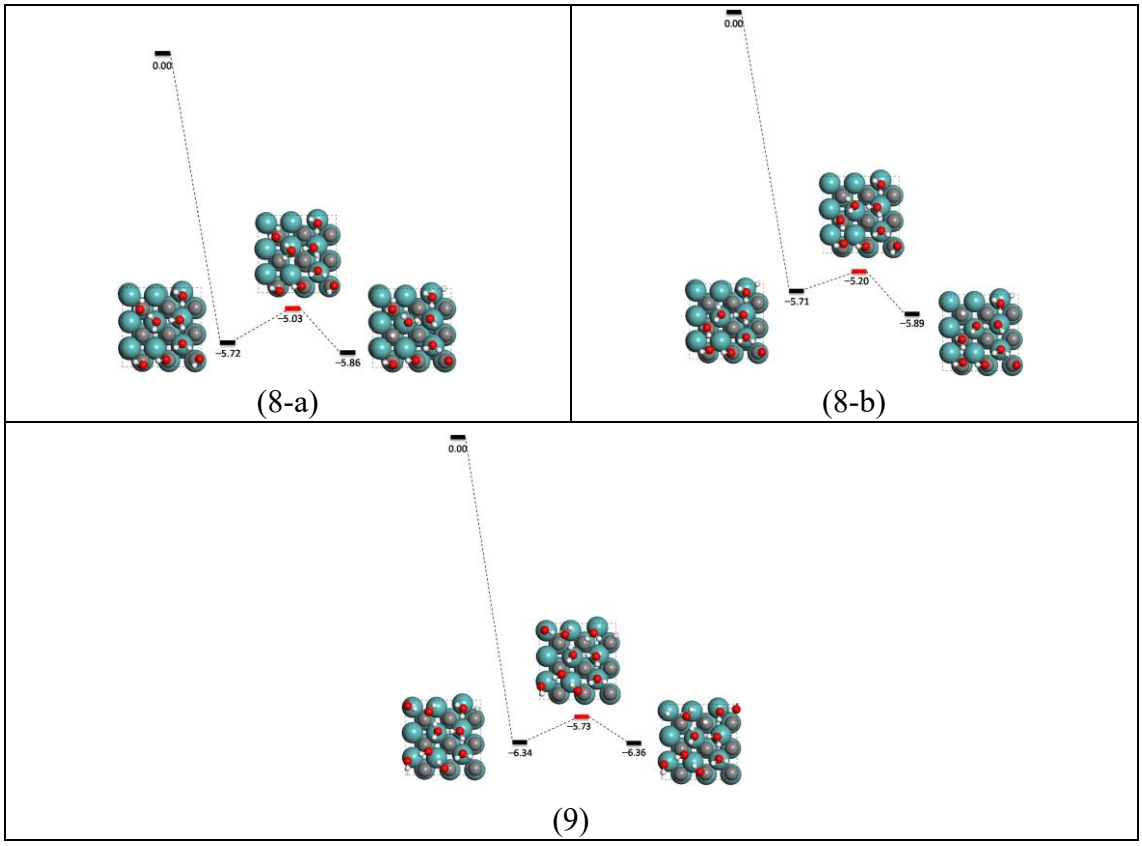

Figure S1 The potential energy profiles with zero-point energy correction for the H_2O^* dissociation considering the coverage of H_2O^*.

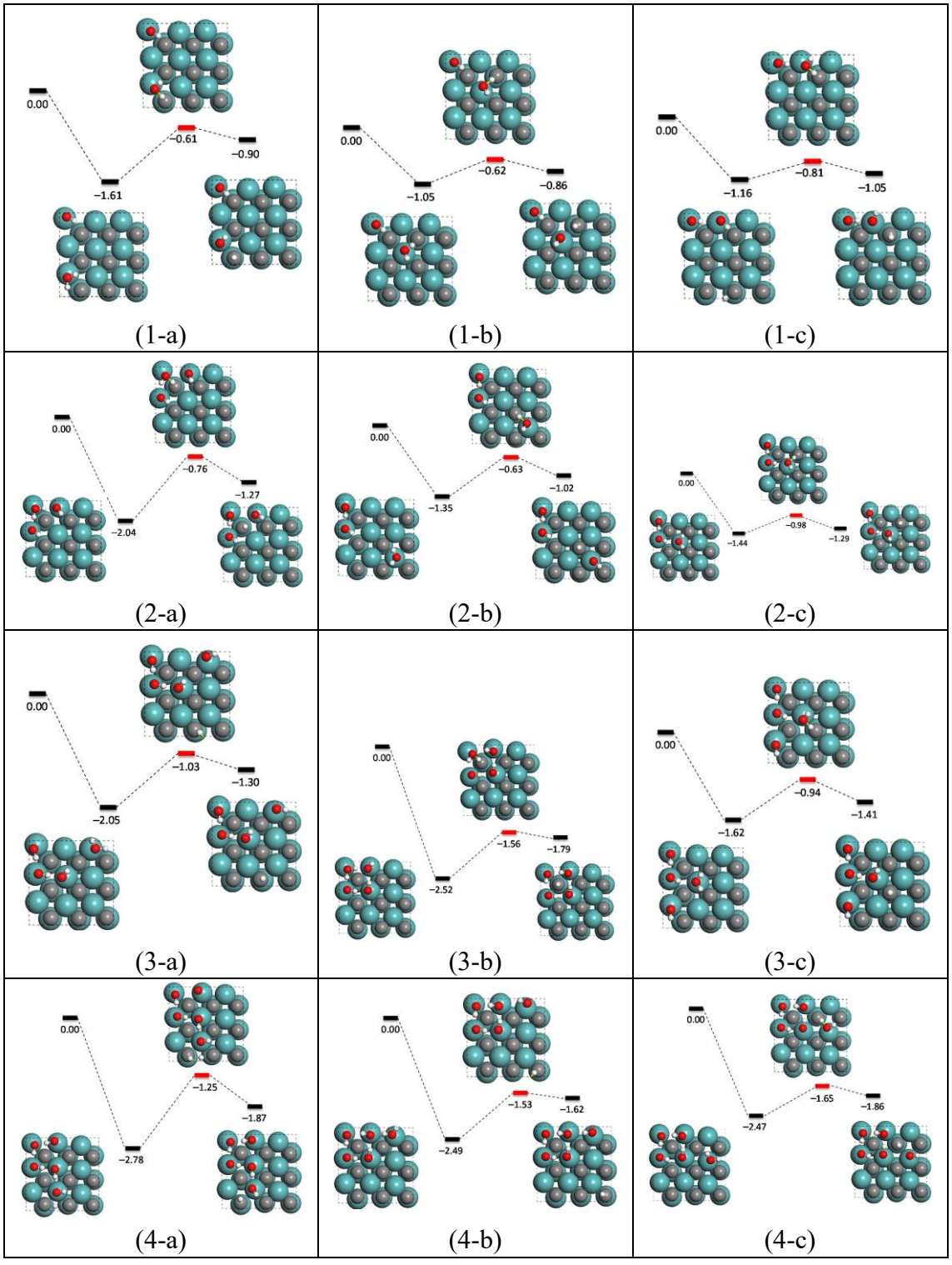
0.00
−0.61
−0.90
−1.61
(1-a)
0.00
−0.62
−0.86
−1.05
(1-b)
0.00
−0.81
−1.05
−1.16
(1-c)
0.00
−0.76
−1.27
−2.04
(2-a)
0.00
−0.63
−1.02
−1.35
(2-b)
0.00
−0.98
−1.29
−1.44
(2-c)
0.00
−1.03
−1.30
−2.05
(3-a)
0.00
−1.56
−1.79
−2.52
(3-b)
0.00
−0.94
−1.41
−1.62
(3-c)
0.00
−1.25
−1.87
−2.78
(4-a)
0.00
−1.53
−1.62
−2.49
(4-b)
0.00
−1.65
−1.86
−2.47
(4-c)

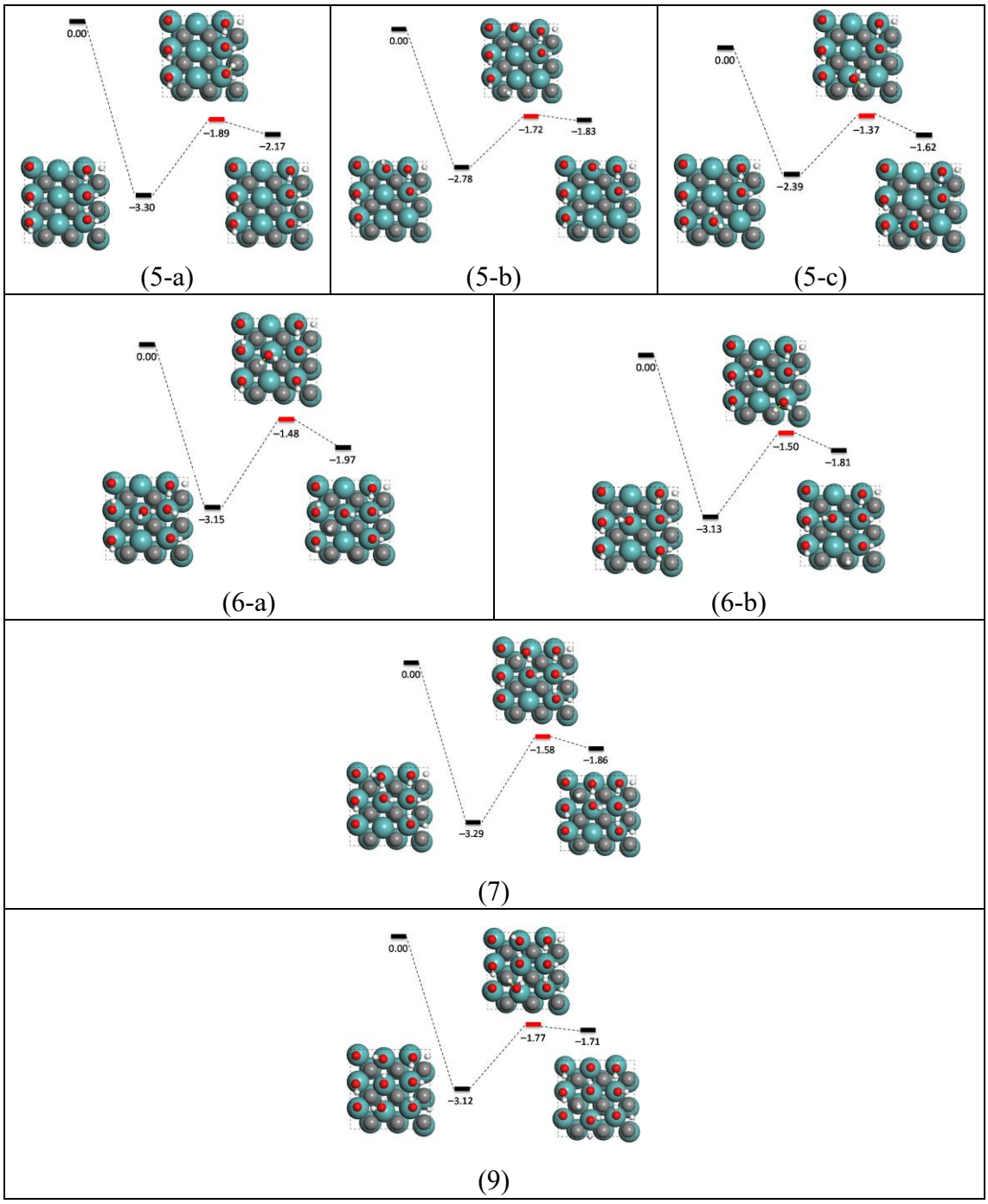

Figure S2 The potential energy profiles with zero-point energy correction for the H_2O^* dissociation considering the coverage of OH*.

(a)

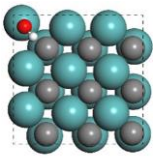

(1)
0.40 eV

(b)

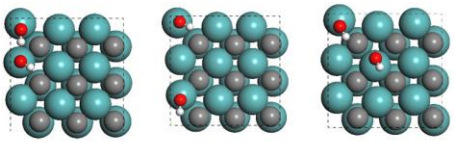

(1) −0.78 eV | (2) −0.74 eV | (3) −0.46 eV

(c)

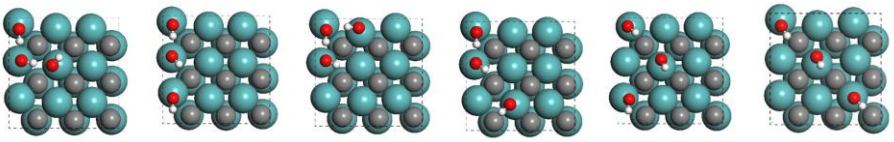

(1) −0.89 eV | (2) −0.89 eV | (3) −0.83 eV | (4) −0.72 eV | (5) −0.51 eV | (6) −0.32 eV

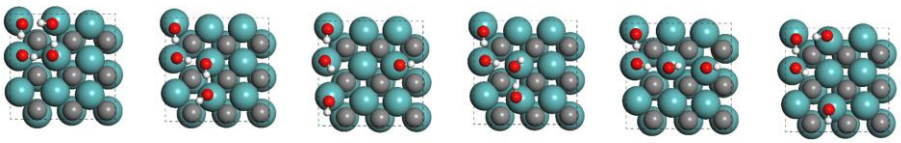

(1) −1.31 eV | (2) −1.03 eV | (3) −0.98 eV | (4) −0.97 eV | (5) −0.96 eV | (6) −0.96 eV

(d)

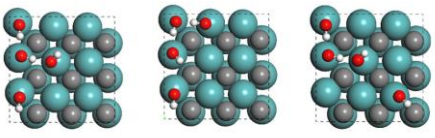

(7) −0.93 eV | (8) −0.88 eV | (9) −0.61 eV

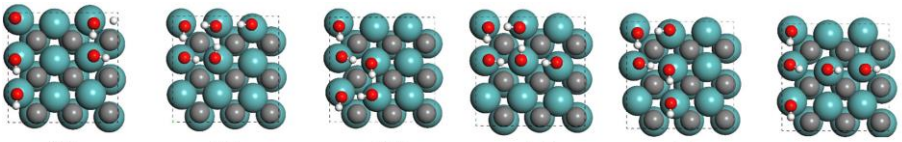

(1) −1.48 eV | (2) −1.26 eV | (3) −1.23 eV | (4) −1.17 eV | (5) −1.16 eV | (6) −1.05 eV

(e)

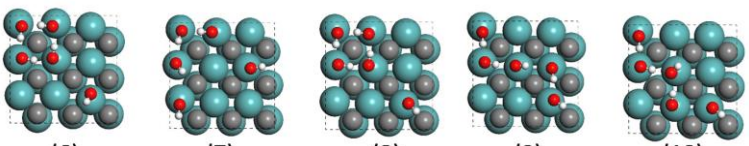

(6) −0.96 eV | (7) −0.94 eV | (8) −0.79 eV | (9) −0.74 eV | (10) −0.70 eV

(f)

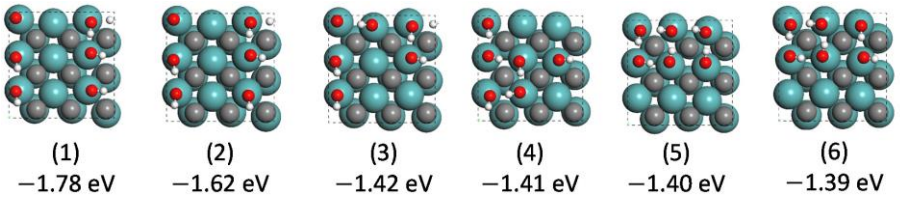
(1)
−1.78 eV
(2)
−1.62 eV
(3)
−1.42 eV
(4)
−1.41 eV
(5)
−1.40 eV
(6)
−1.39 eV

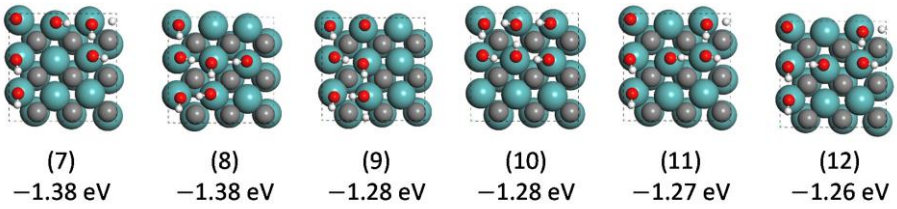
(7)
−1.38 eV
(8)
−1.38 eV
(9)
−1.28 eV
(10)
−1.28 eV
(11)
−1.27 eV
(12)
−1.26 eV

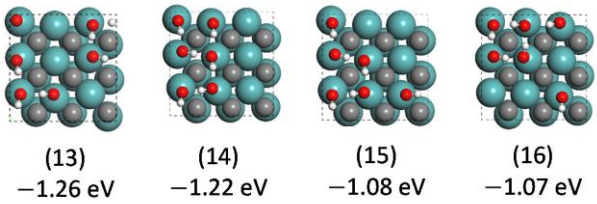
(13)
−1.26 eV
(14)
−1.22 eV
(15)
−1.08 eV
(16)
−1.07 eV

(g)

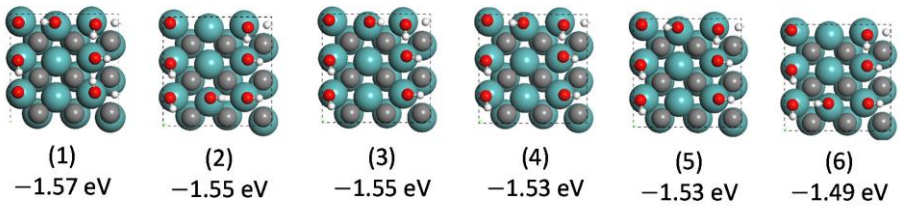
(1)
−1.57 eV
(2)
−1.55 eV
(3)
−1.55 eV
(4)
−1.53 eV
(5)
−1.53 eV
(6)
−1.49 eV

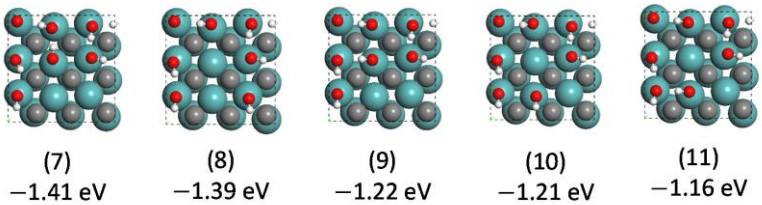
(7)
−1.41 eV
(8)
−1.39 eV
(9)
−1.22 eV
(10)
−1.21 eV
(11)
−1.16 eV

(h)

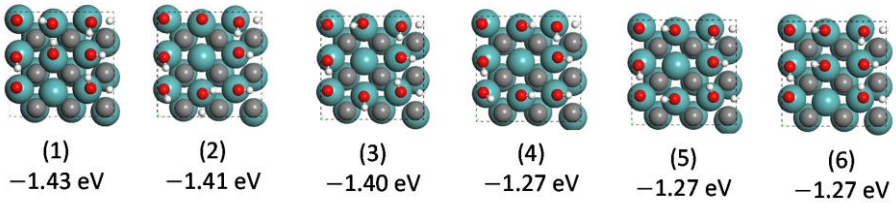
(1)
−1.43 eV
(2)
−1.41 eV
(3)
−1.40 eV
(4)
−1.27 eV
(5)
−1.27 eV
(6)
−1.27 eV

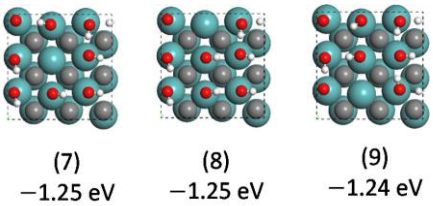
(7)
−1.25 eV
(8)
−1.25 eV
(9)
−1.24 eV

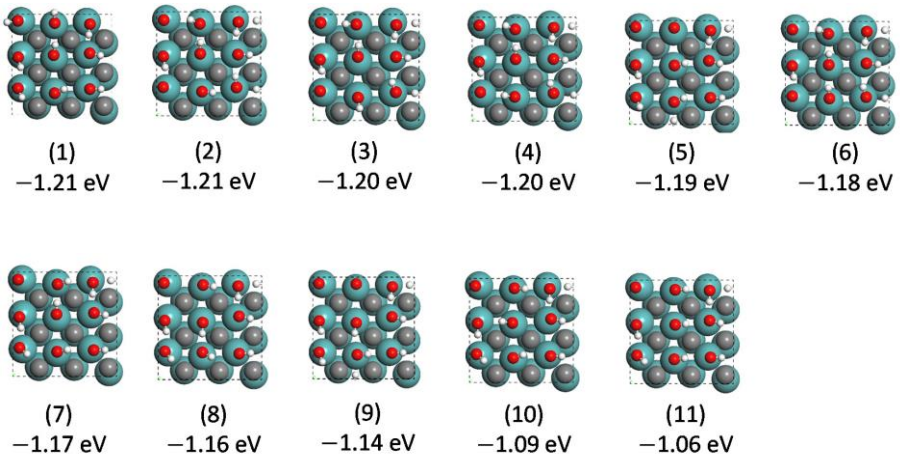

Figure S3 Configurations of OH* coverages from 1/9 to 1 ML ((a) to (i)) and surface binding energy without zero-point energy correction.

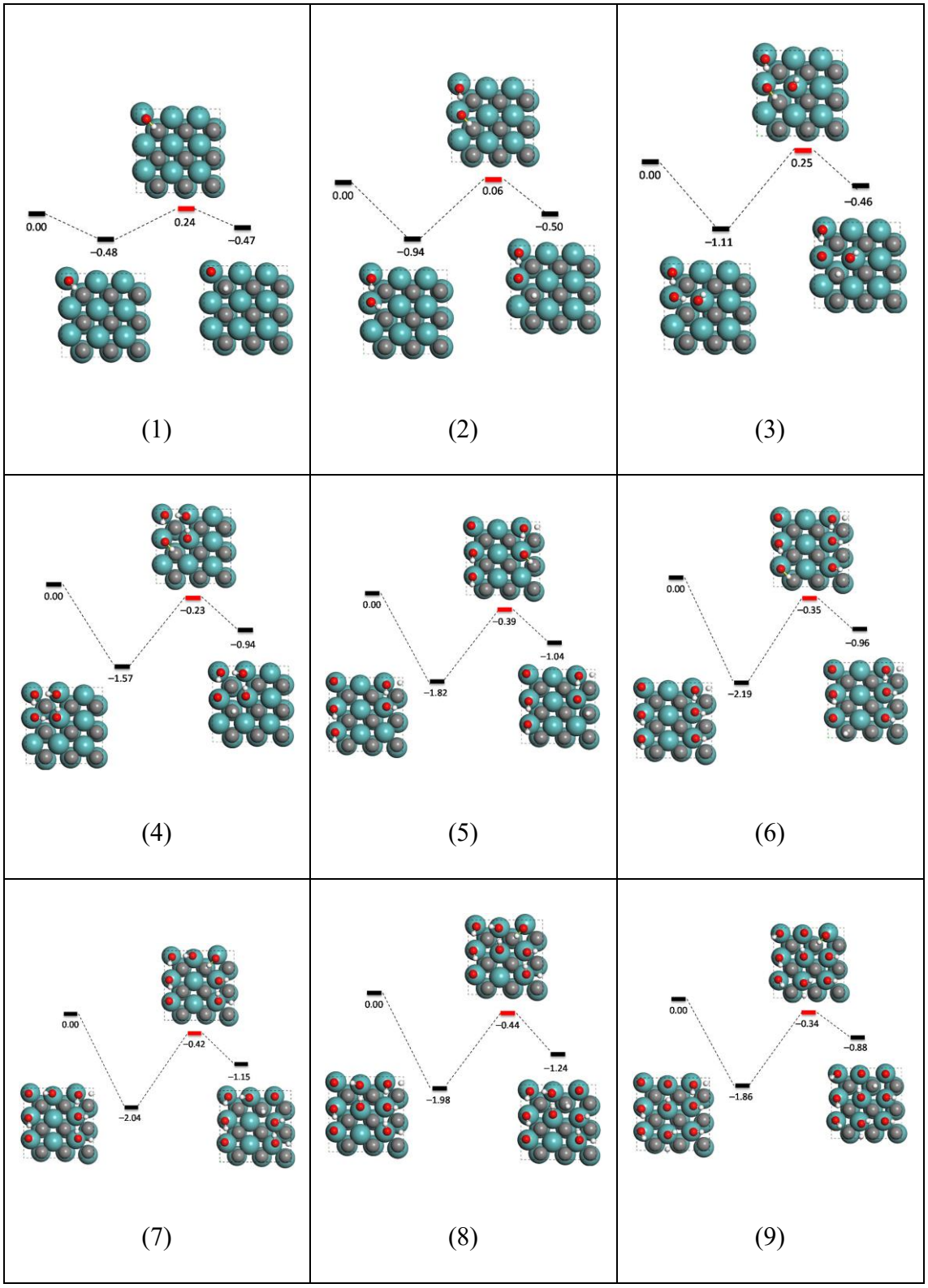

Figure S4 The potential energy profiles with zero-point energy correction for direct deprotonation of single OH* considering the coverage of OH*.

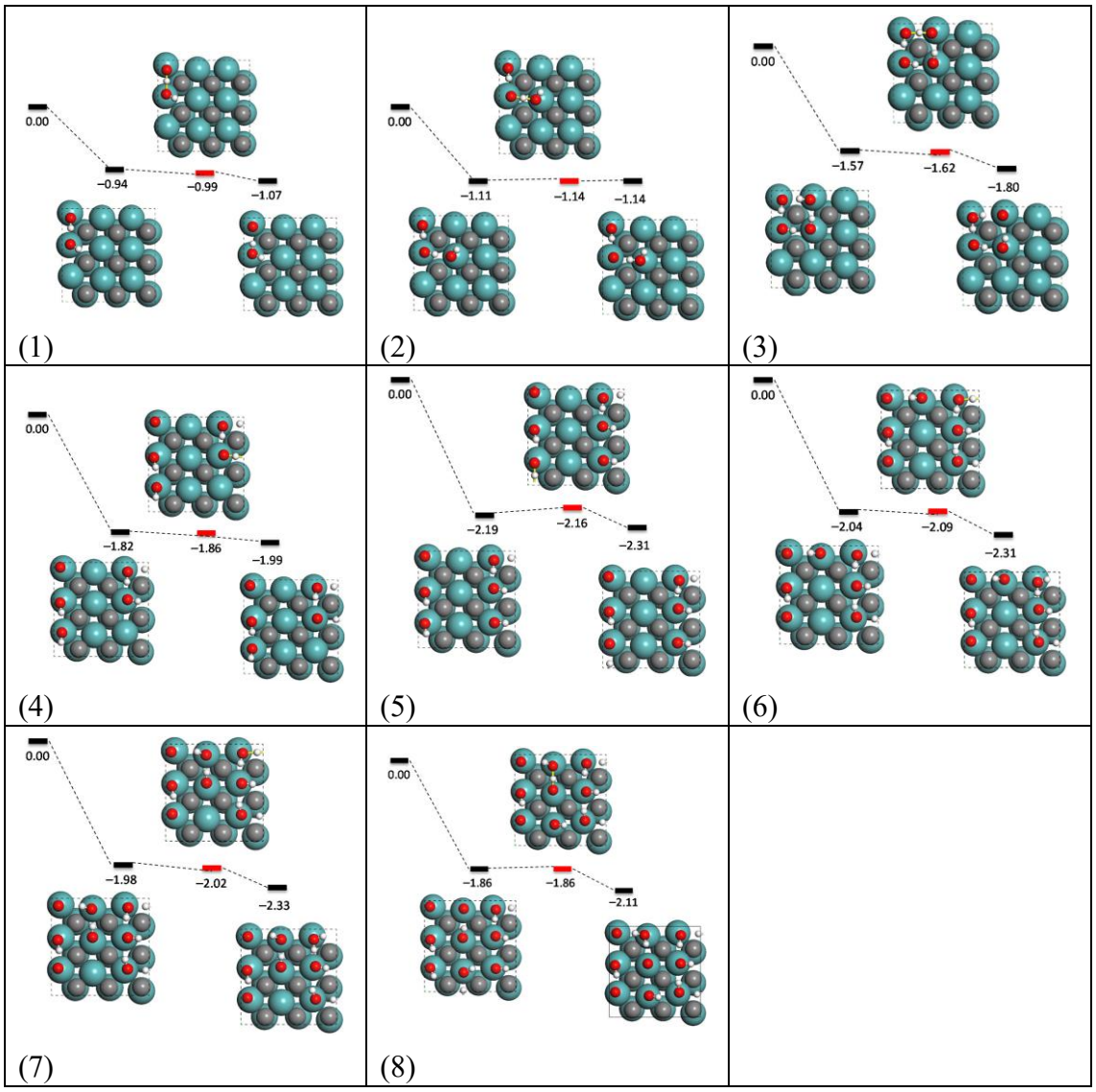

Figure S5 The potential energy profiles with zero-point energy correction for hydroxyls disproportionation considering the coverage of OH*.

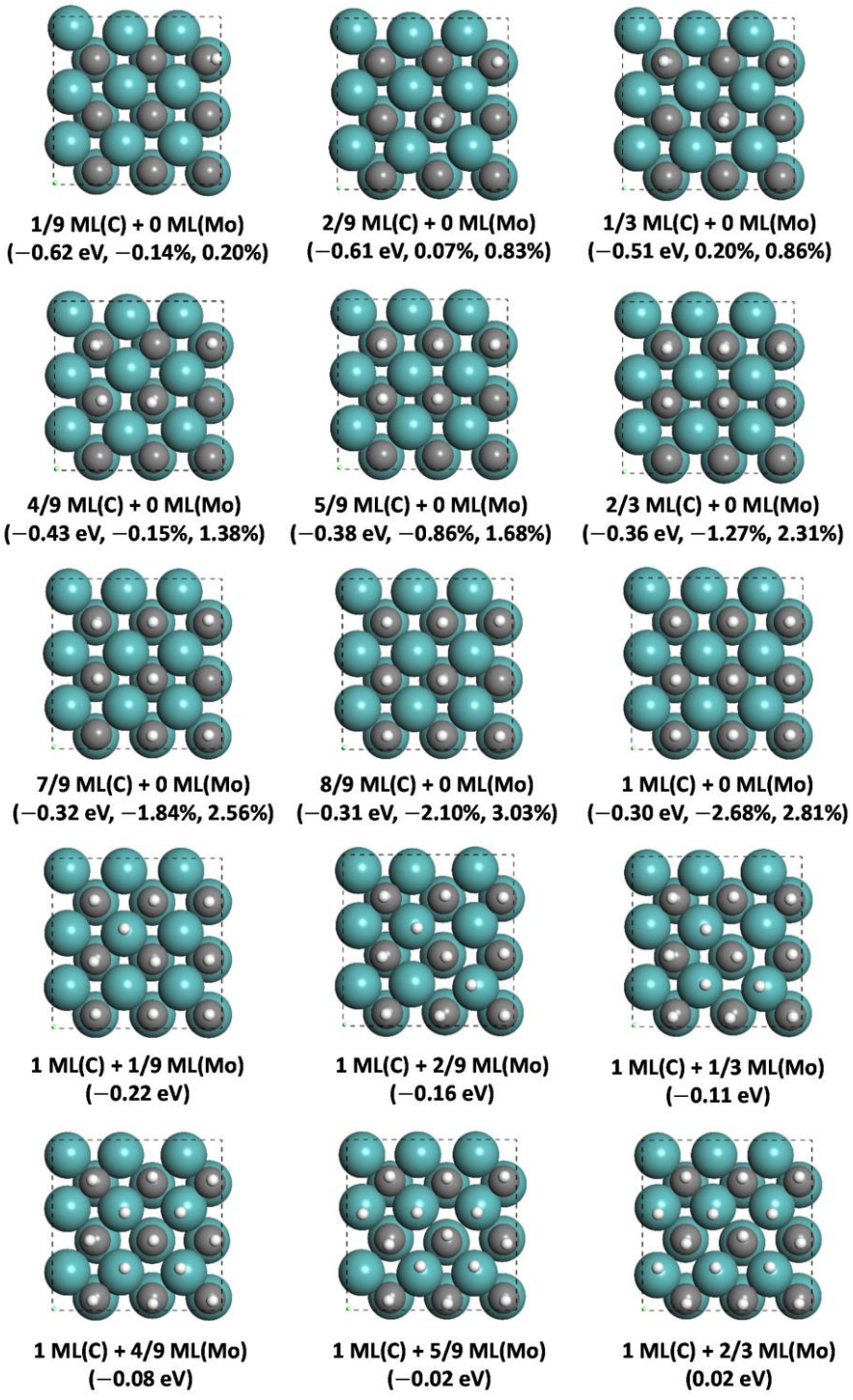

Figure S6 Configurations of H* species on fcc MoC (001) surface.

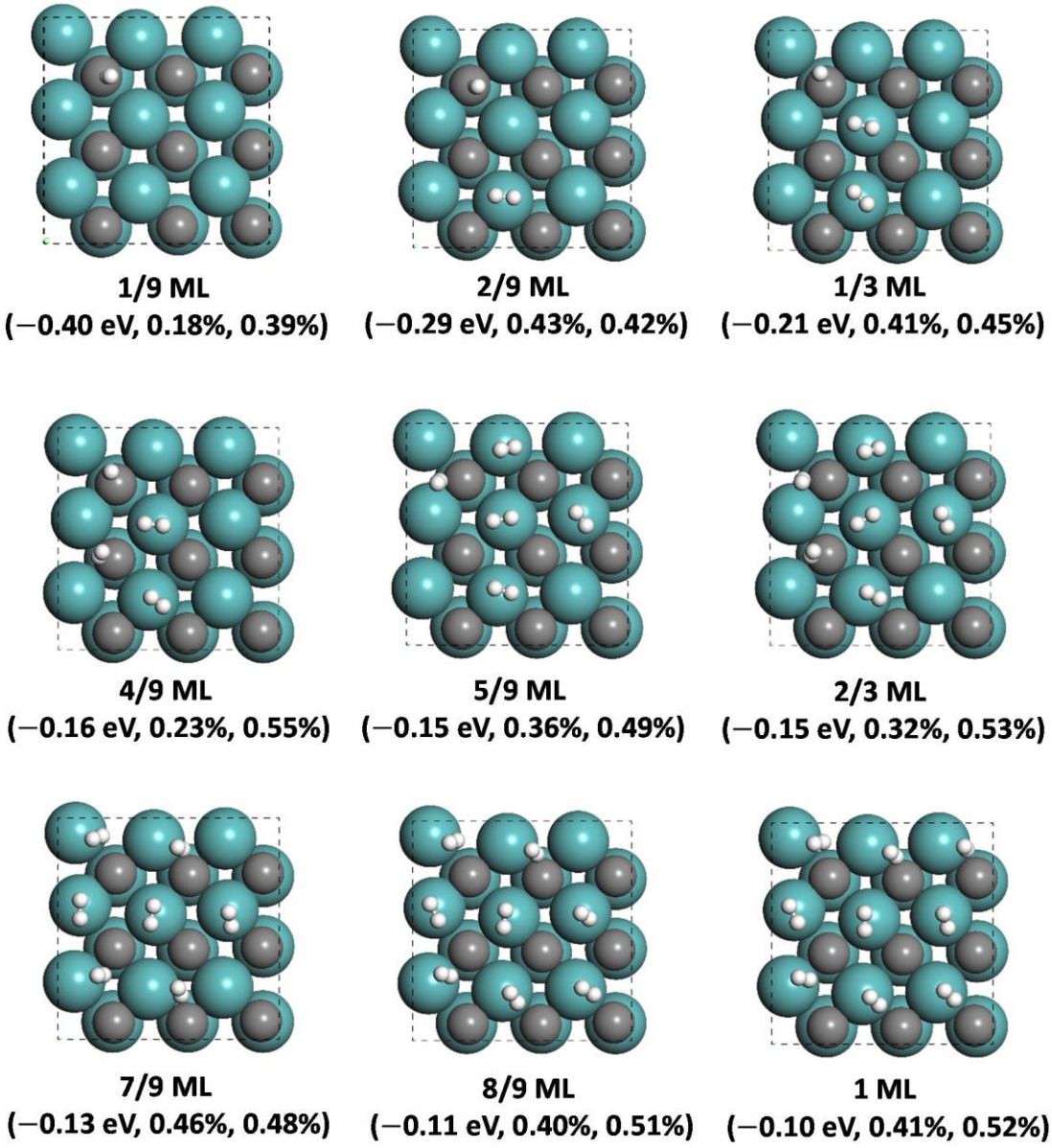

Figure S7 Configurations of H_2 adsorption coverage on fcc MoC (001) surface.

Supplementary Information B: Tables

Table S1 Energetic aspects of surface H_2O^* dissociation with *n* adsorbing H_2O^*.

	$n\ H_2O^* \rightarrow (n-1)\ H_2O^* + OH^* + H^*$						
n	$\Delta E^{\neq}_{TS,ZPE}$	$\Delta E^{\neq}_{TS}$	$\Delta E_{r,ZPE}$	ΔE_r	δ^i_{TS}	$d^{\neq}_{O\cdots H}$	$d^{\neq}_{C\cdots H}$
1	0.22	0.38	0.01	0.07	1167	1.313	1.335
2-a	0.30	0.42	−0.26	−0.20	1291	1.257	1.416
2-b	0.50	0.65	0.28	0.34	1002	1.385	1.290
3-a	0.32	0.45	−0.46	−0.44	1291	1.317	1.373
3-b	0.30	0.43	−0.39	−0.37	1296	1.297	1.390
3-c	0.32	0.46	−0.47	−0.45	1269	1.369	1.321
4-a	0.48	0.64	−0.26	−0.23	1286	1.357	1.350
4-b	0.41	0.55	0.00	0.09	1239	1.351	1.348
5-a	0.46	0.61	−0.08	0.01	1257	1.354	1.351
5-b	0.50	0.67	−0.10	−0.02	1203	1.284	1.372
5-c	0.44	0.63	−0.21	−0.14	1192	1.310	1.349
6-a	0.48	0.63	0.01	0.09	1235	1.357	1.347
6-b	0.49	0.64	−0.03	0.04	1173	1.303	1.353
7-a	0.33	0.48	−0.33	−0.27	1325	1.293	1.388
7-b	0.55	0.71	−0.05	0.01	1298	1.317	1.382
8-a	0.69	0.85	−0.14	−0.10	1379	1.358	1.355
8-b	0.52	0.67	−0.18	−0.12	1357	1.327	1.363
9	0.62	0.76	−0.02	0.04	1214	1.307	1.356

Note: n = 1–9, the energy barriers ($\Delta E^{\neq}_{TS,ZPE}$, $\Delta E^{\neq}_{TS}$) and reaction energies ($\Delta E_{r,ZPE}$, ΔE_r) were in the unit of eV, the bond lengths ($d^{\neq}_{O\cdots H}$, $d^{\neq}_{C\cdots H}$) were in the unit of Å, and the frequencies (δ^i_{TS}) were in the unit of cm^{-1}.

Table S2 Energetic aspects of surface H_2O^* dissociation with *n* adsorbing OH*.

$$n\,OH^* + H_2O^* \rightarrow (n+1)HO^* + H^*$$

n	$\Delta E^{\neq}_{TS,ZPE}$	$\Delta E^{\neq}_{TS}$	$\Delta E_{r,ZPE}$	ΔE_r	δ^i_{TS}	$d^{\neq}_{O\cdots H}$	$d^{\neq}_{C\cdots H}$
1-a	1.00	1.15	0.71	0.78	1219	1.354	1.321
1-b	0.43	0.58	0.19	0.23	1020	1.345	1.295
1-c	0.35	0.49	0.11	0.19	1169	1.356	1.325
2-a	1.28	1.45	0.77	0.83	1232	1.361	1.311
2-b	0.72	0.86	0.33	0.36	985	1.405	1.267
2-c	0.46	0.60	0.15	0.18	1210	1.330	1.334
3-a	1.02	1.17	0.75	0.77	1172	1.368	1.301
3-b	0.96	1.11	0.73	0.79	1074	1.335	1.302
3-c	0.68	0.83	0.21	0.26	1213	1.377	1.351
4-a	1.53	1.69	0.91	0.98	897	1.468	1.250
4-b	0.96	1.14	0.87	0.95	853	1.458	1.260
4-c	0.82	0.99	0.61	0.68	1175	1.371	1.308
5-a	1.41	1.57	1.13	1.19	1059	1.429	1.272
5-b	1.06	1.23	0.95	1.02	851	1.464	1.260
5-c	1.02	1.19	0.77	0.85	914	1.442	1.267
6-a	1.67	1.86	1.18	1.27	1212	1.378	1.301
6-b	1.63	1.80	1.32	1.39	665	1.526	1.231
7	1.71	1.87	1.43	1.52	821	1.486	1.231
8	1.35	1.53	1.41	1.49	942	1.444	1.266

Note: *n* = 1–8, the energy barriers ($\Delta E^{\neq}_{TS,ZPE}$, $\Delta E^{\neq}_{TS}$) and reaction energies ($\Delta E_{r,ZPE}$, ΔE_r) were in the unit of eV, the bond lengths ($d^{\neq}_{O\cdots H}$, $d^{\neq}_{C\cdots H}$) were in the unit of Å, and the frequencies (δ^i_{TS}) were in the unit of cm^{-1}.

Appendix A Related Publication

Journal Paper

1. Chu C, Li C, Liu X, Zhao H, Wu C, Li J, Liu K*, Li Q, **Cao D***. The surface phase structure evolution of the fcc MoC (001) surface in a steam reforming atmosphere: systematic kinetic and thermodynamic investigations. Catalysis Science & Technology. 2022;12(4):1130-43.

   Contribution: Came up with the main idea for this article, supervised the project, completed the data analysis, and wrote the article. As the author was involved in both the content of the paper and the supervision work, he was listed as a corresponding author. This publication was partly included in Chapter 4 of this thesis.

2. **Cao D,** Chu C, Chen B, Wu C, Li Q, Li Q, Liu B, Jia W, Li D, Ding Y, Liu K*. Low Temperature Water Gas Shift Reaction with Molybdenum Carbide: Insights from the Energetic Span Model. Applied Surface Science. (Submitted)

   Contribution: Came up with the main idea for this article, completed the data analysis, and wrote the article. This publication was included in Chapter 5 and 6 of this thesis.

3. Li J, Wu C, **Cao D**, Hu S, Weng L, Liu K. Green Methanol—An Important Pathway to Realize Carbon Neutrality. Engineering. 2023. (10.1016/j.eng.2023.08.005).

   Contribution: Provides an overview of methanol and hydrogen energy and related technological advances. The introduction of the present thesis contains some content.

Book Chapter

1. Liu K, Wu C, **Cao D,** Li J, Carbon Neutral Misconceptions and Pathways to Achievement, in Chapter 13 Critical issues and disruptive technologies for carbon neutrality, Z. Hu, Editor. 2022, Tsinghua University Press: Beijing.

   Contribution: Wrote the sections on methanol economy for the promotion of hydrogen energy, which are also the introductory parts of this thesis.

Reference

1. K. Alanne and S. Cao, *An overview of the concept and technology of ubiquitous energy.* Applied Energy, 2019. **238**: p. 284-302.

2. *Global Warming of 1.5°C*, in *An IPCC Special Report on the impacts of global warming of 1.5°C above pre-industrial levels and related global greenhouse gas emission pathways, in the context of strengthening the global response to the threat of climate change, sustainable development, and efforts to eradicate poverty*, V. Masson-Delmotte, P. Zhai, H.-O. Pörtner, D. Roberts, J. Skea, P.R. Shukla, A. Pirani, W. Moufouma-Okia, C. Péan, R. Pidcock, S. Connors, J.B.R. Matthews, Y. Chen, X. Zhou, M.I. Gomis, E. Lonnoy, T. Maycock, M. Tignor, and T. Waterfield, Editor. 2018, IPCC.

3. Y. Gao, X. Gao, and X. Zhang, *The 2 °C Global Temperature Target and the Evolution of the Long-Term Goal of Addressing Climate Change—From the United Nations Framework Convention on Climate Change to the Paris Agreement.* Engineering, 2017. **3**(2): p. 272-278.

4. Y. Xu, T. Ancev, and R. Betz, *Sustainable energy transition toward renewables: Drivers and hurdles.* Energy Policy, 2019. **134**.

5. R. York and S.E. Bell, *Energy transitions or additions?* Energy Research & Social Science, 2019. **51**: p. 40-43.

6. S.E. Hosseini and M.A. Wahid, *Hydrogen production from renewable and sustainable energy resources: Promising green energy carrier for clean development.* Renewable and Sustainable Energy Reviews, 2016. **57**: p. 850-866.

7. F. Barbir, *Transition to renewable energy systems with hydrogen as an energy carrier.* Energy, 2009. **34**(3): p. 308-312.

8. N. Muradov and T. Veziroglu, *"Green" path from fossil-based to hydrogen economy: An overview of carbon-neutral technologies.* International Journal of Hydrogen Energy, 2008. **33**(23): p. 6804-6839.

9. M. Balat, *Potential importance of hydrogen as a future solution to environmental and transportation problems.* International Journal of Hydrogen Energy, 2008. **33**(15): p. 4013-4029.

10. T. Sinigaglia, F. Lewiski, M.E. Santos Martins, and J.C. Mairesse Siluk, *Production, storage, fuel stations of hydrogen and its utilization in automotive applications-a review.* International Journal of Hydrogen Energy, 2017. **42**(39): p. 24597-24611.

11. A.G. Stern, *A new sustainable hydrogen clean energy paradigm.* International Journal of Hydrogen Energy, 2018. **43**(9): p. 4244-4255.

12. A.M. Elberry, J. Thakur, A. Santasalo-Aarnio, and M. Larmi, *Large-scale compressed hydrogen storage as part of renewable electricity storage systems.* International Journal of Hydrogen Energy, 2021. **46**(29): p. 15671-15690.

13. F. Ausfelder and A. Bazzanella, *Hydrogen in the Chemical Industry*, in *Hydrogen Science and Engineering : Materials, Processes, Systems and Technology*. 2016. p. 19-40.

14. M. Gurz, E. Baltacioglu, Y. Hames, and K. Kaya, *The meeting of hydrogen and automotive: A review.* International Journal of Hydrogen Energy, 2017. **42**(36): p. 23334-23346.

15. S. McQueen, J. Stanford, S. Satyapal, E. Miller, N. Stetson, . . . K. Randolph, *Department of energy hydrogen program plan*. 2020, US Department of Energy (USDOE), Washington DC (United States).

16. A. Veziroglu and R. Macario, *Fuel cell vehicles: State of the art with economic and environmental concerns.* International Journal of Hydrogen Energy, 2011. **36**(1): p. 25-43.

17. P.E. Dodds, I. Staffell, A.D. Hawkes, F. Li, P. Grünewald, W. McDowall, and P. Ekins, *Hydrogen and fuel cell technologies for heating: A review.* International Journal of Hydrogen Energy, 2015. **40**(5): p. 2065-2083.

18. S. Singh, S. Jain, V. Ps, A.K. Tiwari, M.R. Nouni, J.K. Pandey, and S. Goel, *Hydrogen: A sustainable fuel for future of the transport sector.* Renewable and Sustainable Energy Reviews, 2015. **51**: p. 623-633.

19. C.A. Kukkonen, *Hydrogen as an Alternative Automotive Fuel.* SAE Transactions, 1981. **90**: p. 1425-1461.

20. IEA, *The Future of Hydrogen*, I.E. Agency, Editor. 2019: Paris.

21. T. da Silva Veras, T.S. Mozer, D. da Costa Rubim Messeder dos Santos, and A. da Silva César, *Hydrogen: Trends, production and characterization of the main process worldwide.* International Journal of Hydrogen Energy, 2017. **42**(4): p. 2018-2033.

22. H. Lohse-Busch, K. Stutenberg, M. Duoba, and S. Iliev, *Technology Assessment Of A Fuel Cell Vehicle: 2017 Toyota Mirai*. 2018, ; Argonne National Lab. (ANL), Argonne, IL (United States).

23. Z. Xu, D. Qiu, P. Yi, L. Peng, and X. Lai, *Towards mass applications: A review on the challenges and developments in metallic bipolar plates for PEMFC.* Progress in Natural Science: Materials International, 2020. **30**(6): p. 815-824.

24. R.-A. Felseghi, E. Carcadea, M.S. Raboaca, C.N. Trufin, and C. Filote, *Hydrogen Fuel Cell Technology for the Sustainable Future of Stationary Applications.* Energies, 2019. **12**(23).

25. W. Cao, J. Zhang, and H. Li, *Batteries with high theoretical energy densities.* Energy Storage Materials, 2020. **26**: p. 46-55.

26. J. Li, C. Wu, D. Cao, S. Hu, L. Weng, and K. Liu, *Green Methanol—An Important Pathway to Realize Carbon Neutrality.* Engineering, 2023.

27. O. Faye, J. Szpunar, and U. Eduok, *A critical review on the current technologies for the generation, storage, and transportation of hydrogen.* International Journal of Hydrogen Energy, 2022. **47**(29): p. 13771-13802.

28. H.T. Hwang and A. Varma, *Hydrogen storage for fuel cell vehicles.* Current Opinion in Chemical Engineering, 2014. **5**: p. 42-48.

29. A.M. Abdalla, S. Hossain, O.B. Nisfindy, A.T. Azad, M. Dawood, and A.K. Azad, *Hydrogen production, storage, transportation and key challenges with applications: A review.* Energy Conversion and Management, 2018. **165**: p. 602-627.

30. G. Valenti, *2 - Hydrogen liquefaction and liquid hydrogen storage*, in *Compendium of Hydrogen Energy*, R.B. Gupta, A. Basile, and T.N. Veziroğlu, Editors. 2016, Woodhead Publishing. p. 27-51.

31. R.K. Ahluwalia, J.K. Peng, and T.Q. Hua, *5 - Cryo-compressed hydrogen storage*, in *Compendium of Hydrogen Energy*, R.B. Gupta, A. Basile, and T.N. Veziroğlu, Editors. 2016, Woodhead Publishing. p. 119-145.

32. P. Rao and M. Yoon, *Potential Liquid-Organic Hydrogen Carrier (LOHC) Systems: A Review on Recent Progress.* Energies, 2020. **13**(22).

33. A.T. Wijayanta, T. Oda, C.W. Purnomo, T. Kashiwagi, and M. Aziz, *Liquid hydrogen, methylcyclohexane, and ammonia as potential hydrogen storage: Comparison review.* International Journal of Hydrogen Energy, 2019. **44**(29): p. 15026-15044.

34. B.A.H. Inc., *Research, development and demonstration of a fuel cell/battery powered bus system. Phase 1*. 1990: United States. p. 147.

35. I. Ganesh, *Conversion of carbon dioxide into methanol – a potential liquid fuel: Fundamental challenges and opportunities (a review).* Renewable and Sustainable Energy Reviews, 2014. **31**: p. 221-257.

36. M.J. Bos, S.R.A. Kersten, and D.W.F. Brilman, *Wind power to methanol: Renewable methanol production using electricity, electrolysis of water and CO2 air capture.* Applied Energy, 2020. **264**.

37. D.D. Papadias, J.-K. Peng, and R.K. Ahluwalia, *Hydrogen carriers: Production, transmission, decomposition, and storage.* International Journal of Hydrogen Energy, 2021. **46**(47): p. 24169-24189.

38. T.B. Reed and R.M. Lerner, *Methanol: A Versatile Fuel for Immediate Use.* Science, 1973. **182**(4119): p. 1299-1304.

39. C. Chen and A. Yang, *Power-to-methanol: The role of process flexibility in the integration of variable renewable energy into chemical production.* Energy Conversion and Management, 2021. **228**.

40. P. Battaglia, G. Buffo, D. Ferrero, M. Santarelli, and A. Lanzini, *Methanol synthesis through CO_2 capture and hydrogenation: Thermal integration, energy performance and techno-economic assessment.* Journal of CO_2 Utilization, 2021. **44**.

41. N. Rambhujun, M.S. Salman, T. Wang, C. Pratthana, P. Sapkota, M. Costalin, . . . K.-F. Aguey-Zinsou, *Renewable hydrogen for the chemical industry.* MRS Energy & Sustainability, 2020. **7**: p. E33.

42. M. Niermann, S. Drünert, M. Kaltschmitt, and K. Bonhoff, *Liquid organic hydrogen carriers (LOHCs) – techno-economic analysis of LOHCs in a defined process chain.* Energy & Environmental Science, 2019. **12**(1): p. 290-307.

43. E. Santacesaria and S. Carrá, *Kinetics of catalytic steam reforming of methanol in a cstr reactor.* Applied Catalysis, 1983. **5**(3): p. 345-358.

44. W.-H. Chen and C.-Y. Chen, *Water gas shift reaction for hydrogen production and carbon dioxide capture: A review.* Applied Energy, 2020. **258**: p. 114078.

45. C. Rhodes, G.J. Hutchings, and A.M. Ward, *Water-gas shift reaction: finding the mechanistic boundary.* Catalysis Today, 1995. **23**(1): p. 43-58.

46. T.L. LeValley, A.R. Richard, and M. Fan, *The progress in water gas shift and steam reforming hydrogen production technologies – A review.* International Journal of Hydrogen Energy, 2014. **39**(30): p. 16983–17000.

47. X. Zhang, M. Zhang, Y. Deng, M. Xu, L. Artiglia, W. Wen, . . . D. Ma, *A stable low-temperature H_2-production catalyst by crowding Pt on alpha-MoC.* Nature, 2021. **589**(7842): p. 396-401.

48. L. Lin, W. Zhou, R. Gao, S. Yao, X. Zhang, W. Xu, . . . D. Ma, *Low-temperature hydrogen production from water and methanol using Pt/alpha-MoC catalysts.* Nature, 2017. **544**(7648): p. 80-83.

49. D.T. Burns, G. Piccardi, and L. Sabbatini, *Some people and places important in the history of analytical chemistry in Italy.* Microchimica Acta, 2008. **160**(1): p. 57-87.

50. A.L. de Lavoisier, *Oeuvres de Lavoisier*. Vol. II. 1862: Imprimerie Impériale.

51. S. Xiao, J. Xu, Y. Wang, J. Wang, and X. Xu, *Investigation of a methanol processing system comprising of a steam reformer and two preferential oxidation reactors for fuel cells.* International Journal of Hydrogen Energy, 2022. **47**(68): p. 29242-29254.

52. M. O'Connell, G. Kolb, K.-P. Schelhaas, J. Schuerer, D. Tiemann, A. Ziogas, and V. Hessel, *The development and evaluation of microstructured reactors for the water gas shift and preferential oxidation reactions in the 5kW range.* International Journal of Hydrogen Energy, 2010. **35**(6): p. 2317–2327.

53. E. Baraj, K. Ciahotný, and T. Hlinčík, *The water gas shift reaction: Catalysts and reaction mechanism.* Fuel, 2021. **288**.

54. D.S. Newsome, *The Water-Gas Shift Reaction.* Catalysis Reviews, 1980. **21**(2): p. 275-318.

55. E.F. Armstrong, T.P. Hilditch, and H.E. Armstrong, *A study of catalytic actions at solid surfaces. —IV. The interaction of carbon monoxide and steam as conditioned by iron oxide and by copper.* Proceedings of the Royal Society of London. Series A, Containing Papers of a Mathematical and Physical Character, 1920. **97**(684): p. 265-273.

56. N. Kul'Kova and M. Temkin, *Kinetics of the reaction of conversion of carbon monoxide by water vapors (shift-reaction).* Russ J Phys Chem, 1949. **23**: p. 695-700.

57. X.-Q. Gong, P. Hu, and R. Raval, *The catalytic role of water in CO oxidation.* The Journal of Chemical Physics, 2003. **119**(12): p. 6324-6334.

58. A.B. Mhadeshwar and D.G. Vlachos, *Microkinetic Modeling for Water-Promoted CO Oxidation, Water−Gas Shift, and Preferential Oxidation of CO on Pt.* The

Journal of Physical Chemistry B, 2004. **108**(39): p. 15246-15258.

59. L.C. Grabow, A.A. Gokhale, S.T. Evans, J.A. Dumesic, and M. Mavrikakis, *Mechanism of the Water Gas Shift Reaction on Pt: First Principles, Experiments, and Microkinetic Modeling.* The Journal of Physical Chemistry C, 2008. **112**(12): p. 4608-4617.

60. A.A. Gokhale, J.A. Dumesic, and M. Mavrikakis, *On the Mechanism of Low-Temperature Water Gas Shift Reaction on Copper.* Journal of the American Chemical Society, 2008. **130**(4): p. 1402-1414.

61. C. Ratnasamy and J.P. Wagner, *Water Gas Shift Catalysis.* Catalysis Reviews, 2009. **51**(3): p. 325-440.

62. X.-P. Fu, L.-W. Guo, W.-W. Wang, C. Ma, C.-J. Jia, K. Wu, . . . C.-H. Yan, *Direct Identification of Active Surface Species for the Water–Gas Shift Reaction on a Gold–Ceria Catalyst.* Journal of the American Chemical Society, 2019. **141**(11): p. 4613-4623.

63. N.C. Nelson, M.-T. Nguyen, V.-A. Glezakou, R. Rousseau, and J. Szanyi, *Carboxyl intermediate formation via an in situ-generated metastable active site during water-gas shift catalysis.* Nature Catalysis, 2019. **2**(10): p. 916-924.

64. N.C. Nelson, L. Chen, D. Meira, L. Kovarik, and J. Szanyi, *In Situ Dispersion of Palladium on TiO_2 During Reverse Water–Gas Shift Reaction: Formation of Atomically Dispersed Palladium.* Angewandte Chemie International Edition, 2020. **59**(40): p. 17657-17663.

65. N.C. Nelson and J. Szanyi, *Heterolytic Hydrogen Activation: Understanding Support Effects in Water–Gas Shift, Hydrodeoxygenation, and CO Oxidation Catalysis.* ACS Catalysis, 2020. **10**(10): p. 5663-5671.

66. S. Yao, X. Zhang, W. Zhou, R. Gao, W. Xu, Y. Ye, . . . D. Ma, *Atomic-layered Au clusters on α-MoC as catalysts for the low-temperature water-gas shift reaction.* Science, 2017. **357**(6349): p. 389-393.

67. X. Zhang, C. Shi, B. Chen, A.N. Kuhn, D. Ma, and H. Yang, *Progress in hydrogen production over transition metal carbide catalysts: challenges and opportunities.* Current Opinion in Chemical Engineering, 2018. **20**: p. 68-77.

68. L. Lin, Q. Yu, M. Peng, A. Li, S. Yao, S. Tian, . . . D. Ma, *Atomically Dispersed Ni/alpha-MoC Catalyst for Hydrogen Production from Methanol/Water.* J Am Chem Soc, 2021. **143**(1): p. 309-317.

69. Z. Lin, S.R. Denny, and J.G. Chen, *Transition metal carbides and nitrides as*

catalysts for thermochemical reactions. Journal of Catalysis, 2021. **404**: p. 929-942.

70. L. Sun, J. Xu, X. Liu, B. Qiao, L. Li, Y. Ren, . . . T. Zhang, *High-Efficiency Water Gas Shift Reaction Catalysis on α-MoC Promoted by Single-Atom Ir Species.* ACS Catalysis, 2021. **11**(10): p. 5942-5950.

71. Y. Chen, J. Lin, and X. Wang, *Noble-metal based single-atom catalysts for the water-gas shift reaction.* Chem Commun (Camb), 2021. **58**(2): p. 208-222.

72. J.G. Chen, *Carbide and Nitride Overlayers on Early Transition Metal Surfaces: Preparation, Characterization, and Reactivities.* Chemical Reviews, 1996. **96**(4): p. 1477-1498.

73. H.H. Hwu and J.G. Chen, *Surface Chemistry of Transition Metal Carbides.* Chemical Reviews, 2005. **105**(1): p. 185-212.

74. P.A. Alaba, A. Abbas, J. Huang, and W.M.A.W. Daud, *Molybdenum carbide nanoparticle: Understanding the surface properties and reaction mechanism for energy production towards a sustainable future.* Renewable and Sustainable Energy Reviews, 2018. **91**: p. 287-300.

75. Y. Deng, Y. Ge, M. Xu, Q. Yu, D. Xiao, S. Yao, and D. Ma, *Molybdenum Carbide: Controlling the Geometric and Electronic Structure of Noble Metals for the Activation of O–H and C–H Bonds.* Accounts of Chemical Research, 2019. **52**(12): p. 3372-3383.

76. W. Wan, B.M. Tackett, and J.G. Chen, *Reactions of water and C1 molecules on carbide and metal-modified carbide surfaces.* Chemical Society Reviews, 2017. **46**(7): p. 1807-1823.

77. Y. Ma, G. Guan, X. Hao, J. Cao, and A. Abudula, *Molybdenum carbide as alternative catalyst for hydrogen production – A review.* Renewable and Sustainable Energy Reviews, 2017. **75**: p. 1101-1129.

78. Y. Ma, G. Guan, C. Shi, A. Zhu, X. Hao, Z. Wang, . . . A. Abudula, *Low-temperature steam reforming of methanol to produce hydrogen over various metal-doped molybdenum carbide catalysts.* International Journal of Hydrogen Energy, 2014. **39**(1): p. 258-266.

79. F. Cai, J.J. Ibrahim, Y. Fu, W. Kong, J. Zhang, and Y. Sun, *Low-temperature hydrogen production from methanol steam reforming on Zn-modified Pt/MoC catalysts.* Applied Catalysis B: Environmental, 2020. **264**.

80. F. Cai, Y. Guo, J.J. Ibrahim, J. Zhang, and Y. Sun, *A highly active and stable*

Pd/MoC catalyst for hydrogen production from methanol decomposition. Applied Catalysis B: Environmental, 2021. **299**.

81. J.A. Rodriguez, P.J. Ramírez, and R.A. Gutierrez, *Highly active Pt/MoC and Pt/TiC catalysts for the low-temperature water-gas shift reaction: Effects of the carbide metal/carbon ratio on the catalyst performance.* Catalysis Today, 2017. **289**: p. 47-52.

82. M. Khzouz, J. Wood, B. Pollet, and W. Bujalski, *Characterization and activity test of commercial Ni/Al_2O_3, Cu/ZnO/Al_2O_3 and prepared Ni–Cu/Al_2O_3 catalysts for hydrogen production from methane and methanol fuels.* International Journal of Hydrogen Energy, 2013. **38**(3): p. 1664-1675.

83. M. Khzouz, E.I. Gkanas, S. Du, and J. Wood, *Catalytic performance of Ni-Cu/Al_2O_3 for effective syngas production by methanol steam reforming.* Fuel, 2018. **232**: p. 672-683.

84. X. Hou, S. Qing, Y. Liu, L. Li, Z. Gao, and Y. Qin, *Enhancing effect of MgO modification of Cu–Al spinel oxide catalyst for methanol steam reforming.* International Journal of Hydrogen Energy, 2020. **45**(1): p. 477-489.

85. D. Li, Y. Li, X. Liu, Y. Guo, C.-W. Pao, J.-L. Chen, . . . Y. Wang, *$NiAl_2O_4$ Spinel Supported Pt Catalyst: High Performance and Origin in Aqueous-Phase Reforming of Methanol.* ACS Catalysis, 2019. **9**(10): p. 9671-9682.

86. J.-L. Calais, *Band structure of transition metal compounds.* Advances in Physics, 1977. **26**(6): p. 847-885.

87. R.B. Levy and M. Boudart, *Platinum-Like Behavior of Tungsten Carbide in Surface Catalysis.* Science, 1973. **181**(4099): p. 547-549.

88. M. Wu, X. Lin, A. Hagfeldt, and T. Ma, *Low-Cost Molybdenum Carbide and Tungsten Carbide Counter Electrodes for Dye-Sensitized Solar Cells.* Angewandte Chemie International Edition, 2011. **50**(15): p. 3520-3524.

89. G. Kaye, *Face-centred Cubic Molybdenum Monocarbide.* Nature, 1962. **195**(4847): p. 1195-1196.

90. J. Patt, D.J. Moon, C. Phillips, and L. Thompson, *Molybdenum carbide catalysts for water–gas shift.* Catalysis Letters, 2000. **65**(4): p. 193-195.

91. Z. Lin, L. Cai, W. Lu, and Y. Chai, *Phase and Facet Control of Molybdenum Carbide Nanosheet Observed by In Situ TEM.* Small, 2017. **13**(35).

92. M.G. Quesne, A. Roldan, N.H. de Leeuw, and C.R.A. Catlow, *Bulk and surface*

properties of metal carbides: implications for catalysis. Phys Chem Chem Phys, 2018. **20**(10): p. 6905-6916.

93. S.T. Oyama, *Preparation and catalytic properties of transition metal carbides and nitrides.* Catalysis Today, 1992. **15**(2): p. 179-200.

94. Y. Zhong, X. Xia, F. Shi, J. Zhan, J. Tu, and H.J. Fan, *Transition Metal Carbides and Nitrides in Energy Storage and Conversion.* Adv Sci (Weinh), 2016. **3**(5): p. 1500286.

95. H.W. Hugosson, O. Eriksson, U. Jansson, and B. Johansson, *Phase stabilities and homogeneity ranges in 4d-transition-metal carbides: A theoretical study.* Physical Review B, 2001. **63**(13): p. 134108.

96. A. De Zanet and S.A. Kondrat, *A Review of Preparation Strategies for α-MoC_{1-x} Catalysts.* Johnson Matthey Technology Review, 2022.

97. J. Dong, Q. Fu, Z. Jiang, B. Mei, and X. Bao, *Carbide-Supported Au Catalysts for Water–Gas Shift Reactions: A New Territory for the Strong Metal–Support Interaction Effect.* Journal of the American Chemical Society, 2018. **140**(42): p. 13808-13816.

98. S. Posada-Pérez, R.A. Gutiérrez, Z. Zuo, P.J. Ramírez, F. Viñes, P. Liu, . . . J.A. Rodriguez, *Highly active Au/δ-MoC and Au/β-Mo_2C catalysts for the low-temperature water gas shift reaction: effects of the carbide metal/carbon ratio on the catalyst performance.* Catalysis Science & Technology, 2017. **7**(22): p. 5332-5342.

99. J.L.C. Fajín and M.N.D.S. Cordeiro, *Insights into the Mechanism of Methanol Steam Reforming for Hydrogen Production over Ni–Cu-Based Catalysts.* ACS Catalysis, 2021. **12**(1): p. 512-526.

100. X. Tang, J. Li, Z. Fang, X. Dong, C. Sun, X. Qiao, and X. Li, *Single Ni-inserted Cu (111) surface: A DFT study of adsorption and reaction mechanisms of methanol steam reforming.* Applied Surface Science, 2022. **596**: p. 153635.

101. A.M. Ranjekar and G.D. Yadav, *Steam Reforming of Methanol for Hydrogen Production: A Critical Analysis of Catalysis, Processes, and Scope.* Industrial & Engineering Chemistry Research, 2021. **60**(1): p. 89-113.

102. P. Sabatier, *Hydrogénations et déshydrogénations par catalyse.* Berichte der deutschen chemischen Gesellschaft, 1911. **44**(3): p. 1984-2001.

103. A.A. Balandin, *Modern State of the Multiplet Theor of Heterogeneous Catalysis*, in *Advances in Catalysis*, D.D. Eley, H. Pines, and P.B. Weisz, Editors. 1969,

Academic Press. p. 1-210.

104. A.J. Medford, A. Vojvodic, J.S. Hummelshøj, J. Voss, F. Abild-Pedersen, F. Studt, . . . J.K. Nørskov, *From the Sabatier principle to a predictive theory of transition-metal heterogeneous catalysis.* Journal of Catalysis, 2015. **328**: p. 36-42.

105. J. Pérez-Ramírez and N. López, *Strategies to break linear scaling relationships.* Nature Catalysis, 2019. **2**(11): p. 971-976.

106. P. Liu and J.A. Rodriguez, *Water-Gas-Shift Reaction on Molybdenum Carbide Surfaces: Essential Role of the Oxycarbide.* The Journal of Physical Chemistry B, 2006. **110**(39): p. 19418-19425.

107. J.R.d.S. Politi, F. Viñes, J.A. Rodriguez, and F. Illas, *Atomic and electronic structure of molybdenum carbide phases: bulk and low Miller-index surfaces.* Physical Chemistry Chemical Physics, 2013. **15**(30): p. 12617-12625.

108. C. Chu, X. Liu, C. Wu, J. Li, and K. Liu, *Surface phase structures responsible for the activity and deactivation of the fcc MoC (111)-Mo surface in steam reforming: a systematic kinetic and thermodynamic investigation.* Catalysis Science & Technology, 2021. **11**(3): p. 823-835.

109. J.-X. Liang, J. Lin, J. Liu, X. Wang, T. Zhang, and J. Li, *Dual Metal Active Sites in an Ir1 /FeOx Single-Atom Catalyst: A Redox Mechanism for the Water-Gas Shift Reaction.* Angew Chem Int Ed Engl, 2020. **59**(31): p. 12868-12875.

110. P. Yin, J. Yu, L. Wang, J. Zhang, Y. Jie, L.-F. Chen, . . . M. Wei, *Water-Gas-Shift Reaction on Au/TiO_{2-x} Catalysts with Various TiO_2 Crystalline Phases: A Theoretical and Experimental Study.* The Journal of Physical Chemistry C, 2021. **125**(37): p. 20360-20372.

111. W. Song and E.J.M. Hensen, *Mechanistic Aspects of the Water–Gas Shift Reaction on Isolated and Clustered Au Atoms on CeO_2(110): A Density Functional Theory Study.* ACS Catalysis, 2014. **4**(6): p. 1885-1892.

112. H. Prats, S. Posada-Pérez, J.A. Rodriguez, R. Sayós, and F. Illas, *Kinetic Monte Carlo Simulations Unveil Synergic Effects at Work on Bifunctional Catalysts.* ACS Catalysis, 2019. **9**(10): p. 9117-9126.

113. J. Li, L. Sun, Q. Wan, J. Lin, S. Lin, and X. Wang, *α-MoC Supported Noble Metal Catalysts for Water-Gas Shift Reaction: Single-Atom Promoter or Single-Atom Player.* J Phys Chem Lett, 2021. **12**(46): p. 11415-11421.

114. C. Jimenez-Orozco, E. Flórez, F. Viñes, J.A. Rodriguez, and F. Illas, *Critical*

Hydrogen Coverage Effect on the Hydrogenation of Ethylene Catalyzed by δ-MoC(001): An Ab Initio Thermodynamic and Kinetic Study. ACS Catalysis, 2020. **10**(11): p. 6213-6222.

115. D. Li, F. Xu, X. Tang, S. Dai, T. Pu, X. Liu, . . . M. Zhu, *Induced activation of the commercial Cu/ZnO/Al_2O_3 catalyst for the steam reforming of methanol.* Nature Catalysis, 2022. **5**(2): p. 99-108.

116. K. Reuter and M. Scheffler, *First-Principles Atomistic Thermodynamics for Oxidation Catalysis: Surface Phase Diagrams and Catalytically Interesting Regions.* Physical Review Letters, 2003. **90**(4): p. 046103.

117. K. Reuter and M. Scheffler, *Composition and structure of the RuO_2(110) surface in an O_2 and CO environment: Implications for the catalytic formation of CO_2.* Physical Review B, 2003. **68**(4): p. 045407.

118. H. Tian, Y. He, Q. Zhao, J. Li, X. Shao, Z. Zhang, . . . S.Y. Tong, *Avoiding Sabatier's conflict in bifunctional heterogeneous catalysts for the WGS reaction.* Chem, 2021. **7**(5): p. 1271-1283.

119. Z.-S. Zhang, Q. Fu, K. Xu, W.-W. Wang, X.-P. Fu, X.-S. Zheng, . . . C.-H. Yan, *Intrinsically Active Surface in a Pt/gamma-Mo_2N Catalyst for the Water-Gas Shift Reaction: Molybdenum Nitride or Molybdenum Oxide?* J Am Chem Soc, 2020. **142**(31): p. 13362-13371.

120. S. Kozuch and J.M.L. Martin, *"Turning Over" Definitions in Catalytic Cycles.* ACS Catalysis, 2012. **2**(12): p. 2787-2794.

121. S. Kozuch and S. Shaik, *How to Conceptualize Catalytic Cycles? The Energetic Span Model.* Accounts of Chemical Research, 2011. **44**(2): p. 101-110.

122. S. Kozuch and J.M.L. Martin, *The Rate-Determining Step is Dead. Long Live the Rate-Determining State!* ChemPhysChem, 2011. **12**(8): p. 1413-1418.

123. S. Kozuch and J.M.L. Martin, *What Makes for a Bad Catalytic Cycle? A Theoretical Study on the Suzuki−Miyaura Reaction within the Energetic Span Model.* ACS Catalysis, 2011. **1**(4): p. 246-253.

124. A. Szabo and N.S. Ostlund, *Modern quantum chemistry: introduction to advanced electronic structure theory*. 2012: Courier Corporation.

125. P.W. Atkins and R.S. Friedman, *Molecular quantum mechanics*. 2011: Oxford university press.

126. B.W.J. Chen, L. Xu, and M. Mavrikakis, *Computational Methods in*

Heterogeneous Catalysis. Chem Rev, 2021. **121**(2): p. 1007-1048.

127. E. Schrödinger, *An Undulatory Theory of the Mechanics of Atoms and Molecules.* Physical Review, 1926. **28**(6): p. 1049-1070.

128. D.J. Griffiths and D.F. Schroeter, *Introduction to Quantum Mechanics*. 3 ed. 2018, Cambridge: Cambridge University Press.

129. M. Born and R. Oppenheimer, *Zur Quantentheorie der Molekeln.* Annalen der Physik, 1927. **389**(20): p. 457-484.

130. E.G. Lewars, *Computational Chemistry: Introduction to the Theory and Applications of Molecular and Quantum Mechanics*. 2nd ed. 2011.

131. L.H. Thomas, *The calculation of atomic fields.* Mathematical Proceedings of the Cambridge Philosophical Society, 1927. **23**(5): p. 542-548.

132. E. Fermi, *Un metodo statistico per la determinazione di alcune priorieta dell'atome.* Rend. Accad. Naz. Lincei, 1927. **6**(602-607): p. 32.

133. P. Hohenberg and W. Kohn, *Inhomogeneous Electron Gas.* Physical Review, 1964. **136**(3B): p. B864-B871.

134. W. Kohn and L.J. Sham, *Self-Consistent Equations Including Exchange and Correlation Effects.* Physical Review, 1965. **140**(4A): p. A1133-A1138.

135. A.D. Becke, *Perspective: Fifty years of density-functional theory in chemical physics.* J Chem Phys, 2014. **140**(18): p. 18A301.

136. N. Mardirossian and M. Head-Gordon, *Thirty years of density functional theory in computational chemistry: an overview and extensive assessment of 200 density functionals.* Molecular Physics, 2017. **115**(19): p. 2315-2372.

137. J.P. Perdew, A. Ruzsinszky, J. Tao, V.N. Staroverov, G.E. Scuseria, and G.I. Csonka, *Prescription for the design and selection of density functional approximations: More constraint satisfaction with fewer fits.* The Journal of Chemical Physics, 2005. **123**(6).

138. Q. Peng, F. Duarte, and R.S. Paton, *Computing organic stereoselectivity - from concepts to quantitative calculations and predictions.* Chem Soc Rev, 2016. **45**(22): p. 6093-6107.

139. J.P. Perdew, *Density-functional approximation for the correlation energy of the inhomogeneous electron gas.* Physical Review B, 1986. **33**(12): p. 8822-8824.

140. J.P. Perdew and Y. Wang, *Accurate and simple analytic representation of the*

electron-gas correlation energy. Physical Review B, 1992. **45**(23): p. 13244-13249.

141. J.P. Perdew, K. Burke, and M. Ernzerhof, *Generalized Gradient Approximation Made Simple.* Physical Review Letters, 1996. **77**(18): p. 3865-3868.

142. J. Sun, R.C. Remsing, Y. Zhang, Z. Sun, A. Ruzsinszky, H. Peng, . . . J.P. Perdew, *Accurate first-principles structures and energies of diversely bonded systems from an efficient density functional.* Nat Chem, 2016. **8**(9): p. 831-6.

143. J. Heyd, G.E. Scuseria, and M. Ernzerhof, *Hybrid functionals based on a screened Coulomb potential.* The Journal of Chemical Physics, 2003. **118**(18): p. 8207-8215.

144. L. Schimka, J. Harl, and G. Kresse, *Improved hybrid functional for solids: The HSEsol functional.* The Journal of Chemical Physics, 2011. **134**(2).

145. H. Li, L. Zhang, Q. Zeng, K. Guan, K. Li, H. Ren, . . . L. Cheng, *Structural, elastic and electronic properties of transition metal carbides TMC (TM=Ti, Zr, Hf and Ta) from first-principles calculations.* Solid State Communications, 2011. **151**(8): p. 602-606.

146. A. Tkatchenko and M. Scheffler, *Accurate Molecular Van Der Waals Interactions from Ground-State Electron Density and Free-Atom Reference Data.* Physical Review Letters, 2009. **102**(7): p. 073005.

147. S. Grimme, *Semiempirical GGA-type density functional constructed with a long-range dispersion correction.* Journal of Computational Chemistry, 2006. **27**(15): p. 1787-1799.

148. S. Grimme, J. Antony, S. Ehrlich, and H. Krieg, *A consistent and accurate ab initio parametrization of density functional dispersion correction (DFT-D) for the 94 elements H-Pu.* The Journal of Chemical Physics, 2010. **132**(15): p. 154104.

149. F. Bloch, *Über die Quantenmechanik der Elektronen in Kristallgittern.* Zeitschrift für Physik, 1929. **52**(7): p. 555-600.

150. H.J. Monkhorst and J.D. Pack, *Special points for Brillouin-zone integrations.* Physical Review B, 1976. **13**(12): p. 5188-5192.

151. J.C. Phillips and L. Kleinman, *New Method for Calculating Wave Functions in Crystals and Molecules.* Physical Review, 1959. **116**(2): p. 287-294.

152. P.E. Blöchl, *Projector augmented-wave method.* Physical Review B, 1994. **50**(24): p. 17953-17979.

153. H. Eyring, *The Activated Complex in Chemical Reactions.* The Journal of Chemical Physics, 1934. **3**(2): p. 107-115.

154. M.G. Evans and M. Polanyi, *Some applications of the transition state method to the calculation of reaction velocities, especially in solution.* Transactions of the Faraday Society, 1935. **31**(0): p. 875-894.

155. J. Gao and D.G. Truhlar, *Quantum Mechanical Methods for Enzyme Kinetics.* Annual Review of Physical Chemistry, 2002. **53**(1): p. 467-505.

156. G. Henkelman, B.P. Uberuaga, and H. Jónsson, *A climbing image nudged elastic band method for finding saddle points and minimum energy paths.* The Journal of Chemical Physics, 2000. **113**(22): p. 9901-9904.

157. J. Lu, S. Behtash, M. Faheem, and A. Heyden, *Microkinetic modeling of the decarboxylation and decarbonylation of propanoic acid over Pd(111) model surfaces based on parameters obtained from first principles.* Journal of Catalysis, 2013. **305**: p. 56-66.

158. F. Richard and R. Bader, *Atoms in molecules: a quantum theory*. 1990, Oxford University Press, Oxford.

159. G. Henkelman, A. Arnaldsson, and H. Jónsson, *A fast and robust algorithm for Bader decomposition of charge density.* Computational Materials Science, 2006. **36**(3): p. 354-360.

160. R. Iftimie, P. Minary, and M.E. Tuckerman, *Ab initio molecular dynamics: Concepts, recent developments, and future trends.* Proceedings of the National Academy of Sciences, 2005. **102**(19): p. 6654-6659.

161. L. Grajciar, C.J. Heard, A.A. Bondarenko, M.V. Polynski, J. Meeprasert, E.A. Pidko, and P. Nachtigall, *Towards operando computational modeling in heterogeneous catalysis.* Chemical Society reviews, 2018. **47**(22): p. 8307-8348.

162. L. Verlet, *Computer "Experiments" on Classical Fluids. I. Thermodynamical Properties of Lennard-Jones Molecules.* Physical Review, 1967. **159**(1): p. 98-103.

163. J.W. Gibbs, *Elementary principles in statistical mechanics: developed with especial reference to the rational foundations of thermodynamics*. 1902: C. Scribner's sons.

164. S. Nosé, *A unified formulation of the constant temperature molecular dynamics methods.* The Journal of Chemical Physics, 1984. **81**(1): p. 511-519.

165. W.G. Hoover, *Canonical dynamics: Equilibrium phase-space distributions.* Physical Review A, 1985. **31**(3): p. 1695-1697.

166. K. Reuter and M. Scheffler, *Composition, structure, and stability of RuO_2(110) as a function of oxygen pressure.* Physical Review B, 2001. **65**(3): p. 035406.

167. K. Reuter, C. Stampf, and M. Scheffler, *AB Initio Atomistic Thermodynamics and Statistical Mechanics of Surface Properties and Functions*, in *Handbook of Materials Modeling: Methods*, S. Yip, Editor. 2005, Springer Netherlands: Dordrecht. p. 149-194.

168. K. Reuter, *First-Principles Kinetic Monte Carlo Simulations for Heterogeneous Catalysis: Concepts, Status, and Frontiers*, in *Modeling and Simulation of Heterogeneous Catalytic Reactions*. 2011. p. 71-111.

169. J. Rogal and K. Reuter. *Ab Initio Atomistic Thermodynamics for Surfaces: A Primer*. in *VT-142 RTO AVT/VKI Lecture Series*. 2007. NATO Research and Technology Organisation.

170. O. Lamiel-Garcia, S. Tosoni, and F. Illas, *Relative Stability of F-Covered TiO_2 Anatase (101) and (001) Surfaces from Periodic DFT Calculations and ab Initio Atomistic Thermodynamics.* The Journal of Physical Chemistry C, 2014. **118**(25): p. 13667-13673.

171. D. Stull and H. Prophet, *JANAF Thermochemical Tables 2nd edn (Washington, DC: US National Bureau of Standards)*. 1971.

172. M. Boudart, *Turnover Rates in Heterogeneous Catalysis.* Chemical Reviews, 1995. **95**(3): p. 661-666.

173. J.-H. Wen, D. Guo, and G.-C. Wang, *Structure-sensitivity of direct oxidation methane to methanol over Rhn/ZrO_{2-x} (101) (n = 1, 4, 10) surfaces: A DFT study.* Applied Surface Science, 2021. **555**: p. 149690.

174. W. Xue, X. Song, and D. Mei, *Theoretical Insights into CO Oxidation over MOF-808-Encapsulated Single-Atom Metal Catalysts.* The Journal of Physical Chemistry C, 2021. **125**(31): p. 17097-17108.

175. S. Bac and S. Mallikarjun Sharada, *CO Oxidation with Atomically Dispersed Catalysts: Insights from the Energetic Span Model.* ACS Catalysis, 2022. **12**(3): p. 2064-2076.

176. G. Kresse and J. Furthmüller, *Efficiency of ab-initio total energy calculations for metals and semiconductors using a plane-wave basis set.* Computational Materials Science, 1996. **6**(1): p. 15-50.

177. G. Kresse and J. Furthmüller, *Efficient iterative schemes for ab initio total-energy calculations using a plane-wave basis set.* Physical Review B, 1996. **54**(16): p. 11169-11186.

178. G. Kresse and D. Joubert, *From ultrasoft pseudopotentials to the projector augmented-wave method.* Physical Review B, 1999. **59**(3): p. 1758-1775.

179. C. Chu, C. Li, X. Liu, H. Zhao, C. Wu, J. Li, . . . D. Cao, *The surface phase structure evolution of the fcc MoC (001) surface in a steam reforming atmosphere: systematic kinetic and thermodynamic investigations.* Catalysis Science & Technology, 2022. **12**(4): p. 1130-1143.

180. G. Henkelman and H. Jónsson, *A dimer method for finding saddle points on high dimensional potential surfaces using only first derivatives.* The Journal of Chemical Physics, 1999. **111**(15): p. 7010-7022.

181. A. Heyden, A.T. Bell, and F.J. Keil, *Efficient methods for finding transition states in chemical reactions: Comparison of improved dimer method and partitioned rational function optimization method.* The Journal of Chemical Physics, 2005. **123**(22): p. 224101.

182. G. Henkelman and H. Jónsson, *Improved tangent estimate in the nudged elastic band method for finding minimum energy paths and saddle points.* The Journal of Chemical Physics, 2000. **113**(22): p. 9978-9985.

183. *Jmol: an open-source Java viewer for chemical structures in 3D*.

184. S. Grimme, S. Ehrlich, and L. Goerigk, *Effect of the damping function in dispersion corrected density functional theory.* Journal of Computational Chemistry, 2011. **32**(7): p. 1456-1465.

185. V. Wang, N. Xu, J.C. Liu, G. Tang, and W.-T. Geng, *VASPKIT: a pre-and post-processing program for VASP code.* arXiv preprint arXiv:1908.08269, 2019.

186. C. Jimenez-Orozco, E. Flórez, A. Montoya, and J.A. Rodriguez, *Binding and activation of ethylene on tungsten carbide and platinum surfaces.* Physical Chemistry Chemical Physics, 2019. **21**(31): p. 17332-17342.

187. X. Tian, T. Wang, and H. Jiao, *Oxidation of the hexagonal Mo_2C(101) surface by H_2O dissociative adsorption.* Catalysis Science & Technology, 2017. **7**(13): p. 2789-2797.

188. J.D. Gouveia, Á. Morales-García, F. Viñes, F. Illas, and J.R.B. Gomes, *MXenes as promising catalysts for water dissociation.* Applied Catalysis B: Environmental, 2020. **260**.

189. A.J. Jones and E. Iglesia, *The Strength of Brønsted Acid Sites in Microporous Aluminosilicates.* ACS Catalysis, 2015. **5**(10): p. 5741-5755.

190. H. Prats, J.J. Piñero, F. Viñes, S.T. Bromley, R. Sayós, and F. Illas, *Assessing the usefulness of transition metal carbides for hydrogenation reactions.* Chemical Communications, 2019. **55**(85): p. 12797-12800.

191. M. Xu, S. Yao, D. Rao, Y. Niu, N. Liu, M. Peng, . . . M. Wei, *Insights into Interfacial Synergistic Catalysis over Ni@TiO_{2-x} Catalyst toward Water-Gas Shift Reaction.* Journal of the American Chemical Society, 2018. **140**(36): p. 11241–11251.

192. E.V. Clougherty, K.H. Lothrop, and J.A. Kafalas, *A New Phase formed by High-Pressure Treatment : Face-centred Cubic Molybdenum Monocarbide.* Nature, 1961. **191**(4794): p. 1194-1194.

193. Z. Li, Y. Xiao, P.R. Chowdhury, Z. Wu, T. Ma, J.Z. Chen, . . . A. Varma, *Direct methane activation by atomically thin platinum nanolayers on two-dimensional metal carbides.* Nature Catalysis, 2021. **4**(10): p. 882-891.

194. R. Morales-Salvador, J.D. Gouveia, Á. Morales-García, F. Viñes, J.R.B. Gomes, and F. Illas, *Carbon Capture and Usage by MXenes.* ACS Catalysis, 2021. **11**(17): p. 11248-11255.

195. B.B. Sarma, P.N. Plessow, G. Agostini, P. Concepcion, N. Pfander, L. Kang, . . . G. Prieto, *Metal-Specific Reactivity in Single-Atom Catalysts: CO Oxidation on 4d and 5d Transition Metals Atomically Dispersed on MgO.* J Am Chem Soc, 2020. **142**(35): p. 14890-14902.

196. I. Langmuir, *Part II.—"Heterogeneous reactions". Chemical reactions on surfaces.* Transactions of the Faraday Society, 1922. **17**(0): p. 607-620.

197. L. Beránek, *An Examination of the Langmuir-Hinshelwood Model Using Ion Exchange Catalysts.* Catalysis Reviews, 1977. **16**(1): p. 1-35.